Summer 8-10-2016

Engineering Nanoarchitectures from Nanosheets, Nanoscrolls, and Nanoparticles

Taha Rostamzadeh
University of New Orleans, New Orleans, trostamz@uno.edu

Engineering Nanoarchitectures from Nanosheets, Nanoscrolls, and Nanoparticles

A Dissertation

Submitted to the Graduate Faculty of the
University of New Orleans
in partial fulfillment of the
requirements for the degree of

Doctor of Philosophy
in
Chemistry
Nano-Materials

by

Taha Rostamzadeh

B.S. Semnan University, 2005
M.S. Tarbiat Modares University, 2008
M.S. University of New Orleans, 2013

August 2016

Dedication

To My Family

Acknowledgments

Keywords: *Nanomaterials, Nanopeapods, Nanosheets, Nanoscrolls, Nanoparticles, Synthesis, Characterization, Hexaniobate, Vanadium Oxide, Molybdenum Oxide, Surface Plasmon Resonance.*

Table of Contents

Table of Figures

viii

Abstract

The ability to encapsulate/insert different kinds of nanoparticles (NPs) in scrolled nanosheets (NSs) may lead to the formation of new nanocomposite materials that yield novel properties. These nanostructures resemble "peapods" that consist of NPs chains ("peas") located in a hollow space of desired nanoscrolls ("pods"). Depending on different combinations of "peas" and "pods" diverse families of nanopeapods (NPPs) can be synthesized which may exhibit interesting properties not accessible from the individual components. Though there exist various synthetic methods for the formation of NPPs, more development in terms of simplicity, flexibility, and productivity of synthetic approaches are needed so that different classes of NPPs with unique combinations/characteristics of "peas" and "pods" can be synthesized.

A simple solvothermal synthesis method for the encapsulation of spherical Fe_3O_4 NPs by the capture of preformed NPs in scrolled hexaniobate has previously been developed in our group. In the first part of this research, efforts were made to extend the "pod" materials to other inorganic NScs. Vanadate nanoscrolls (NScs) could rapidly (2h) be produced using a simple solvothermal treatment in the presence of V_2O_5 as vanadium source, and either dodecylamine (DDA) or octadecylamine (ODA) as the structure-directing agent. The synthesis parameters were successfully adjusted to obtain high yields vanadate NScs (~ 20 g of NScs per synthesis) with different average lengths as 383 nm, 816 nm to 3.3 µm. The effects of reaction time on the formation of NScs were also investigated.

Further efforts focused on the development of methods for making vanadate NPPs. Here, two novel approaches for the formation of these NPPs have been successfully developed. In the first, solvothermal methods utilizing preformed Ag NPs and vanadate NSs lead to the formation of Ag@vanadate NPPs where NPs could be encapsulated during the scrolling of NSs. High NP loadings were acquired with this approach. In the second method, an insertion strategy was developed where Ag NPs were drawn into the lumen of preformed vanadate NScs upon controlled solvent evaporation. This method was also quite effective, though much lower loadings of NPs were achieved with larger average NP-NP distances. Also noteworthy in the study of vanadate NScs and NPPs is the observation of an uncommon asymmetric scrolling

behavior; this was realized for both vanadate NScs and solvothermally synthesized Ag@vanadate NPPs.

Novel solvothermal approaches for the effective construction of organic-MoO_x hybrid structures and MoO_x nanosheets (NSs) have also been developed. These NSs can be controlled so as to exist in different oxidation states as well as in different crystal structures. Layer spacing as a function of organic molecule lengths could also be controlled by changing the type of surfactants located between the NSs. Individual NSs or a few layers of stacked NSs, up to four micrometers in lateral size were successfully prepared upon sonication. The effect of time, temperature, as well as the type of structure-directing agents on the formation and crystal structure of MoO_x intercalated compound/NSs were also explored.

Lastly, a modified solvothermal method previously used for the encapsulation of spherical Fe_3O_4 NPs inside hexaniobate NScs was applied for the construction of cubic-CeO_2 NPPs. High yield encapsulations of preformed cubic ~5 nm ceria NPs within the lumen of hexaniobate NScs were readily accomplished. Size selective encapsulation and the formation mechanism of cubic-CeO_2 NPPs were also studied. Pre-organization and attachment of ceria NPs to the surface/edges of hexaniobate crystals prior to the scrolling process were observed, which is in a good agreement with our previous studies on the formation mechanism of NPPs. Partially filled CeO_2@hexaniobate NPPs were further used in the in-situ growth of gold NPs within the empty/hollow space of hexaniobate NScs. This led to the formation of high-quality Au-CeO_2@hexaniobate NPPs. We believe that smart combinations of the methods for the formation of NPPs, encapsulation, in-situ growth and insertion, will allow one to acquire other classes of nanocomposite materials composed of different types, shapes, and arrangements of NPs in the hollow spaces of distinct NTs/NScs.

Chapter 1 Introduction

1.1 Nanotechnology

Nanotechnology as an interdisciplinary field is the science and technology of manipulation, characterization, observation, and application of matter at the nanoscale level.[1, 2] Though the concept of nanotechnology/nanoscience is fairly new, there are several historical examples revealing that nanomaterials have been used for centuries. One of the famous examples of the use of nanotechnology have been found in Lycurgus Cup[3, 4] which is a Roman glass cage cup held in British museum and dates back to the 4th century. This special cup, changes its color from opaque green in reflection to translucent red in transmitted light. Detailed analyses of this glass revealed the presence of gold, silver and copper nanoparticles embedded within the glass. The interaction of light with these tiny metal nanoparticles is responsible for this color change. Legendary Damascus[5, 6] swords are also pondered as another early example of nanotechnology; their excellent mechanical properties including flexibility and sharpness may have carbon nanotubes embedded within their steel matrix.

The highly regarded physicist Richard Feynman (1918-1988) in his famous 1959 speech, "There is Plenty of Room at the Bottom," is widely credited for the inspiration of modern nanotechnology.[7, 8] He speculated about a tiny world where advanced and precise tools could be used to rearrange and manipulate small molecules and atoms. The invention of scanning tunneling microscope (STM) in 1981 by Gerd Binning and Heinrich Roher,[9] an instrument which can be used for surface imaging at the atomic level, was a great advance in the characterization of nanomaterials and consequently lead to rapid progress in the development of nanotechnology/nanoscience. The discovery of fullerenes[10, 11] by Harry Kroto, Richard Smalley, and Robert Curl in 1985 and carbon nanotubes by Sumio Iijima in 1991[12] in 1991 opened up a huge interest in both scientific and engineering applications of nanotechnology. (It is worth noting that the history of carbon nanotube discovery is still controversial.[13]) Further improvement in characterization tools as well as progress in different synthetic approaches of nanomaterials over the last two decades, have been resulted in an exponential growth of research dedicated to the science and technology of materials in the nanoscale. Several novel methods for nanomaterials synthesis including those for different nanoparticles (NPs),[14, 15] nanowires

(NWs),[16, 17] nanorods (NRs),[18] nanotubes (NTs),[19] and nanosheets (NSs)[20] are now available. Unusual and advanced properties of nanomaterials in comparison to their bulk have also opened up new opportunities for further exploration of physical and mechanical properties of nanomaterials, resulting in a better understanding of size-dependent mechanical, optical, electrical, and, magnetic properties of different nanomaterials. Innovative approaches of to the engineering of patterned/self-assembled nanostructures as well as new nano-device concepts are being constantly discovered.[21]

1.2 Classification of Nanomaterials

Nanomaterials refer to materials whose length scale is, at least in one dimension, in the nanometer range. This range, which is usually considered between 1 to 100 nm, can vary depending on the emergence of new properties/effects at distinct nanoscale range for different materials/properties.[22-24] One nanometer (1 nm) is approximately equal to the length of 10 hydrogen atoms. One way to differentiate nanomaterials is based on their dimensionality. In general, nanostructured materials can be classified based on their dimensions as 0D (e.g. quantum dots), 1D (e.g. nanoscrolls (NScs)), 2D (e.g. nanosheets (NSs)), and 3D (e.g. nanocomposites composed of embedded 0D/1D/2D materials in metal/polymer/ceramic matrix), all of which can be presented in different sizes, forms and shapes.[22, 23] Size and morphological control of different nanomaterials including 0D, 1D, and 2D are interesting topics among different researchers. Nanoscale materials exhibit special properties compared to their bulk materials. One of the main reasons why nanoscale materials have special properties is due to their increased surface area to volume ratios as well as the presence of quantum effect in comparison to bulk materials.[22, 23, 25]

Bulk polycrystalline materials consisting of ultrafine grains/crystallites were also classified and considered as bulk nanostructured/nanocrystalline materials by Herbert Gleiter.[26, 27] Bulk nanostructured materials in which considerable numbers of atoms are located at grain boundaries, have been fabricated using several irreversible non-equilibrium processes such as rapid quenching from the molten phase,[28] severe plastic deformation (SPD)[29] including equal channel angular pressing (ECAP),[29] and high pressure torsion (HPT).[30] Several properties of bulk nanocrystalline samples such as mechanical strength, toughness, ductility, hardness, and thermal

expansion are different from their microcrystalline counterparts.[26] It should be noted that there are, however, some nanomaterials that simply cannot be classified by either their dimensionality or micro/nanostructures, which are categorized mainly by their shapes and are gathered in the handbook of less-common nanostructures.[31] Solvothermally synthesized ZnO nanoflowers are an example of one such unusual structure (Figure 1.1).
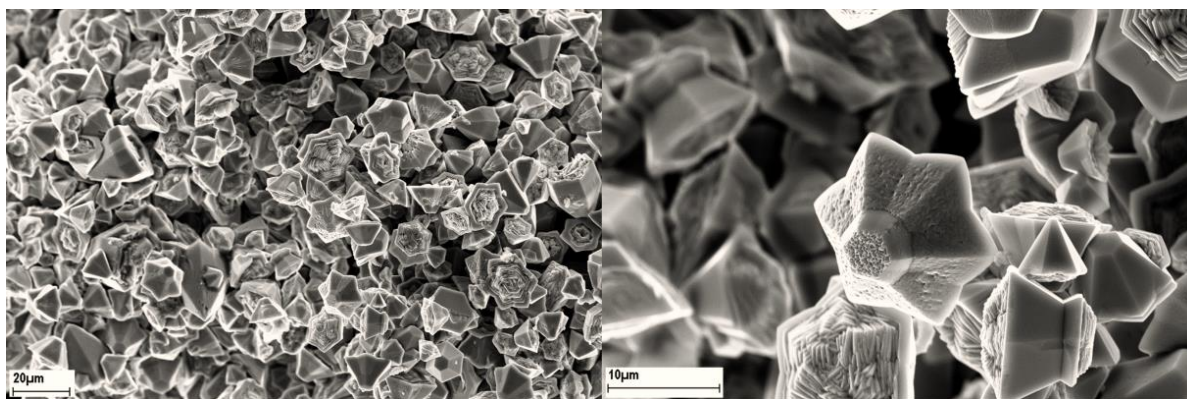
Figure 1.1. SEM images of ZnO nanoflowers.

Nanomaterials can also be classified by their synthesis/fabrication methods to two main categories known as "top-down"[32] and "bottom-up"[33] approaches. Top-down processes can be considered as being subtractive approaches in which nanostructured materials can be obtained by starting from a large piece/unit of matter and reaching to a nano size/grain size material mainly through diverse physical or mechanical and sometimes chemical means. Mechanical milling,[34] electron beam lithography,[35] etching,[36] and laser ablation[37] are some examples of this method.

In the case of "bottom-up" approach, however, small units such as atoms or molecules are considered as building blocks and through different synthesis/assembly approaches, a variety of nanomaterials from 0D to 3D, with controlled shape and size, can be synthesized.[38]

1.3 Nanoparticle Synthesis

There exist a variety of methods for the synthesis of different NPs which can be categorized as either top-down and bottom-up.[3] Bottom-up approaches, however, are more popular and different NPs can be chemically produced through a homogeneous/heterogeneous nucleation from liquid/vapor phase, followed by a growth process. Hydrothermal/solvothermal, reduction,

combustion, precipitation, co-precipitation, sol-gel, sonochemical, and microwave-assisted synthesis methods are all widely used approaches for the formation of different types of NPs including noble metals, metal oxides, quantum dots, etc.[39, 40]

Different steps are involved in the formation/precipitation of NPs from a liquid phase. These include the generation of atoms, nucleation, and growth as shown in Figure 1.2.[41, 42] Depending on the synthesis approach, atoms can be generated from reduction/precipitation of precursor dissolved in the particular solvent. In the first step, atomic concentration increases upon an increase in the reaction time. Nucleation, which is the formation of a very small solid phase, can start when the atomic concentration of the solute reaches the critical point needed for nucleation. After/during nucleation and growth, the atomic concentration drops as shown in Figure 1. The degree of supersaturation (S) can be defined as $S=C/C_0$ where C and C_0 are the solute concentrations at saturation and equilibrium, respectively.[43] In the literature, the difference in C and C_0, $\Delta C=C-C_0$, is commonly considered as the driving force for precipitation/nucleation.[43]
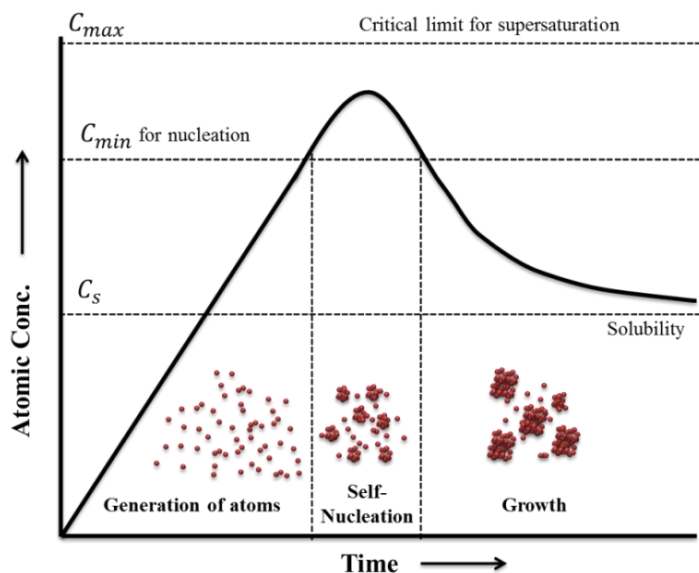
Figure 1.2. Schematic showing different steps involved in the formation of NPs including generation of atoms, self-nucleation and subsequent growth.[42]

The Gibbs free energy of a supersaturated system would be reduced by precipitation of a solute from the solution. The Gibbs free energy of a system is defined as [44]

4

$$G = H - TS; \quad H = E + PV \tag{1.1}$$

where H is the enthalpy, T is the absolute temperature, and S is the entropy or the degree of the randomness of the system. Enthalpy, itself, is the amount of heat content of the system for which E is the internal energy of a system (overall kinetic and potential energies), P is the pressure and V is the volume.[44] In the case of solid and liquid, the PV term is usually very small in comparison to E and can be ignored. A system is in equilibrium when it is in the most stable state. A closed system (e.g. fixed mass and composition) at constant P, and T will be in stable equilibrium if it has the lowest possible value of Gibbs free energy ($dG=0$). [44]

From the definition of G (eq. 1.1), it can be realized that the highest stability of a system can be reached when the best compromise between low enthalpy (E) and high entropy (S) is provided. For example, at low temperatures, solid phases have the strongest atomic binding and so the lowest internal energy (E). Therefore, solids are the most stable phase at low temperatures. However, at elevated temperatures, -TS term will dominate and liquid and gas phases with more entropy become more stable. This is further illustrated in Figure 1.3. As can be seen, $dG=0$ for two different imaginary configuration of atoms, A, and B.
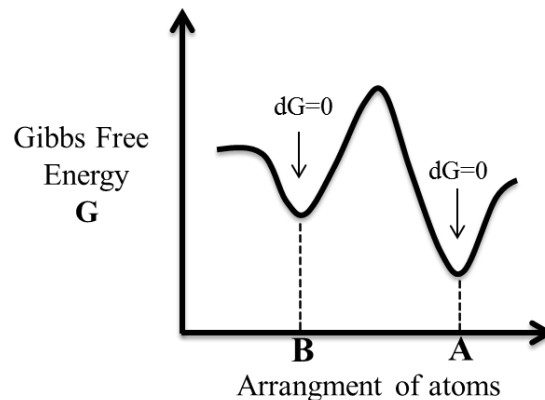
Figure 1.3. Variation of Gibbs free energy (G) with respect to different arrangement of atoms. B: metastable state, A: the most stable equilibrium.[44]

However, configuration A has the most stable state since it has the lowest value for Gibbs free energy. Configuration B also has a minimum ($dG=0$), but it does not have the lowest

possible value for G. this configuration is called a metastable equilibrium state. Any transformation that results in a reduction of Gibbs free energy ($\Delta G = G_2 - G_1 < 0$) such as the transformation from metastable state (configuration B) to the most stable state (configuration A) is favorable. However, sometimes such transformation may take a very long time due to the presence of the free energy hump between metastable and the most stable states (Figure 1.3). The rate of transformation could further be studied through kinetic of transformation.[44]

1.4 Basics of Homogeneous Nucleation

As explained above, the reduction of Gibbs free energy can be considered as the driving force for both the nucleation and growth processes.
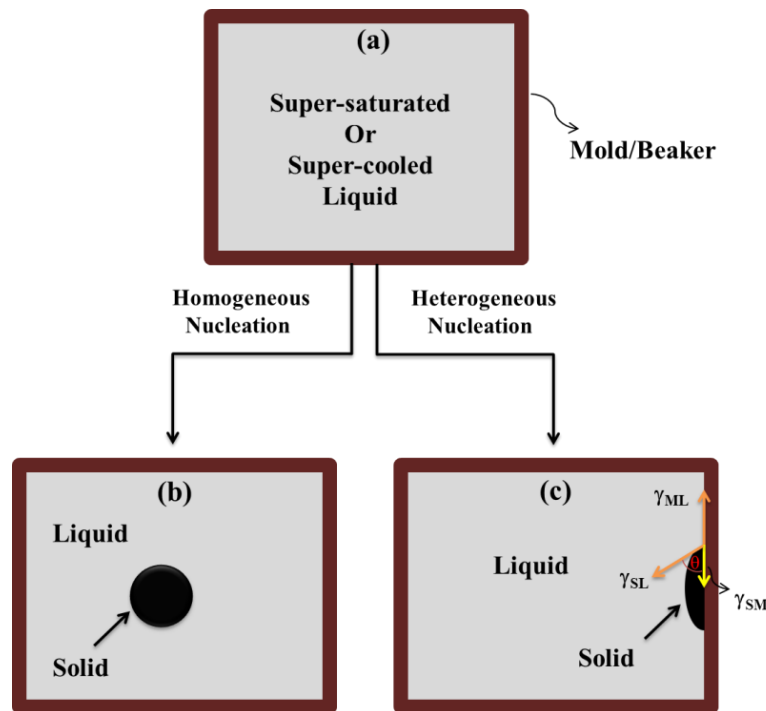
Figure 1.4. Schematic showing the homogeneous and heterogeneous nucleation of a solid from a supersaturated/supercooled liquid.

Assume a given volume of supersaturated liquid with a free energy G_1 (Figure 1.4a), the Gibbs free energy of the system can be reached to G_2 through the homogeneous formation of a solid within the liquid (Figure 1.4b). G_2 can be defined as:

$$G_2 = V_S G_v^S + V_L G_v^L + A_{SL} \gamma_{SL} \qquad (1.2)$$

Where V_S and V_L are the volume of the spherical solid and liquid, respectively, G_v^S and G_v^L are the free energy per volume unit for the solid and liquid, respectively, A_{SL} is the solid/liquid interfacial area, and γ_{SL} is the solid/liquid interfacial free energy per unit area. G_1, the free energy of the system before the formation of solid, can also be defined as[44]:

$$G_1 = (V_S + V_L) G_v^L \qquad (1.3)$$

The total change of G for the formation of a nucleus is therefore defined as:

$$\Delta G = G_2 - G_1 = -V_S \Delta G_v + A_{SL} \gamma_{SL} \qquad (1.4)$$

Where

$$\Delta G_v = G_v^L - G_v^S \qquad (1.5)$$

Finally, the ΔG associated with homogeneous nucleation of a sphere with radius r, can be given by:[42, 44]

$$\Delta G_r = -4/3 \pi r^3 \Delta G_v + 4 \pi r^2 \gamma_{SL} \qquad (1.6)$$

This variation, as well as the total free energy for the formation of a nucleus, is shown in Figure 1.5. Due to supersaturation, ΔG_v is a positive term, so the formation of small volume of the sphere has a negative contribution ($\propto r^3$) in ΔG of nucleation. On the other hand, there is a

positive contribution ($\propto r^2$) due to the creation of a new surface and S/L interface. Therefore, there is a maximum for the total free energy (ΔG_r) labeled as ΔG^*, acting as the energy barrier for the nucleation process.[42, 44]
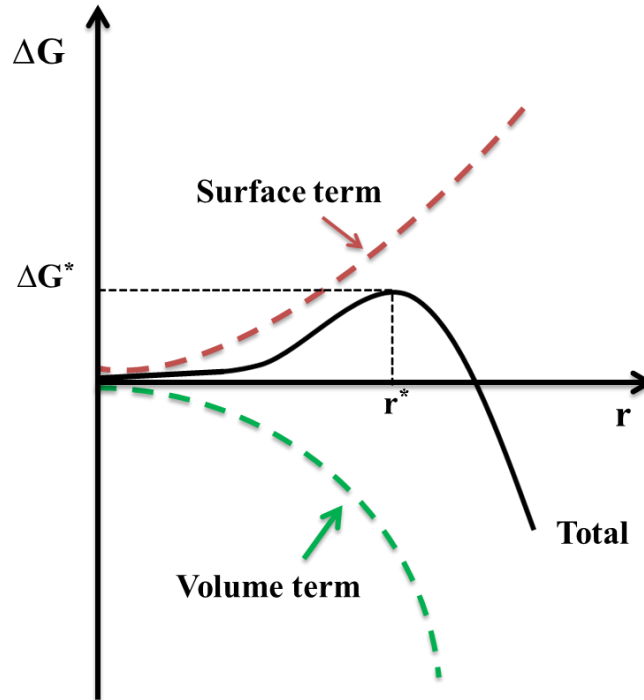
Figure 1.5. Schematic showing the change of surface free energy ($\propto r^2$) volume free energy ($\propto r^3$), and total free energy, ΔG, as a functions of r.[42, 44]

It can be seen from Figure 1.5 that there is a critical radius, r*, for a formed solid associated with the critical energy ΔG^*. When r = r* the formed solid can be called nucleus which is in unstable equilibrium with surrounding liquid. If r > r*, the formed solid is called nucleus. Total free energy of the system can be reduced by growing the nucleus. However, when r < r* the formed solid, referred to as a cluster or an embryo, is not stable. Clusters/embryos may disappear to decrease the total free energy of the system (Figure 1.5). r* can be obtained by differentiation of Equation 1.6 as: [42, 44]

$$r^* = 2\gamma_{SL}/\Delta G_V \qquad\qquad\qquad (1.7)$$

ΔG*can, therefore, be defined as:

$$\Delta G^* = 16\pi\gamma^3_{SL}/3(\Delta G_V)^2 \qquad (1.8)$$

In the case of heterogeneous nucleation, a new phase forms on the surface of other materials such as solid impurities and/or mold/beaker walls (Figure 1.4c). It can be proven that $\Delta G^*_{het} < \Delta G^*_{hom}$ and also $r^*_{het} < r^*_{hom}$ as schematically shown in Figure 1.6. [44]
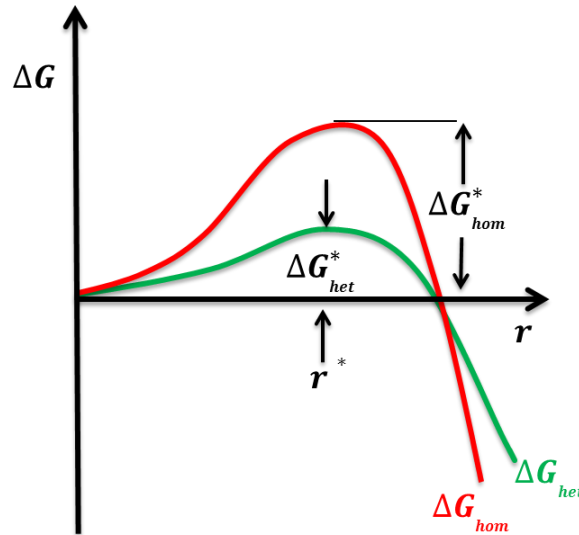
Figure 1.6. Schematic showing the change in total free energy, ΔG, for homogeneous and heterogeneous nucleation.[44]

This implies that at low supersaturation, where there is not enough driving force for homogeneous nucleation provided, heterogeneous nucleation can be dominated. Using smaller reaction container (e.g. vial/mold) as well as high supersaturation, homogeneous nucleation can, however, be encouraged, which may result in the formation of mono-dispersed and uniform NPs.

The results of above discussion, which was based on the nucleation of a solid phase in a supersaturated solution/supercooled liquid, can be generalized and applied to nanomaterials size control in variety of synthesis approaches including those related to the formation of NPs from

vapor/gas/liquid. For example, r* represent a limit on how small NPs can be; this size can be altered by tuning the synthesis parameters. In order to reduce r* and ΔG^*, one may need to reduce the surface energy of the new phase (γ_{SL}) by using different surfactants/additives and by increasing the level of supersaturation. [41-44]

To obtain uniform size distribution of NPs, it is desirable to have a nucleation process that occurs on a short time scale.[45] This way, all of the quickly formed nuclei can have similar size. Separation of nucleation and growth processes as well as elimination of secondary nucleation can also be considered for obtaining monodispersed NPs.[46, 47] In practice, several techniques including a rapid injection of precursors at elevated temperature[47, 48] are designed to have an abrupt nucleation process. The same growth conditions for the similar size nuclei can guarantee the formation of mono-sized NPs. After a rapid nucleation, the process can terminated if the atomic concentration decreases below a minimum concentration needed for nucleation (Figure 1.2). However, the growth step will continue until the atomic concentration reaches the equilibrium concentration of solubility, C_s (Figure 1.2).[42]

There are different steps involved in the subsequent growth of formed nuclei. First, generated growth species should diffuse from bulk (liquid) to the growth surface. Then, growth species should be adsorbed onto the growth surface. Finally, the surface of the formed nuclei/solid can grow through irreversible incorporation of growth species onto their surface.[42] If the diffusion of growth species on the surface is very slow, when the atomic concentration of surface is similar as that for the bulk, growth rate can be controlled by diffusion. However, growth rate can be controlled by surface processes when/if diffusion of growth species is sufficiently rapid.[42] It has been suggested by *Williams et al.*[49] that both diffusion and surface controlled mechanisms are involved during the growth step. For the smaller nuclei, the growth process is mainly controlled by a surface-controlled mechanism, while for bigger NPs, diffusion rates can control the growth rate.[42]

In order to synthesize mono-sized NPs through a homogenous nucleation, a diffusion-controlled mechanism for the growth step is required.[42] For example, using a very low concentration of growth species, diffusion distances would increase and, thus, diffusion could become the limiting step. For those synthetic approaches where growth species are provided by the reduction of a precursor, the use of a very weak reducing agent allows a gentle generation of atoms/growth species.[41-43, 47] Introduction an additive/surfactant to the surface of growing nuclei

10

as well as a viscous solvent to the synthesis media can also be considered as another approach for controlling the diffusion and growth rate of the NPs.[42, 48]

The reduction of Gibbs free energy (thermodynamic consideration) is also considered as the driving force for nanocrystal growth.[42] Ostwald ripening,[50] where bigger nuclei/NPs grow at the expense of smaller nuclei/NPs, is one of the main suggested mechanisms for the NPs growth. The reduction of surface energy can be achieved by elimination of very small NPs having a large surface area. Digestive ripening,[51] however, is the inverse process of Ostwald ripening where smaller particles grow at the expense of the larger ones. A digestive agent is however needed for such ripening to occur.[51] Coalescence and orientated attachment are other suggested mechanisms for the crystal growth.[52] Though they are very similar, they differ in the orientation of NP attachment. In the case of orientated attachment, NP attachments can happen through a common crystallographic facet to minimize the interfacial energy. For the coalescence, though, there is no specific preference observed for the attachment and crystal facets are randomly positioned between domains.[52]

1.5 Synthesis of Noble Metal Nanoparticles

Noble metal NPs can generally be synthesized via a reduction of metal complexes in dilute solutions.[53] In the synthesis of metallic NPs, several types of precursors, reducing agents, surfactants, solvents, and methods were used/ developed to control the formation of NPs through the initial nucleation and the subsequent growth processes.[41, 42] Diverse reducing agents with different reduction abilities can be used to control the generation rate of metal atoms and, therefore, the nucleation rate. Sodium citrate, sodium borohydride, sodium carbonate, sodium hydroxide, oleylamine, hydroxylamine, hydrogen peroxide, hydrochloride, citric acid, carbon monoxide, and hydrogen have all been reported to act as reducing agents for the reduction of metal ions to atoms in the synthesis of metallic NPs.[42, 54, 55] Generally, a strong reducing agent can increase the nucleation rate and lead to the formation of smaller NPs. In the presence of a weak reducing agent, obtained NPs can be larger and have a narrow size distribution if secondary nucleation is prevented. Low concentration of solute as well as the existence of surfactant in different synthesis media can hinder rapid diffusion of growth species from the surrounding solution/media to the growth surface resulting in the formation of uniform NPs.[42, 48] Depending

on the surface chemistry, interaction of surfactant/polymer stabilizer with the formed solid/nuclei is one of the main synthetic parameters that can influence both NPs size and shape. A strong adsorption of surfactant to the surface of growth sites could reduce the growth rate of NPs. Beside, different surfactants may have different tendencies towards different facets of crystals, so that they can encourage/hinder the growth rate of different crystal facets. [48, 56] Varying the type and amount of surfactants/capping agents, therefore, is one of the main synthesis parameters that can influence NPs shape.[48, 56] The surface functionality of NPs, which can be tuned using different capping agent/surfactant plays an important role in the properties of NPs including dispersibility, catalytic activity, stability, reactivity, and melting point.[57, 58] Synthesized NPs can be dispersible in either a polar or a nonpolar solvent depending on the capping groups attached on their surface. Surface of NPs can be, further, modified using different ligand exchange approaches.[57, 59]

1.6 Solvothermal Synthesis of Nanomaterials

There exist a variety of reports on the formation of different dimensional inorganic nanomaterials (0D, 1D, and 2D) using a solvothermal (ST) synthetic approach.[58, 60-62] ST is similar to hydrothermal (HT) approach except that, in the case of ST, different types of organic solvents instead of water can be used.[63] A typical set-up including Teflon liner and autoclave (Parr, model 4749, 1800 psig) used in the ST preparation of inorganic materials is shown in Figure 6. In the preparation procedure, the reaction mixture should be placed/transferred into a Teflon liner, and then sealed within stainless steel pressure vessel or autoclave.[58] Heating the sealed autoclave at the temperature higher than the boiling point of the solvent, may create a high pressure depending on several parameters including type of solvents, filling fraction of the Teflon liner, temperature and the existence of different precursors and/or surfactants in the synthesis media. Using high temperatures as well as different solvents with low boiling points, the pressure within the reaction vessel can be increased, which results in a rapid nucleation and growth processes and, therefore, facile crystallization/formation of nanomaterials.[58, 62, 63]
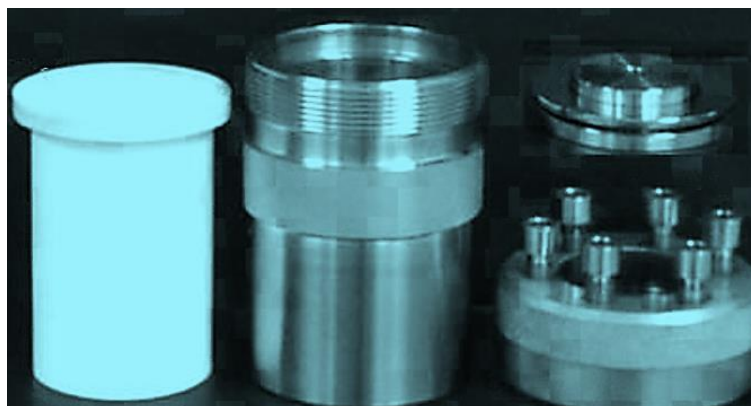
Figure 1.7. A typical set up used for solvothermal synthesis of nanomaterials; 20 mL of Teflon liner (left), stainless steel container (autoclave, middle) corrosion disc (upper right), and screw cap (lower right).
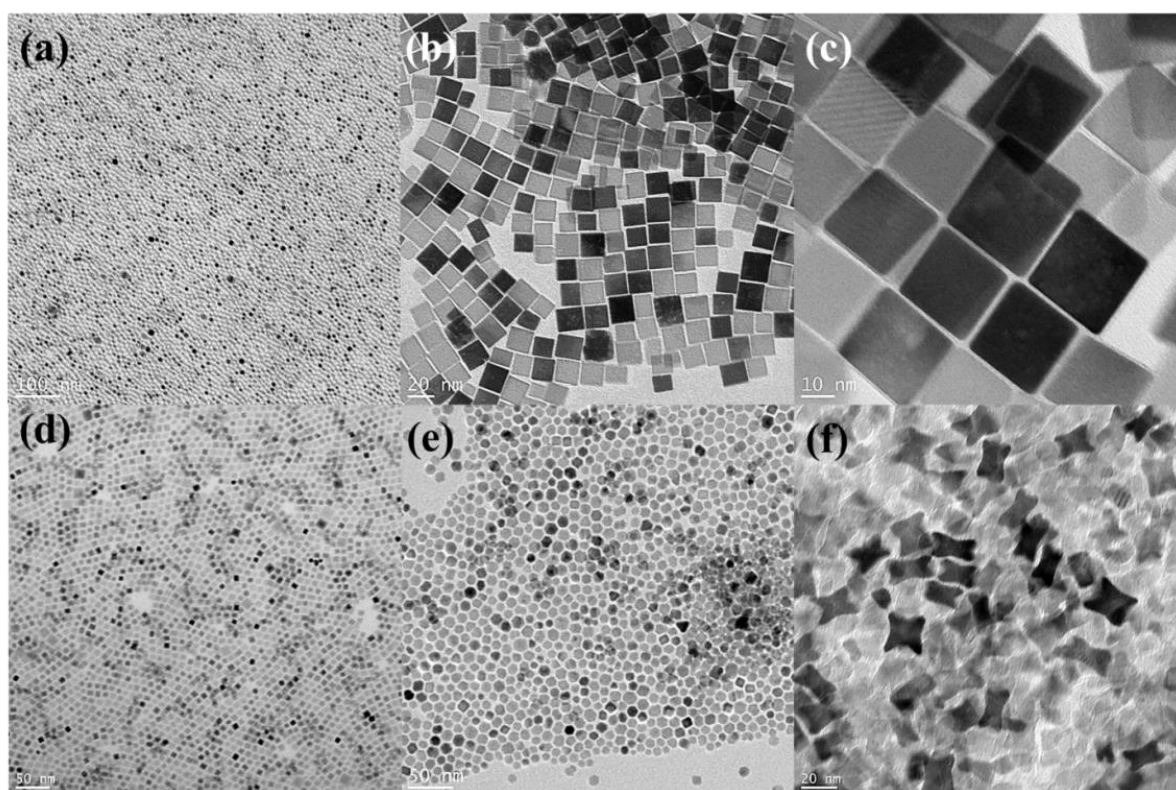
Figure 1.8. TEM images of solvothermally synthesized NPs (a, and b) about 5nm, and 25nm cubic ceria, (c) 25nm Fe_2O_3, (d) 9nm cubic Mn_3O_4, (e) 12nm Fe_3O_4 and (f) TiO_2 NPs (all these nanoparticles were synthesized in our laboratory).

Solvothermal synthetic approaches have been used for the shape and size control of different type of NPs such as metal oxide (e.g. $BaTiO_3$[60, 64], TiO_2[65], and Fe_2O_3[66]), noble metals (e.g. Ag),[61] and metal chalcogenide (e.g. CdS[67] and $CdSe$[68]). These methods have widely been applied by our group for making/developing a variety of nanomaterials including NPs of Fe_3O_4, Fe_2O_3, $BaTiO_3$, CeO_2, TiO_2, and Mn_3O_4, nanosheets (NSs) of MoO_x, and hexaniobate and vanadate NScs. Some examples of the various synthesized metal oxides NPs are shown in Figure 1.8.

1.7 Layered Inorganic Materials

Layered materials consist of two-dimensional (2D) sheets which are usually stacked weakly (e.g. van der Walla bonds) to form three-dimensional (3D) structures.[69] There are different types of layered materials including clays (layered silicates), graphite, hexagonal boron nitrate (h-BN), transition metal dichalcogenides (e.g. MoS_2), transition metal trichalcogenides (e.g. $TiTe_3$), metal halides (e.g. $MoCl_2$, and $CrCl_3$), metal oxides (e.g. V_2O_5, MnO_2, MoO_3, $K_4Nb_6O_{17}$), layered doubled hydroxides (LDHs), III-V layered semiconductors (e.g. GaSe, and InSe), and layered perovskites.[69-71]

Graphite has relatively a simple crystal structure composed of layers of hexagonally arranged carbon atoms connected to each other by strong covalent bonds. Individual layers of graphite, however, stack on top of each other by weak van der Waals forces (Figure 1.9a).[69] h-BN has a similar crystal structure and layer spacing to graphite, though covalent C-C bonds are replaced by B-N bonds (Figure 1.9b). [72, 73]

Transition metal dichalcogenides (TMDs) are another important class of layered materials can have a variety of crystal structures depending on different combinations of transition metals and chalcogens. MoS_2, a typical example of a TMD, is composed of a plane of metal atoms (Mo) sandwiched between planes of chalcogens (S), as can be seen in Figure 1.9c. Different types of TMDs have shown metallic, semimetallic and semiconducting behavior depending on their crystal structure as well as oxidation states and coordination of metal atoms.[69, 71]
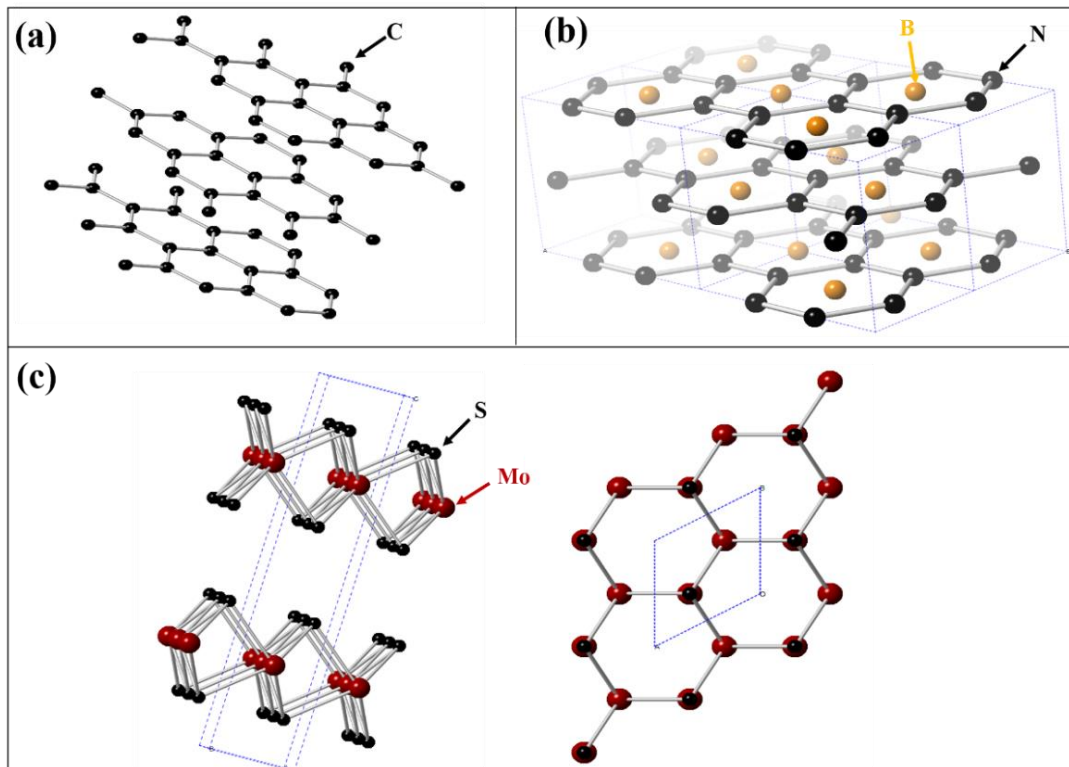
Figure 1.9. Crystal structure of common layered materials drawn using crystal maker software a) graphite b) BN, and C) MoS_2 in two different orientations.

Similar to TMDs, layered metal oxides have different crystal structures and have found applications in catalysts and batteries. Crystal structures of α-V_2O_5 and α-MoO_3 are shown in Figure 1.10. V_2O_5 has an orthorhombic crystal structure and composed of layers of distorted square pyramids of VO_5 that alternate (up and down) orientation. In each square pyramids, V atom is connected to five oxygen atoms. The pyramids share their corners to make a double chain which are connected along the edges to form individual layers.[74] There exist three nonequivalent types of oxygen atoms in each layer. O_b, bridging oxygen atoms, is coordinated with two V atoms. O_v, vanadyl oxygen, and O_c, chain oxygen atoms, are coordinated with one and three vanadium atoms, respectively. Orthorhombic crystal structure of α-MoO_3 is also displayed in Figure 1.10b. Each bilayer consists of edge sharing distorted MoO_6 octahedral which are cross-linked by bridging oxygen atoms.[75] There are similarly three nonequivalent oxygen atoms in the structure of α-MoO_3 as marked in the Figure 1.10b.
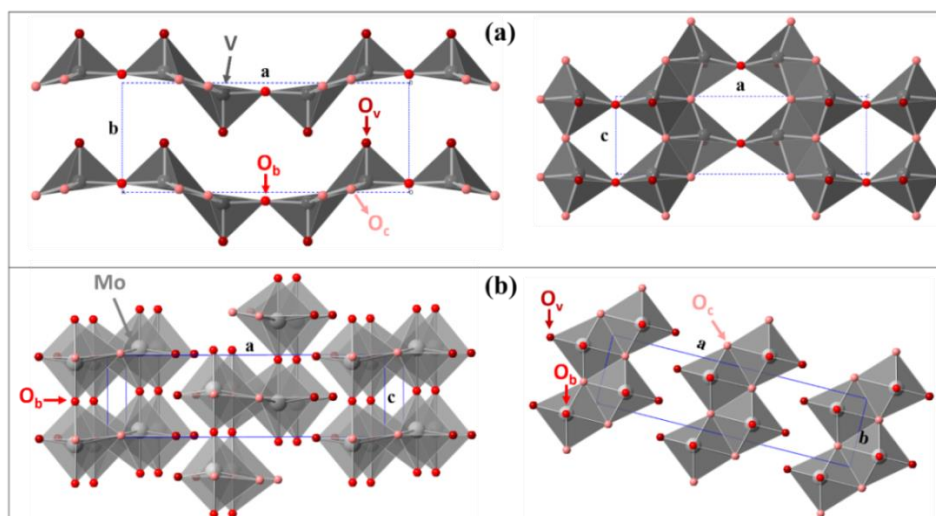
Figure 1.10. Crystal structure of two significant layered oxides a) V_2O_5, and b) MoO_3 shown at two different perpendicular directions.
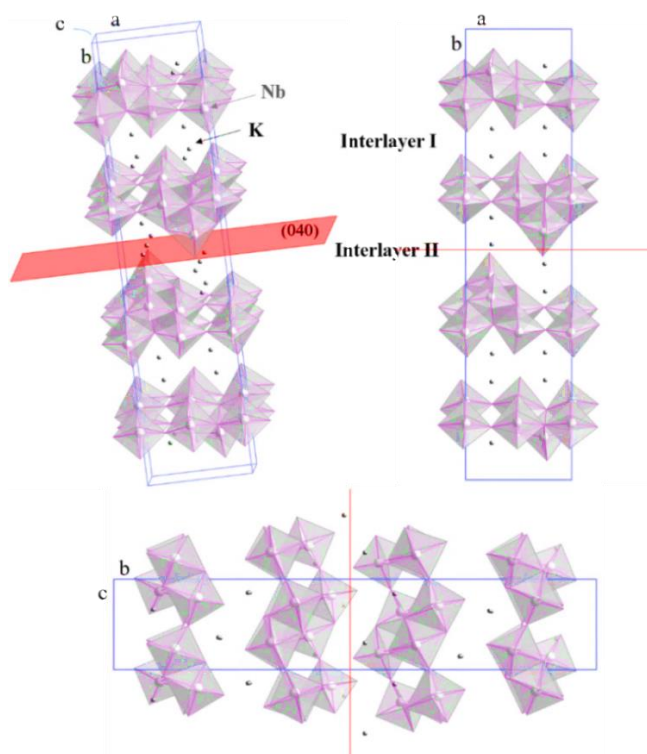
Figure 1.11. Crystal structure of $K_4Nb_6O_{17}$ shown at three different directions.

The orthorhombic crystal structure of $K_4Nb_6O_{17}$[76], an important photocatalyst, is shown in Figure 1.10. Each unit cell contains four negatively charged layers along the *b* axis, which are

composed of corner and edge-sharing distorted NbO_6 octahedra. K ions are located between the layers in order to compensate the negative charges of layers. There exist two distinct interlayers; interlayer I and interlayer II. The distance between interlayer I and II is dissimilar and they show different ion exchange behavior. While interlayer I can be ion exchanged by variety of cations, ion-exchange within interlayer II is quite unusual.[76-78]

1.8 Exfoliation of Layered Materials

Layered materials with strong chemical bonds in-plane and weak out of plane bonds can be exfoliated, leading to the formation of nanosheets (NSs) or 2D materials.[69, 71] When inorganic NSs are isolated, their properties can be considerably different from their 3D counterparts (e.g. graphene, and h-BN). Owing to the presence of a large accessible/effective surface area and the fact that each atoms can be a surface atom (in a monolayer), 2D materials are an excellent choice for those applications that desire large surface area and active surface; such as in catalyst and batteries.[69-71] Electronic band structures of NSs have also been reported to be different from their 3D counterparts due to the confinement of electrons in 2D. For instance, bandgap of bulk MoS_2 changes from 1.3 eV to 1.9 eV after exfoliation.[69] After the discovery of graphene and its extraordinary properties, a number of techniques, including mechanical exfoliation and liquid exfoliation, have been developed for exfoliation of other layered materials. Mechanical exfoliation were developed to make monolayers of graphene and then have been applied to make other 2D materials such as h-BN, and MoS_2.[69] This technique usually results in low-yield production of high quality 2D NSs.[69] Liquid exfoliation, which can be categorized into ion intercalation, ion exchange, and ultrasonication, in contrast, can be applied for large-scale production of NSs from variety of layered materials including layered oxides.[69-71] For instance, NSs of h-BN, MoS_2, WS_2, MnO_2, MoO_3, V_2O_5, and etc. have successfully been exfoliated using liquid exfoliation method.[69-72]

The large interlayer spacings of layered materials can be further increased upon intercalation of guest molecules/ions between the layers. This swelling results in further weakening of interlayer attractions. Individual layers can then be separated via ultrasonication.[69-72] There exist ions between the layers of some layered materials (e.g. K^+ in $K_4Nb_6O_{17}$ interlayers), which can be exchanged with other ions, usually larger ones. This may also be resulted in the reduction of

layers interactions and, therefore, facilitated the exfoliation process.[69-72] For example, protonated $K_4N_bO_{17}$ can be exfoliated using TBAOH as exfoliation agent and then rolled-up into a tubular structure.[73, 79, 80]

After the exfoliation, due to large surface area of free standing 2D materials and, therefore, their high surface energies, separated NSs may have a tendency to restack/aggregate or scroll.[69, 71, 79] This problem can be overcome by variety of techniques such as electrostatic stabilization of NSs using appropriate surfactants as well as the use of the appropriate solvents with surface energies similar to the layered materials.[69, 81] It worth mentioning that utilizing different self-assembly approaches, it is possible to restack separated 2D NSs and develop new hybrid materials/crystals. Formation of highly-oriented MoO_x nanosheets will be described in Chapter 3.

1.9 Inorganic Nanotubes/Nanoscrolls

Single-wall nanotubes (SWNT), multi-wall nanotubes (MWNT) and nanoscroll (NSer) are important classes of nanomaterials due to their special morphologies and geometries. NScs consist of convolved NSs and can have distinct morphological features.[82, 83] Carbon nanotubes (CNT), the most well-known example of NTs, was first reported by Iijima in 1991.[82, 84] During the last few decades, NScs and NTs have drawn extensive attention due to the existence of their three accessible surfaces, inner volume (lumen), outer surface and the interlayers of the multi-walled systems, as well as their interesting properties.[78, 83]

Though there are a few examples, such as halloysite and chrysotile NTs, which can occur naturally,[4, 78] there have been developed a number of methods for the synthetic formation of NTs/NScs from both layered and non-layered materials. High temperature synthesis, laser ablation, chemical vapor deposition (CVD), solvothermal/ hydrothermal and template-assisted synthesis are a few examples of techniques already developed for the production of nitrides (e.g. BN), metal chalcogenides (e.g. WS_2, MoS_2, TiS_2, Bi_2Se_3, NbS_2, and $NbSe_2$), metal oxides (e.g. $K_4Nb_6O_{17}$, V_2O_5, MnO_2, TiO_2, GeO_2, ZnO, CoO, Co_3O_4, $BaTiO_3$, $PbTiO_3$, Fe_2O_3, and Al_2O_3), and carbon nanotubes (CNTs).[4, 73, 79, 82, 83, 85]

Our group has particularly been interested in solvothermal synthesis of different types of NScs/NTs especially metal oxides. ST-synthesis of $K_4Nb_6O_{17}$ NScs has already been reported by

Adireddy *et. al.*[86] Rapid ST-synthesis of vanadate NScs utilizing vanadium oxide as vanadium source and dodecylamine as structure directing agent will be discussed in details (Chapter 2).

1.10 Nanopeapods

NPPs are categorized as uncommon nanomaterials.[31] Resembling the "peapod", NPP is a descriptive term that refers to a nanocomposite structure in which interior space of NT/NSc is filled with a chain of NPs.[87] The typical example of NPPs is related to CNTs filled with C_{60}.[31, 88] Initial studies on synthesis of C_{60}@CNTs involved using preformed open-ended CNTs and filling them by physical or chemical approaches.[88-91] After the discovery of C_{60}@CNTs NPPs and its unusual properties, different research groups have reported the formation of other types of NPPs with different components. Synthesis methods, possible applications and properties of some metal-based NPPs are summarized in the Table 1.1. The ability to make noble metal NPs@NSc/NTs may lead to the formation of new nanoarchitectures that are capable of different applications such as surface-enhanced Raman scattering (SERS),[92] optical waveguides, photonics, and nanodevices for biological and chemical sensing.

Beside different types of NPs and NTs/NSs, shape and size of encapsulated/inserted NPs, structural uniformity, lengths and interlayer distances of NTs/NScs, NPs distance, filling fraction of encapsulated/inserted NPs, and NPs arrangement in the case of bi-functional NPPs, are other important factors that could be controlled in order to tune the structures, morphologies, and different properties of NPPs (Figure 1.12). Filling different types of NTs using variety of NPs is very attractive for the development of advanced nanocomposites with innovative properties, depending on the intrinsic behavior of encapsulated NPs as "peas" and NTs/NSs as "pods."

These materials are also important for studying interactions of NPs/NPs and NPs/NSc.[92, 100] Specifically, when arrays of NPPs are arranged either parallel or perpendicular to the surface of a desired substrate, they can provide a system to investigate fundamental questions, such as those about the interaction of light, electric field and magnetic field with respect to NPs/NScs compositions as well as NPs/NScs distances (Figure 1.13). Although several synthetic methods for the fabrication of NPPs have already been developed,[87, 97, 99, 100] NPPs fabrication routes need more development in terms of simplicity, flexibility, and productivity so that different types on NPPs with controlled compositions, morphologies and NPs distances can be synthesized.

Table 1.1. Summary of some noble metals based nanopeapods: synthesis methods, properties applications and references.

Peapod	Synthesis method	Properties-applications
Au@ITO[93]	Thermal evaporation	Enhanced photoluminescence Photonic and optoelectronic devices
Au@Ga$_2$O$_3$ nanowire[94]	Thermal annealing of core-shell Au-Ga$_2$O$_3$ nanowires	Plasmonic behavior
Au@Ga$_2$O$_3$[94]	Thermal deposition	Plasmonic behavior
Au@Ga$_2$O$_3$ nanowire[95]	Thermal annealing	Surface plasmon resonance, nanophotonic switch
Au@MgO[96]	Vapor–liquid–solid growth	Formation mechanism
Ag@SiO$_2$[97]	Aqueous solution-ammonia dissolution treatment	Chemical sensing, plasmonic
Au@CoAl$_2$O$_4$[98]	Electrodeposition followed by heat treatment	Plasmon absorption
Pt@CoAl$_2$O$_4$[99]	Pulsed electro-deposition	Formation mechanism, structural design

In 2013, Adireddy *et al.* developed a solvothermal method for the formation of Fe$_3$O$_4$@hexaniobate NPPs by the capture of preformed NPs in scrolled NSs.[58] Beside the encapsulation of two different types of NPs within hexaniobate NScs and formation of both Fe$_3$O$_4$-Au@hexaniobate[101] and CeO$_2$-Au@hexaniobate NPPs, we have recently developed two novel approaches for making vanadium oxide-based NPPs. Control of layer spacings of vanadate NScs as a newly developed "pods" and encapsulation/insertion of different types of NPs as "peas" have also been achieved. Synthesis of vanadate based NPPs will be the topic of Chapter 3. Formation of CeO$_2$-Au@hexaniobate using the in-situ growth of gold within partially filled NPPs will also be discussed in Chapter 5.
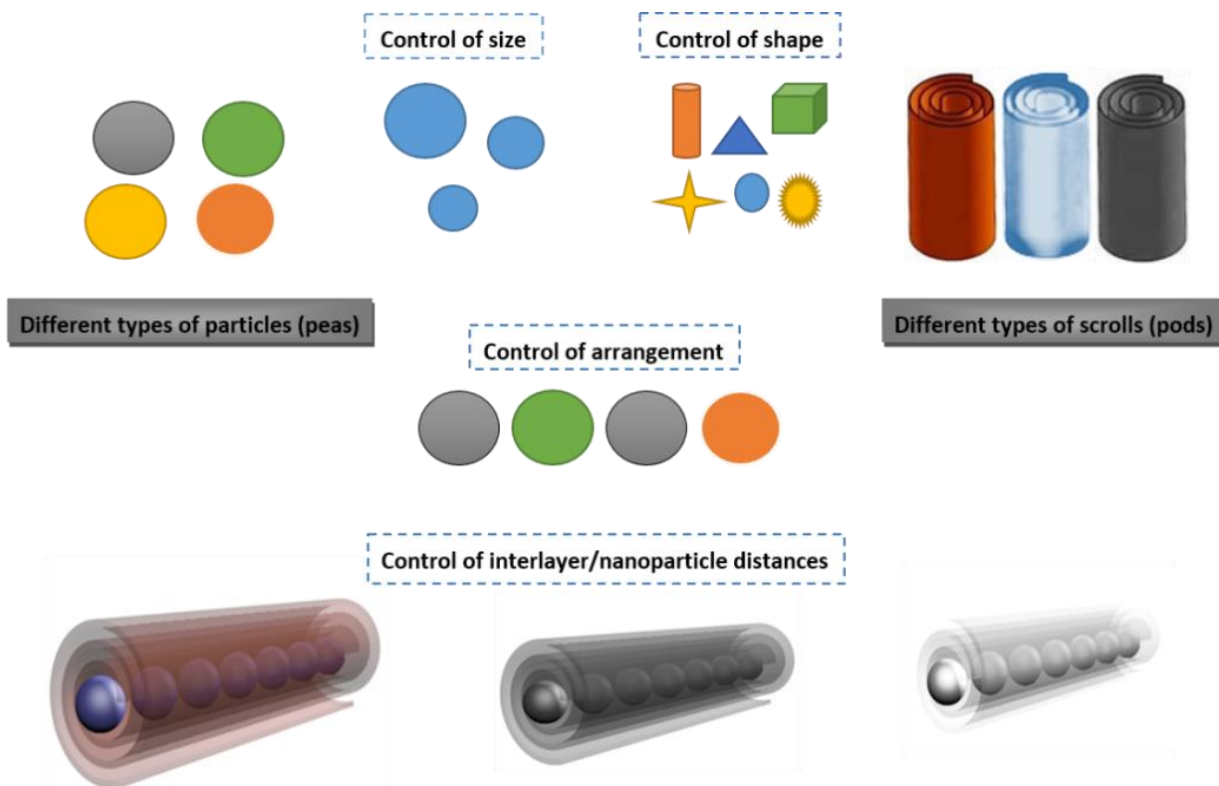
Figure 1.12. Schematic showing controllable parameters and variety of possible NPPs structures.
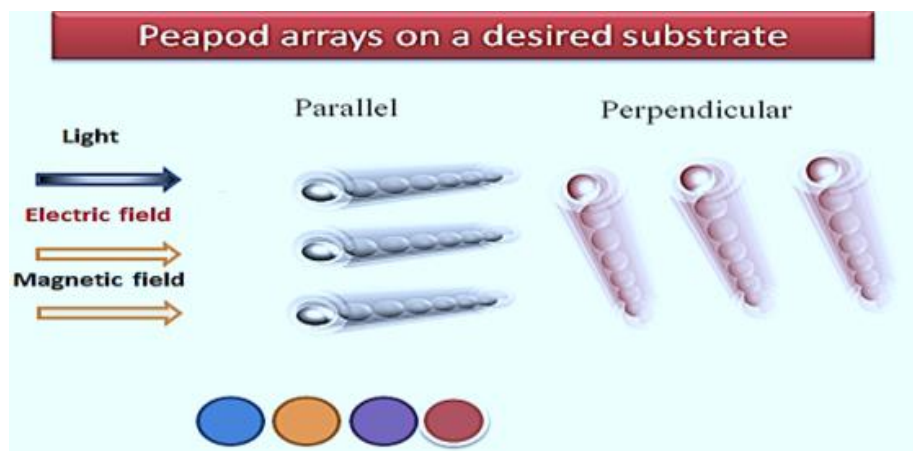
Figure 1.13. Schematic showing possible application of NPPs for fundamental studies.

1.11 References

1. Hornyak, G. L.; Dutta, J.; Tibbals, H. F.; Rao, A., *Introduction to Nanoscience*. Crc Press: 2008.
2. Drexler, K. E., Nanosystems: Molecular Machinery, Manufacturing, and Computation. John Wiley & Sons, Inc.: 1992.
3. Horikoshi, S.; Serpone, N., Introduction to Nanoparticles. Microwaves in Nanoparticle Synthesis: Fundamentals and Applications, Wiley-VCH Verlag, Weinheim **2013**.
4. Bavykin, D. V.; Walsh, F. C., Titanate and Titania Nanotubes: Synthesis, Properties and Applications. Royal Society of Chemistry: 2010.
5. Sanderson, K., Sharpest Cut from Nanotube Sword. *Nature News* **2006**.
6. Reibold, M.; Paufler, P.; Levin, A.; Kochmann, W.; Pätzke, N.; Meyer, D., Materials: Carbon Nanotubes in an Ancient Damascus Sabre. *Nature* **2006,** 444, (7117), 286-286.
7. Junk, A.; Riess, F., From an Idea to a Vision: There's Plenty of Room at the Bottom. *American journal of physics* **2006,** 74, (9), 825-830.
8. Hochella, M. F., There's Plenty of Room at the Bottom: Nanoscience in Geochemistry. *Geochimica et Cosmochimica Acta* **2002,** 66, (5), 735-743.
9. Binnig, G.; Rohrer, H., Scanning Tunneling Microscopy. *IBM Journal of research and development* **2000,** 44, (1/2), 279.
10. Kroto, H. W.; Heath, J. R.; O'Brien, S. C.; Curl, R. F.; Smalley, R. E., C 60: Buckminsterfullerene. *Nature* **1985,** 318, (6042), 162-163.
11. Piacente, V.; Gigli, G.; Scardala, P.; Giustini, A.; Ferro, D., Vapor Pressure of C60 Buckminsterfullerene. *The Journal of Physical Chemistry* **1995,** 99, (38), 14052-14057.
12. Iijima, S., Helical Microtubules of Graphitic Carbon. *nature* **1991,** 354, (6348), 56-58.
13. Monthioux, M.; Kuznetsov, V. L., Who Should be Given the Credit for the Discovery of Carbon Nanotubes? *Carbon* **2006,** 44, (9), 1621-1623.
14. Xia, B.; Lenggoro, I. W.; Okuyama, K., Novel Route to Nanoparticle Synthesis by Salt-Assisted Aerosol Decomposition. *Advanced Materials* **2001,** 13, (20), 1579-1582.
15. Zubarev, E. R., Nanoparticle Synthesis: any Way You Want it. *Nature Nanotechnology* **2013,** 8, (6), 396-397.
16. Wang, Z. L., Nanowires and Nanobelts: Materials, Properties and Devices. Volume 1: Metal and Semiconductor Nanowires. Springer Science & Business Media: 2013; Vol. 1.
17. Cheng, C.; Fan, H. J., Branched Nanowires: Synthesis and Energy Applications. *Nano Today* **2012,** 7, (4), 327-343.
18. Lohse, S. E.; Murphy, C. J., The Quest for Shape Control: a History of Gold Nanorod Synthesis. *Chemistry of Materials* **2013,** 25, (8), 1250-1261.
19. Endo, M.; Iijima, S.; Dresselhaus, M. S., *Carbon Nanotubes*. Elsevier: 2013.
20. Chhowalla, M.; Liu, Z.; Zhang, H., Two-Dimensional Transition Metal Dichalcogenide (TMD) Nanosheets. *Chemical Society Reviews* **2015,** 44, (9), 2584-2586.
21. Zhao, L.; Hu, L.; Fang, X., Growth and Device Application of CdSe Nanostructures. *Advanced Functional Materials* **2012,** 22, (8), 1551-1566.
22. Vollath, D., Nanomaterials. An Introduction to Synthesis, Properties and Applications **2008**.
23. Rao, C. N. R.; Müller, A.; Cheetham, A. K., *The Chemistry of Nanomaterials: Synthesis, Properties and Applications*. John Wiley & Sons: 2006; Vol. 1.
24. Maynard, A. D., Don't Define Nanomaterials. *Nature* **2011,** 475, (7354), 31-31.
25. Bhushan, B.; Luo, D.; Schricker, S. R.; Sigmund, W.; Zauscher, S., *Handbook of Nanomaterials Properties*. Springer Science & Business Media: 2014.
26. Valiev, R. Z.; Zhilyaev, A. P.; Langdon, T. G., *Bulk Nanostructured Materials: Fundamentals and Applications*. John Wiley & Sons: 2013.
27. Gleiter, H., Nanostructured Materials. *Advanced Materials* **1992,** 4, (7-8), 474-481.

28. Guo, W.; Kui, H., Bulk Nanostructured Alloy Formation with Controllable Grain Size. *Acta Materialia* **2000,** 48, (9), 2117-2121.

29. Azushima, A.; Kopp, R.; Korhonen, A.; Yang, D.; Micari, F.; Lahoti, G.; Groche, P.; Yanagimoto, J.; Tsuji, N.; Rosochowski, A., Severe Plastic Deformation (SPD) Processes for Metals. *CIRP Annals-Manufacturing Technology* **2008,** 57, (2), 716-735.

30. Jamaati, R.; Toroghinejad, M. R.; Edris, H.; Salmani, M. R., Fabrication of Nano/Ultra-Fine Grained IF Steel via SPD Processes: a Review. *Transactions of the Indian Institute of Metals* **2014,** 67, (6), 787-802.

31. Kharisov, B. I.; Kharissova, O. V.; Ortiz-Mendez, U., *Handbook of Less-Common Nanostructures*. CRC Press: 2012.

32. Yu, H.-D.; Regulacio, M. D.; Ye, E.; Han, M.-Y., Chemical Routes to top-down Nanofabrication. *Chemical Society Reviews* **2013,** 42, (14), 6006-6018.

33. Yin, Y.; Talapin, D., The Chemistry of Functional Nanomaterials. *Chemical Society Reviews* **2013,** 42, (7), 2484-2487.

34. Yadav, T. P.; Yadav, R. M.; Singh, D. P., Mechanical milling: a top down Approach for the Synthesis of Nanomaterials and Nanocomposites. *Nanoscience and Nanotechnology* **2012,** 2, (3), 22-48.

35. Manfrinato, V. R.; Zhang, L.; Su, D.; Duan, H.; Hobbs, R. G.; Stach, E. A.; Berggren, K. K., Resolution Limits of Electron-Beam Lithography toward the Atomic Scale. *Nano Letters* **2013,** 13, (4), 1555-1558.

36. Jiao, L.; Xie, L.; Dai, H., Densely Aligned Graphene Nanoribbons at~ 35 nm pitch. *Nano Research* **2012,** 5, (4), 292-296.

37. Zeng, H.; Du, X. W.; Singh, S. C.; Kulinich, S. A.; Yang, S.; He, J.; Cai, W., Nanomaterials via Laser Ablation/Irradiation in Liquid: a Review. *Advanced Functional Materials* **2012,** 22, (7), 1333-1353.

38. Rao, C. N. R.; Müller, A.; Cheetham, A. K., *Nanomaterials Chemistry: Recent Developments and New Directions*. John Wiley & Sons: 2007.

39. Nogi, K.; Naito, M.; Yokoyama, T., *Nanoparticle Technology Handbook*. Elsevier: 2012.

40. Altavilla, C.; Ciliberto, E., Inorganic Nanoparticles: Synthesis, Applications, and Perspectives. CRC Press: 2010.

41. Sun, Y., Controlled Synthesis of Colloidal Silver Nanoparticles in Organic Solutions: empirical rules for nucleation engineering. *Chemical Society Reviews* **2013,** 42, (7), 2497-2511.

42. Gao, G., Nanostructures and Nanomaterials: Synthesis, Properties and Applications. In London: Imperial College Press: 2004.

43. Cushing, B. L.; Kolesnichenko, V. L.; O'Connor, C. J., Recent Advances in the Liquid-Phase Syntheses of Inorganic Nanoparticles. *Chemical reviews* **2004,** 104, (9), 3893-3946.

44. Porter, D. A.; Easterling, K. E.; Sherif, M., *Phase Transformations in Metals and Alloys, (Revised Reprint)*. CRC press: 2009.

45. Robb, D. T.; Privman, V., Model of Nanocrystal Formation in Solution by Burst Nucleation and Diffusional Growth. *Langmuir* **2008,** 24, (1), 26-35.

46. Park, J.; Joo, J.; Kwon, S. G.; Jang, Y.; Hyeon, T., Synthesis of Monodisperse Spherical Nanocrystals. *Angewandte Chemie International Edition* **2007,** 46, (25), 4630-4660.

47. Murray, C.; Norris, D. J.; Bawendi, M. G., Synthesis and Characterization of Nearly Monodisperse CdE (E= sulfur, selenium, tellurium) Semiconductor Nanocrystallites. *Journal of the American Chemical Society* **1993,** 115, (19), 8706-8715.

48. Yin, Y.; Alivisatos, A. P., Colloidal Nanocrystal Synthesis and the Organic–Inorganic Interface. *Nature* **2005,** 437, (7059), 664-670.

49. Williams, R.; Yocom, P.; Stofko, F., Preparation and Properties of Spherical Zinc Sulfide Particles. *Journal of Colloid and Interface Science* **1985,** 106, (2), 388-398.

50. Voorhees, P. W., The Theory of Ostwald ripening. *Journal of Statistical Physics* **1985,** 38, (1-2), 231-252.

51. Sidhaye, D. S.; Prasad, B., Many Manifestations of Digestive Ripening: Monodispersity, Superlattices and Nanomachining. *New Journal of Chemistry* **2011,** 35, (4), 755-763.

52. Thanh, N. T.; Maclean, N.; Mahiddine, S., Mechanisms of Nucleation and Growth of Nanoparticles in Solution. *Chemical Reviews* **2014,** 114, (15), 7610-7630.

53. Henglein, A., Small-particle research: Physicochemical Properties of Extremely Small Colloidal Metal and Semiconductor Particles. *Chemical Reviews* **1989,** 89, (8), 1861-1873.

54. Panigrahi, S.; Kundu, S.; Ghosh, S.; Nath, S.; Pal, T., General Method of Synthesis for Metal Nanoparticles. *Journal of Nanoparticle Research* **2004,** 6, (4), 411-414.

55. Tan, Y.; Li, Y.; Zhu, D., Noble Metal Nanoparticles. *Encyclopedia of nanoscience and nanotechnology* **2004,** 8, 9-40.

56. Tao, A. R.; Habas, S.; Yang, P., Shape Control of Colloidal Metal Nanocrystals. *Small* **2008,** 4, (3), 310-325.

57. Goulet, P. J.; Bourret, G. R.; Lennox, R. B., Facile Phase Transfer of Large, Water-Soluble Metal Nanoparticles to Nonpolar Solvents. *Langmuir* **2012,** 28, (5), 2909-2913.

58. Adireddy, S. R., High Yield Solvothermal Synthesis of Hexaniobate Based Nanocomposites via the Capture of Preformed Nanoparticles in Scrolled Nanosheets. **2013**.

59. Brown, L. O.; Hutchison, J. E., Controlled Growth of Gold Nanoparticles During Ligand Exchange. *Journal of the American Chemical Society* **1999,** 121, (4), 882-883.

60. Caruntu, D.; Rostamzadeh, T.; Costanzo, T.; Parizi, S. S.; Caruntu, G., Solvothermal Synthesis and Controlled Self-Assembly of Monodisperse Titanium-Based Perovskite Colloidal Nanocrystals. *Nanoscale* **2015,** 7, (30), 12955-12969.

61. Lai, J.; Niu, W.; Luque, R.; Xu, G., Solvothermal Synthesis of Metal Nanocrystals and their Applications. *Nano Today* **2015**.

62. Walton, R. I., Subcritical Solvothermal Synthesis of Condensed Inorganic Materials. *Chemical Society Reviews* **2002,** 31, (4), 230-238.

63. Demazeau, G., Review. Solvothermal Processes: Definition, Key Factors Governing the Involved Chemical Reactions and New Trends. *Zeitschrift für Naturforschung B* **2010,** 65, (8), 999-1006.

64. Adireddy, S.; Lin, C.; Cao, B.; Zhou, W.; Caruntu, G., Solution-Based Growth of Monodisperse Cube-Like $BaTiO_3$ Colloidal Nanocrystals. *Chemistry of Materials* **2010,** 22, (6), 1946-1948.

65. Yang, H. G.; Liu, G.; Qiao, S. Z.; Sun, C. H.; Jin, Y. G.; Smith, S. C.; Zou, J.; Cheng, H. M.; Lu, G. Q., Solvothermal Synthesis and Photoreactivity of Anatase TiO_2 Nanosheets with Dominant {001} Facets. *Journal of the American Chemical Society* **2009,** 131, (11), 4078-4083.

66. Wu, W.; Hao, R.; Liu, F.; Su, X.; Hou, Y., Single-Crystalline α-Fe_2O_3 Nanostructures: Controlled Synthesis and High-Index Plane-Enhanced Photodegradation by Visible Light. *Journal of Materials Chemistry A* **2013,** 1, (23), 6888-6894.

67. Yu, S.-H.; Yang, J.; Han, Z.-H.; Zhou, Y.; Yang, R.-Y.; Qian, Y.-T.; Zhang, Y.-H., Controllable Synthesis of Nanocrystalline CdS with Different Morphologies and Particle Sizes by a Novel Solvothermal Process. *Journal of Materials Chemistry* **1999,** 9, (6), 1283-1287.

68. Gautam, U. K.; Rajamathi, M.; Meldrum, F.; Morgan, P.; Seshadri, R., A Solvothermal Route to Capped CdSe Nanoparticles. *Chemical Communications* **2001**, (7), 629-630.

69. Nicolosi, V.; Chhowalla, M.; Kanatzidis, M. G.; Strano, M. S.; Coleman, J. N., Liquid Exfoliation of Layered Materials. *Science* **2013,** 340, (6139), 1226419.

70. Auerbach, S. M.; Carrado, K. A.; Dutta, P. K., *Handbook of Layered Materials*. CRC Press: 2004.

71. Coleman, J. N.; Lotya, M.; O'Neill, A.; Bergin, S. D.; King, P. J.; Khan, U.; Young, K.; Gaucher, A.; De, S.; Smith, R. J., Two-Dimensional Nanosheets Produced by Liquid Exfoliation of Layered Materials. *Science* **2011,** 331, (6017), 568-571.

72. Golberg, D.; Bando, Y.; Huang, Y.; Terao, T.; Mitome, M.; Tang, C.; Zhi, C., Boron Nitride Nanotubes and Nanosheets. *ACS Nano* **2010,** 4, (6), 2979-2993.

73. Chen, Y. I., Nanotubes and Nanosheets: Functionalization and Applications of Boron Nitride and Other Nanomaterials. CRC Press: 2015.

74. Chernova, N. A.; Roppolo, M.; Dillon, A. C.; Whittingham, M. S., Layered Vanadium and Molybdenum Oxides: Batteries and Electrochromics. *Journal of Materials Chemistry* **2009,** 19, (17), 2526-2552.

75. Huang, P.-R.; He, Y.; Cao, C.; Lu, Z.-H., Impact of Lattice Distortion and Electron Doping on α-MoO$_3$ Electronic Structure. *Scientific Reports* **2014,** 4.

76. Domen, K.; Kudo, A.; Shibata, M.; Tanaka, A.; Maruya, K.-I.; Onishi, T., Novel Photocatalysts, Ion-Exchanged K$_4$Nb$_6$O$_{17}$, with a Layer Structure. *Journal of the Chemical Society, Chemical Communications* **1986**, (23), 1706-1707.

77. Kudo, A.; Sakata, T., Effect of Ion Exchange on Photoluminescence of Layered Niobates K$_4$Nb$_6$O$_{17}$ and KNb$_3$O$_8$. *The Journal of Physical Chemistry* **1996,** 100, (43), 17323-17326.

78. Yao, Y., Controlled Attachment of Nanoparticles to Layered Oxides. **2012**.

79. Ma, R.; Bando, Y.; Sasaki, T., Directly Rolling Nanosheets into Nanotubes. *The Journal of Physical Chemistry B* **2004,** 108, (7), 2115-2119.

80. Phases, P. A. R.-P., Exfoliation into Sheets and Nanotubes for Assembly of Perovskite Thin Films Schaak, Raymond E.; Mallouk, Thomas E. *Chemistry of Materials* **2000,** 12, (11), 3427-3434.

81. Coleman, J. N., Liquid Exfoliation of Defect-Free Graphene. *Accounts of Chemical Research* **2012,** 46, (1), 14-22.

82. Meyyappan, M., Carbon Nanotubes: Science and Applications. CRC press: 2004.

83. Tománek, D.; Enbody, R. J., *Science and Application of Nanotubes*. Springer Science & Business Media: 2000.

84. Iijima, S., Carbon Nanotubes: Past, Present, and Future. *Physica B: Condensed Matter* **2002,** 323, (1), 1-5.

85. Gogotsi, Y., *Nanomaterials Handbook*. CRC press: 2006.

86. Adireddy, S.; Yao, Y.; He, J.; Wiley, J. B., Rapid Solvothermal Fabrication of Hexaniobate Nanoscrolls. *Materials Research Bulletin* **2013,** 48, (9), 3236-3241.

87. Yao, Y.; Chaubey, G. S.; Wiley, J. B., Fabrication of Nanopeapods: Scrolling of Niobate Nanosheets for Magnetic Nanoparticle Chain Encapsulation. *Journal of the American Chemical Society* **2011,** 134, (5), 2450-2452.

88. Smith, B. W.; Monthioux, M.; Luzzi, D. E., Encapsulated C60 in Carbon Nanotubes. *Nature* **1998,** 396, 323-324.

89. Ajayan, P.; Stephan, O.; Redlich, P.; Colliex, C., Carbon Nanotubes as Removable Templates for Metal Oxide Nanocomposites and Nanostructures. **1995**.

90. Ajayan, P. M., Capillarity-Induced Filling of Carbon Nanotubes. *Nature* **1993,** 361, (6410), 333-334.

91. Luzzi, D. E.; Smith, B. W., Nanoscopic Hybrid Materials: The Synthesis, Structure and Properties of Peapods, Cats and Kin. In *Science and Application of Nanotubes*, Springer: 2002; pp 67-76.

92. Willets, K. A.; Van Duyne, R. P., Localized Surface Plasmon Resonance Spectroscopy and Sensing. *Annu. Rev. Phys. Chem.* **2007,** 58, 267-297.

93. Kim, H.; Park, S.; Jin, C.; Lee, C., Enhanced Photoluminescence in Au-Embedded ITO Nanowires. *ACS applied materials & interfaces* **2011,** 3, (12), 4677-4681.

94. Chen, P.-H.; Hsieh, C.-H.; Chen, S.-Y.; Wu, C.-H.; Wu, Y.-J.; Chou, L.-J.; Chen, L.-J., Direct Observation of Au/Ga$_2$O$_3$ Peapodded Nanowires and Their Plasmonic Behaviors. *Nano Letters* **2010,** 10, (9), 3267-3271.

95. Hsieh, C.-H.; Chou, L.-J.; Lin, G.-R.; Bando, Y.; Golberg, D., Nanophotonic switch: Gold-in-Ga$_2$O$_3$ Peapod Nanowires. *Nano letters* **2008,** 8, (10), 3081-3085.

96. Zhou, W.; Sun, L.; Yu, T.; Zhang, J.; Gong, H.; Fan, H., The Morphology of Au@ MgO Nanopeapods. *Nanotechnology* **2009,** 20, (45), 455603.

97. Hunyadi, S. E.; Murphy, C. J., Tunable One-Dimensional Silver-Silica Nanopeapod Architectures. *The Journal of Physical Chemistry B* **2006,** 110, (14), 7226-7231.

98. Yang, Y.; Li, L.; Li, W., Plasmon Absorption of Au-in-CoAl$_2$O$_4$ Linear Nanopeapod Chains. *The Journal of Physical Chemistry C* **2013,** 117, (27), 14142-14148.

99. Liu, L.; Lee, W.; Scholz, R.; Pippel, E.; Gösele, U., Tailor-Made Inorganic Nanopeapods: Structural Design of Linear Noble Metal Nanoparticle Chains. *Angewandte Chemie* **2008,** 120, (37), 7112-7116.

100. Cong, V. T.; Ganbold, E.-O.; Saha, J. K.; Jang, J.; Min, J.; Choo, J.; Kim, S.; Song, N. W.; Son, S. J.; Lee, S. B., Gold Nanoparticle Silica Nanopeapods. *Journal of the American Chemical Society* **2014,** 136, (10), 3833-3841.

101. Adireddy, S.; Carbo, C. E.; Rostamzadeh, T.; Vargas, J. M.; Spinu, L.; Wiley, J. B., Peapod-Type Nanocomposites through the In Situ Growth of Gold Nanoparticles within Preformed Hexaniobate Nanoscrolls. *Angewandte Chemie International Edition* **2014,** 53, (18), 4614-4617.

Chapter 2 Rapid Large-Scale Synthesis of Vanadate Nanoscrolls with Controllable Lengths[*]

2.1 Introduction

Vanadate nanoscrolls (NScs) have been explored for a variety of applications including energy storage,[1] catalysis,[2] sensors,[3] as well as more fundamental studies of behavior.[4] Several researchers for example have investigated lithium intercalation into these materials for their use in cathodes[5] where the flexible interlayer spacing available may better withstand volume changes tied to electrode instabilities. More fundamental studies have probed electronic, magnetic, and topological properties.[4b, 6]

Vanadate NScs, exhibiting well-ordered multiwalled tubular structures, were first synthesized by Spehr *et al.*[7] Preparation of vanadate NScs usually occurs through a solvothermal (ST) treatment of lamellar vanadium oxide in the presence of organic structure-directing agents (SDA).[5b, 8] In a typical synthesis, vanadium oxide precursor is mixed with either primary alkyl amines or diamines, in water and ethanol. After aging and ST-treatment of the mixture over several days, black VO_x NScs can be obtained.[5b, 7-9] Several research groups have shown that interlayer-spacings in the VO_x NScs are controllable by varying the length of the different SDA.[5b, 10] It has also been shown that the amines can be exchanged with various cations including alkali (Na^+, K^+), alkaline earth (Mg^{2+}, Ca^{2+}, Sr^{2+}) and transition-metal (Fe^{2+}, Co^{2+}, Ni^{2+}, Cu^{2+}) ions.[11] The smaller cations result in a reduction of the interlayer-spacings while retaining the NScs morphology.[11b]

Since the discovery of vanadate NScs, several research groups have investigated the effect of synthetic parameters on their formation. For example, Krumeich *et al.*[6d] studied different molar ratios of the vanadium oxide precursor to the primary amine (e.g., 2:1, 3:1 and 4:1) with the amount of water and ethanol kept constant. They reported that NScs could be obtained with molar ratios of 2:1 and 3:1, while a molar ratio of 4:1 led to the formation of lamellar structures rather than NScs. The effect of aging time as well as hydrothermal reaction time and temperature

---

were also examined.[5b, 6d] Researchers reported that 7 days of hydrothermal treatment at 180 °C is needed for the formation of NScs. By extending the aging time from 2 to 4 days prior to ST treatment, formation time of NScs could be reduced to six days. Though vanadate NScs are already available in gram quantities,[10b] to the best of our knowledge, the minimum time reported for the formation of high-quality vanadate NScs is at least five days[5b, 6d, 7-9, 10a, 11a, 12] and there are no reports on the syntheses with directed lengths. Herein, we report a rapid, large scale synthetic approach where vanadate NScs in distinct size ranges can be realized in as little as 2h.

2.2 Experimental Section

Materials. Hexane (anhydrous, 95%), dodecylamine (98%), octadecylamine (98%), and vanadium (V) oxide ($\geq$ 99.6%), were purchased from Sigma-Aldrich. ACS/USP graded Ethanol (PHARMCO-AAPER), was used in all preparations.

Solvothermal Synthesis of V_2O_5 nanoscrolls with two different average length 383±81nm and 816±135 nm. Short-Length VO_x NSs (383 nm) were synthesized using the following procedure. Dodecylamine (2 g, 10.81 mmol) was dissolved in 10 mL of ethanol. After adding V_2O_5 (1.83 g, 10 mmol) to the stirring mixture, the solution turned into an orange gel. The final mixture was transferred into a 23 mL Teflon-lined stainless-steel autoclave and hydrothermally treated at 250 °C for 1.5 h after which it was cooled down to room temperature (1 °C/min). The obtained black product was washed first with ethanol and then hexane in order to remove the unreacted amine. vanadate NScs were finally separated by centrifugation. Utilizing the same experimental conditions, except that the amount of V_2O_5 was decreased (0.915 g, 5 mmol), led to the formation of V_2O_5 NSCs with an average length of 816 nm. In both cases, reactions could easily be scaled up so that approximately 20 g of product per synthesis obtained using a larger Teflon-lined (100 mL) stainless-steel autoclave.

Solvothermal Synthesis of V_2O_5 nanoscrolls with an average length of 3.3±1µm. Dodecylamine (2 g, 10.81 mmol), V_2O_5 (1.83 g, 10 mmol), and 10 mL of distilled water were mixed and mechanically stirred inside a 23 mL Teflon. The mixture then hydrothermally treated at 250 °C for 2h after which it was cooled down to room temperature (1 °C/min). The obtained black product was washed and separated from the unreacted amine as described above for the

28

shorter NScs. This synthesis could also be scaled up so that approximately 20 g of product per synthesis obtained using a larger Teflon-lined (100 mL) stainless-steel autoclave.

In a similar experiment, an equal mixture of ethanol and DI-water were used (5 mL each). Dodecylamine (2 g, 10.81 mmol) was dissolved in 5 mL of ethanol with stirring. Then an aqueous solution of V_2O_5 (1.83 g, 10 mmol) in 5 mL water was added. The combination turned to an orange gel. Hydrothermal treatment of the final mixture at 250 °C for 2h led to the formation of NScs with similar average lengths. Time and temperature studies were also carried out on this system to investigate the effects on the formation of VO_x NScs. Examining the same ethanol-water mixture, reactants were treated at 180 °C, 230 °C, and 250 °C for different time intervals.

In order to examine the formation of NScs with respect to the molar ratio of dodecylamine and vanadium pentoxide to the solvent, 5.4 mmol dodecylamine, 5 mmol V_2O_5, and either 10mL or 15mL of ethanol were solvothermally treated at 250 °C for 2h. TEM results show the formation of ribbon fragments rather than NScs.

Characterization. The samples were characterized with a TEM JEOL 2010 operated at an accelerating voltage of 200 kV. The unit is equipped with EDAX genesis energy dispersive spectroscopy (EDS) system. For transmission electron microscopy (TEM) measurements, samples were dispersed in toluene and then drop cast onto a 200 mesh carbon-coated copper grid. The same sample drop cast method was used for scanning electron microscopy (SEM) observations. SEM was carried out on a Carl Zeiss 1530 VP field-emission scanning electron microscope (FESEM). A Philips X-Pert PW 3040 MPD equipped with a curved graphite monochromator operating at 45 kV accelerating voltage and 40 mA current, was used to collect XRD data. Formation of layered structures as well as the scrolling process were investigated on an Asylum Research MFP-3D atomic force microscopy (AFM) at room temperature working in the dual amplitude resonance tracking (DART) mode. XPS measurements were conducted on a VG Scientific MKII system using either an Al Kα (hv = 1486.6 eV) or a Mg Kα excitation source (hv = 1253 eV). The pressure in the chamber during analysis was < 5×10^{-8} mbar. Peak fitting was performed with custom VBA program in Microsoft Excel using Voigt profiles together with a Shirley background function. The satellite peaks were accounted for by applying known relative offsets and intensities with respect to the primary excitation of each source.

Unless otherwise stated the displayed spectra and binding energies have not been subjected to any energy correction.

2.3 Results

Figures 2.1 and 2.2 present high magnification TEM images of multiwalled vanadate NScs with equally-spaced parallel layers. The synthesis of short vanadate NScs was readily achieved using a ST treatment (2 h, 250 °C) with dodecylamine (2 g, 10.81 mmol), V_2O_5 (1.83 g, 10 mmol) and ethanol (10 mL). The TEM images (Figure 2.1a and b) show the product exclusively composed of NScs ranging in length from 140 - 600 nm. The average length was found to be about 383±81 nm, based on the analysis of a series of low magnification TEM images (Supporting Information, Figure 2.2a and b).

The lengths of vanadate NScs could be increased to an average of *ca.* 800 nm by increasing the amine to vanadium precursor molar ratio from 1.081 to 2.016 (10.81 mmol dodecylamine and 5 mmol V_2O_5) while maintaining the same solvent and reaction conditions (10 mL ethanol, 2h, 250 °C). TEM images (Figure 2.1c and d) of the synthesized NScs show the presence of well-formed tubular structures ranging from 450 nm to 1200 nm with average lengths of 816±135 nm (Supporting Information, Figure 2.2c, and d).

For the production of even longer NScs, ethanol was replaced with either water or a mixture of water (5 mL) and ethanol (5 mL). In both cases, the ST treatment (250 °C, 2h) led to the formation of NScs ranging from 0.5 µm to 6 µm (Figure 2.1e, and f, and Figure 2.3) with average lengths of 3.3±1 µm. Statistical analysis on a series of low magnification TEM images show that the longer NScs typically have larger inner and outer diameters as well as a larger number of turns within the scroll (Figure 2.1 and Figure 2.2). In some instances, clear evidence for non-registry of the layers can be seen on the outer layers (SEM images, Figure 2.4, and red arrows in Figure 2.1f).
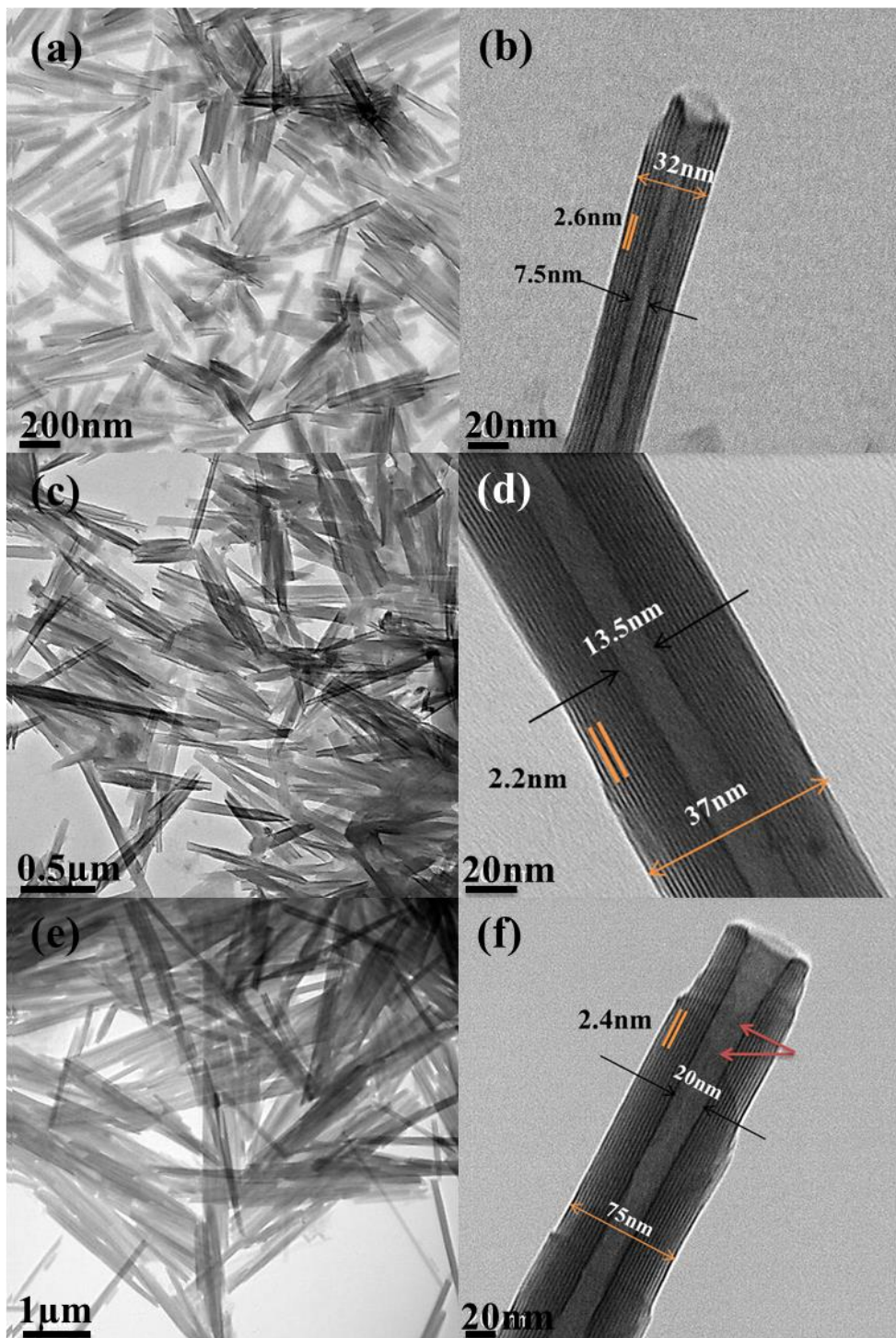
Figure 2.1. Low and high magnification TEM images of VO$_x$ NScs with three different average lengths: a), b) 383±81 nm, c), d) 816±135 nm, and e), f) 3.3±1 µm. Lengths adjacent to arrows in b, d, and f highlight inner and outer diameters and interlayer spacings. Double red arrows in f indicate scrolled structure as opposed to concentric tubular structure.
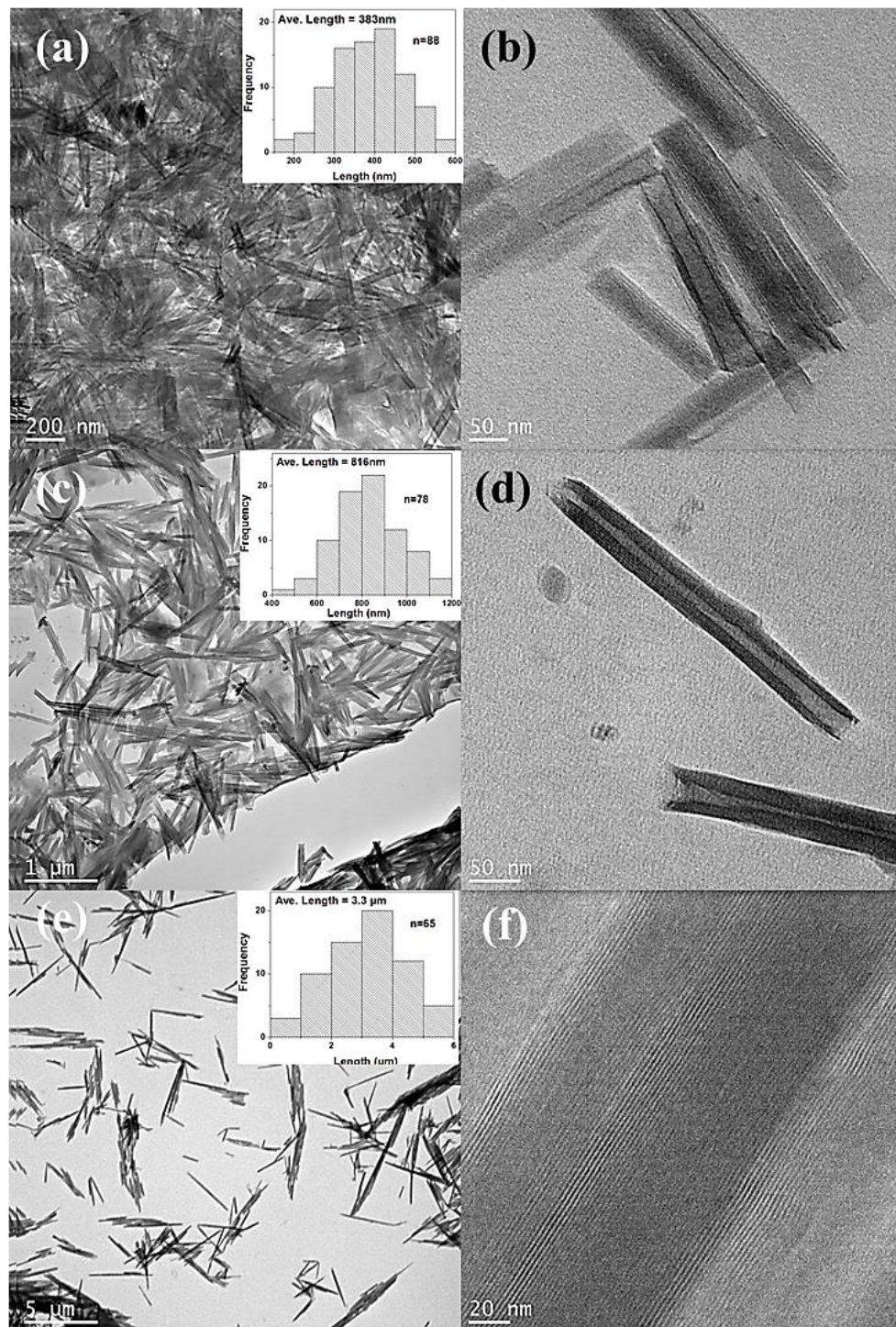
Figure 2.2. TEM images of synthesized V_2O_5 NScs with three different average lengths; (a, b) 383±81 nm, (c, d) 816±135 nm, and (e, f) 3.3±1 µm. The insets show the corresponding NScs lengths distributions obtained using low magnification TEM images.
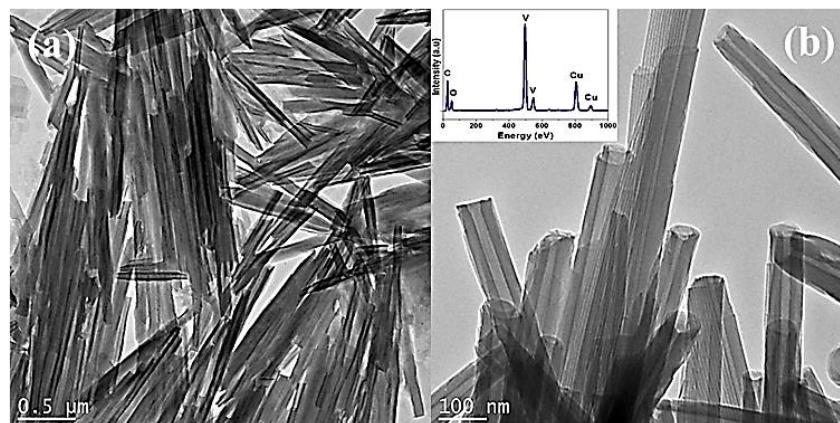
Figure 2.3. Different magnification TEM images of NScs synthesized after 2h solvothermal treatment at 250 °C using water as solvent. The inset in (b) shows the corresponding EDS data; copper is from TEM grid.
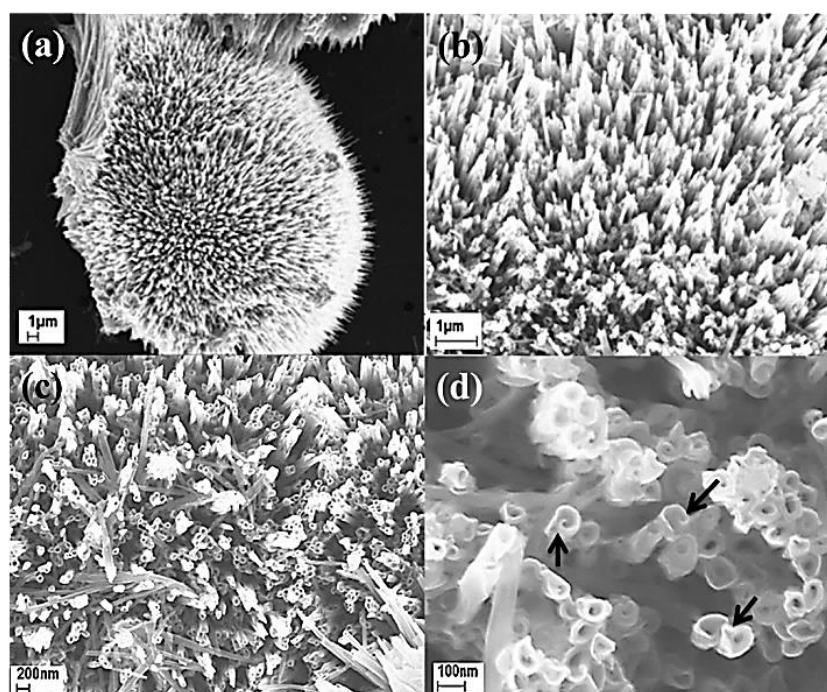
Figure 2.4. SEM images of different magnifications showing the oriented assemblies of vanadate NScs and their morphologies down the length of the NScs. These urchin-like structures obtained after sonication and following drop-casting of concentrated NScs dispersed in toluene (~200 mg/mL). Arrows in (d) show the tubular structures are mainly scrolled tubes and in some instances the scroll ends have an uneven registry. NScs were synthesized using both water and ethanol as solvent (250 °C, 2h).

This presumably is due to an asymmetry in the original parent nanosheet, though it may have also occurred as an uneven "tearing" when the scroll detached from the parent. Additionally notable is that regardless of the lengths of obtained NScs, the majority of tubular structures are open at both ends similar to what has previously been reported.[5b]

X-ray diffraction patterns of VO_x NScs with the three different lengths are shown in Figure 2.5. The low-angle reflections of the vanadate (*00l*) are related to the well-ordered layer structure within the scroll. The interlayer spacing for different lengths NScs is calculated using low-angle reflections (*00l*), which correspond to *d*-spacing values of 29.3(2), 28.73(3), and 26.93(2) Å, for NScs with average lengths of 383±81nm, 816±135 nm, and 3.3±1 μm, respectively. These changes in interlayer spacings can be related to the existence of different amounts of surfactant located between the vanadium oxide layers.[5b, 6d, 7] Using the TEM images of the NScs shown in Figure 2.1b, d, and f, the interlayer spacing for different lengths of NScs were found to be 26, 22, and 24 Å respectively.
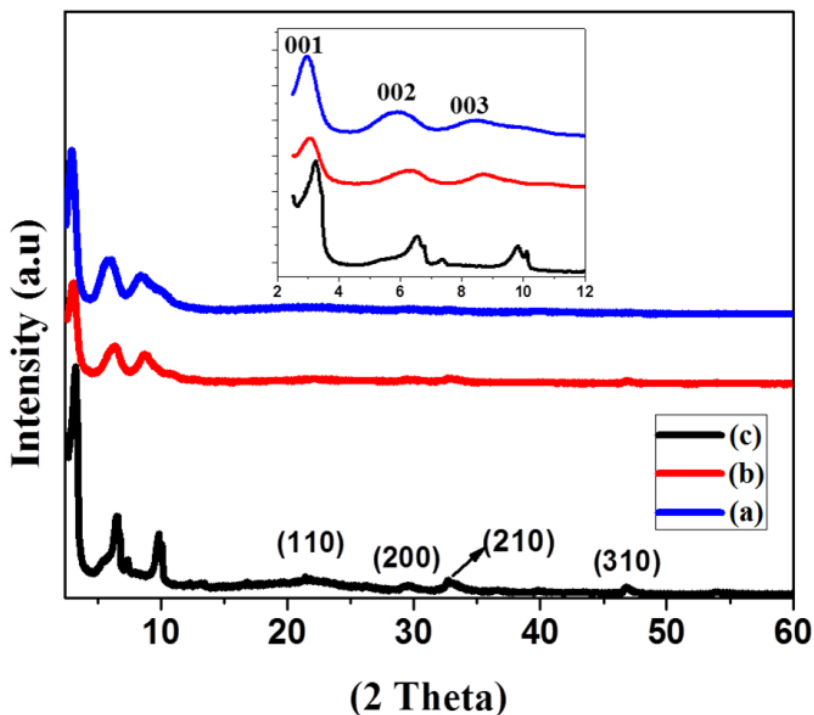
Figure 2.5. Powder XRD pattern of vanadate NScs with different average lengths (a) 3.3±1μm, (b) 816±135 nm, and (c) 383±81 nm. Low angle reflections are highlighted in the insets.

Supplementary TEM analyses showed that different NScs can, however, have different interlayer spacings. The interlayer spacing can be further tuned with a change in the length of the surfactant chain as a structure-directing agent. [5b, 6d, 7, 10b]

A change in interlayer spacing from 2.7 nm to 3.2 nm was observed when dodecylamine was replaced by octadecylamine (Figure 2.6). In the case of long NScs with average lengths of 3.3±1 μm, some of the low angle reflections have shoulders which likely is related to the existence of different interlayer spacings in different NScs.[13]
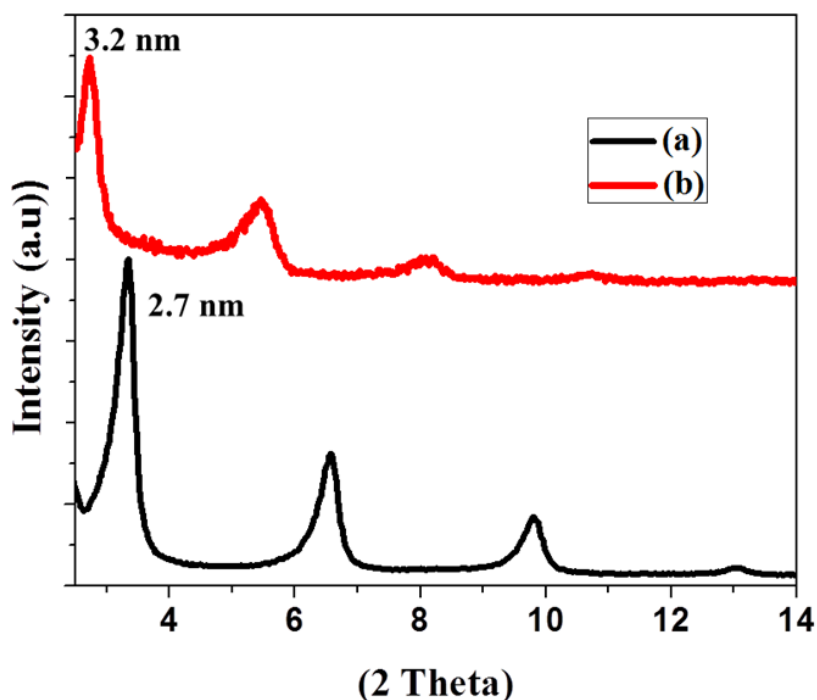
Figure 2.6. XRD patterns of synthesized samples using two different structure-directing templates; (a) dodecylamine and (b) octadecylamine. Samples were synthesized using both ethanol and water as solvent.

Two types of asymmetric NScs with either different inter-layer spacings in opposite side of NScs or uneven interlayer spacings for the inside versus the outside of the NScs (Figure 2.7) as well as other structural defects were also observed in some of the synthesized NScs (Figure 2.8).
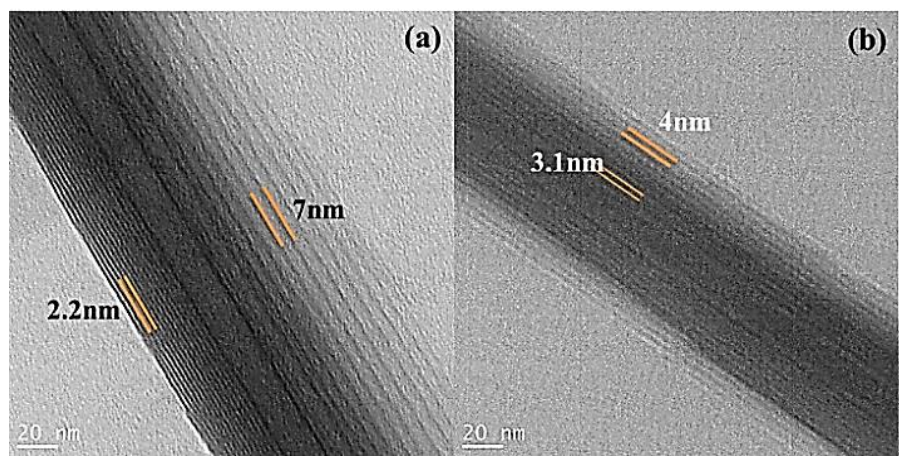
Figure 2.7. TEM images showing layers spacing of a) an asymmetric NScs with different inter-layer spacings in opposite side of NScs, b) uneven interlayer spacings for the inside versus outside of the NScs.
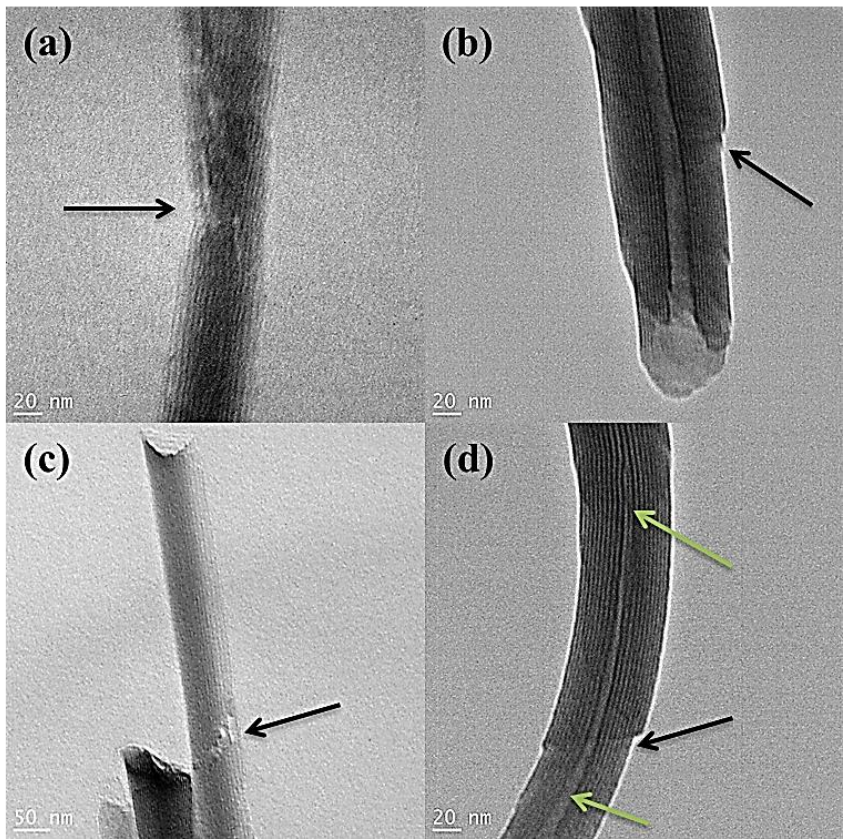
Figure 2.8. TEM images of structural defects observed in vanadate NScs synthesized using only water as solvent and dodecylamine as structure-directing agent (250 °C for 2 h).

The low intensity high-angle reflections (*hk0*), highlighted in the Figure 2.5, are related to the two-dimensional structure of the layers and can be indexed according to a square lattice with $a = 6.1$ Å. There are some differences, however, observable for these samples. In the case of long NScs (3.3μm) at least one additional reflection ($2\theta = 36.6°$) is seen, assigned to the (220),[14] which is absent in the XRD patterns of the other samples. This peak may imply a higher crystallinity for the 3.3 μm NScs. XRD patterns and electrochemical properties of well-ordered and oxygen-deficient ("defect-rich") vanadate NScs were previously investigated by Sun *et al.*[14] They also observed fewer reflections in the case of defect-rich vanadate NScs. The existence of defects was further shown to increase the electrochemical performance of NScs.[14]

In order to investigate the effect of time and temperature on the formation of vanadate NScs, several experiments were performed using the same reaction compositions. The obtained results confirmed the formation of lamellar structures prior to scrolling and showed that higher temperatures accelerate the rolling process. The X-ray diffraction patterns of V_2O_5 used as the vanadium precursor (Figure 2.9a) as well as synthesized structures obtained after different ST time intervals (Figure 2.9b-f) are presented in Figure 2.9.

XRD pattern of the orange gel obtained right after adding an aqueous solution of V_2O_5 to the stirring mixture of ethanol, and dodecylamine (see experimental procedure), show the formation of layered product with a different XRD pattern (Figure 2.9b) relative to the initial starting materials. This simply implies that no aging and ST treatment is needed for the intercalation of surfactant between the layers. Using the low-angle reflection peak (*001*), the interlayer spacing is calculated which corresponds to a *d*-spacing of approximately 24.2(2) Å. After ST treatment of the mixture at 250 °C for 15 and 30 minutes, the already formed layered structures is preserved and interlayer spacings does not significantly change. Any small variations in the interlayer spacings could be related to the rearrangement of the surfactant located between the layers due to the temperature/pressure effects during the ST treatment. TEM observation further confirms the formation of the layered structure at this step (Figure 2.10a and b).
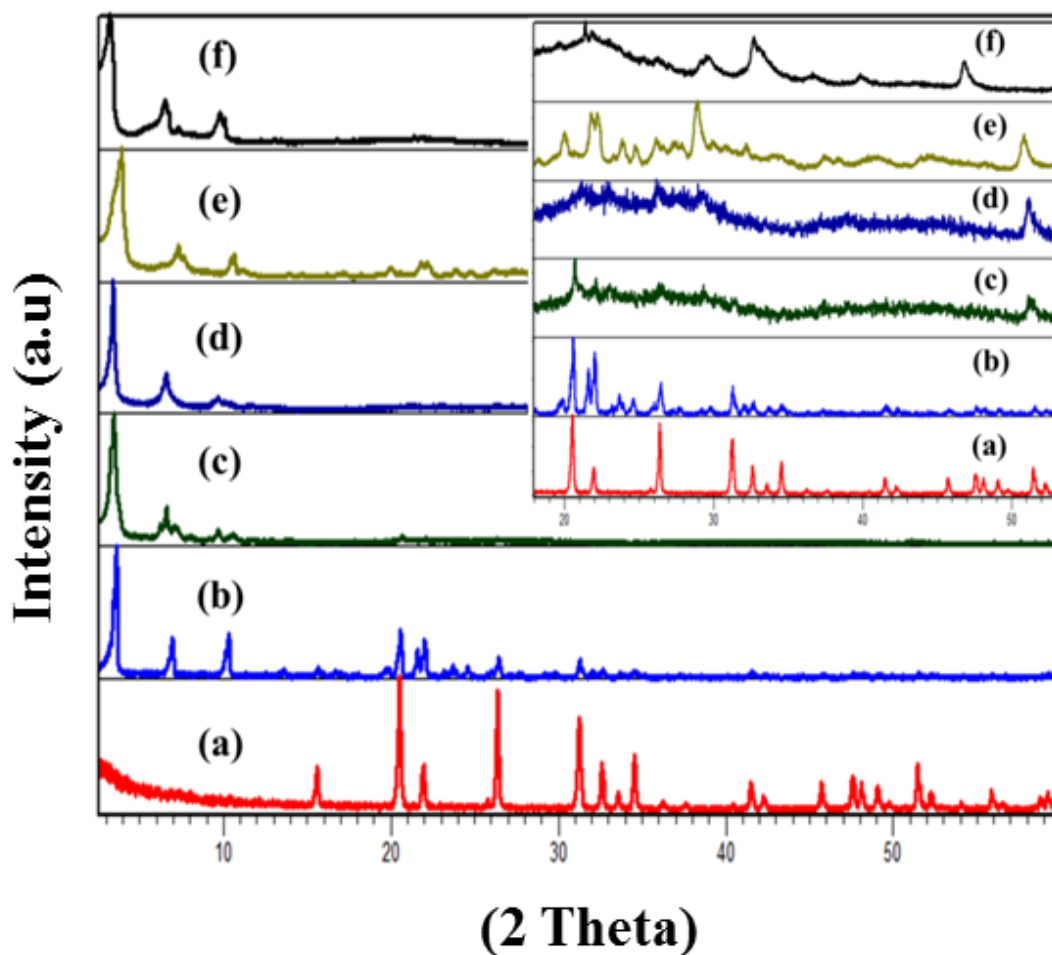
Figure 2.9. XRD patterns of (a) V_2O_5 reagent (b) orange gelatinous sample before ST treatment, (c, d, e, and f) after 0.25, 0.5, 1, and 2 h ST treatment at 250 °C, respectively. High angle reflections are highlighted in the inset. Samples were synthesized using both ethanol and water as solvent and dodecylamine as structure-directing template.

It can be seen, however, from the inset of Figure 2.9c and d that the crystallinity of the samples obtained after 15 and 30 minutes is significantly diminished relative to the starting gel. From the high angle reflections, the existence of new peaks related to the initial evolution of a new structure could be detected for the sample obtained after 1h of ST treatment (Figure 2.9e). The first low angle reflection shows a clear shift to a higher angle that corresponds to *d*-spacing values of approximately 22.2(2) Å (Figure 2.9e).
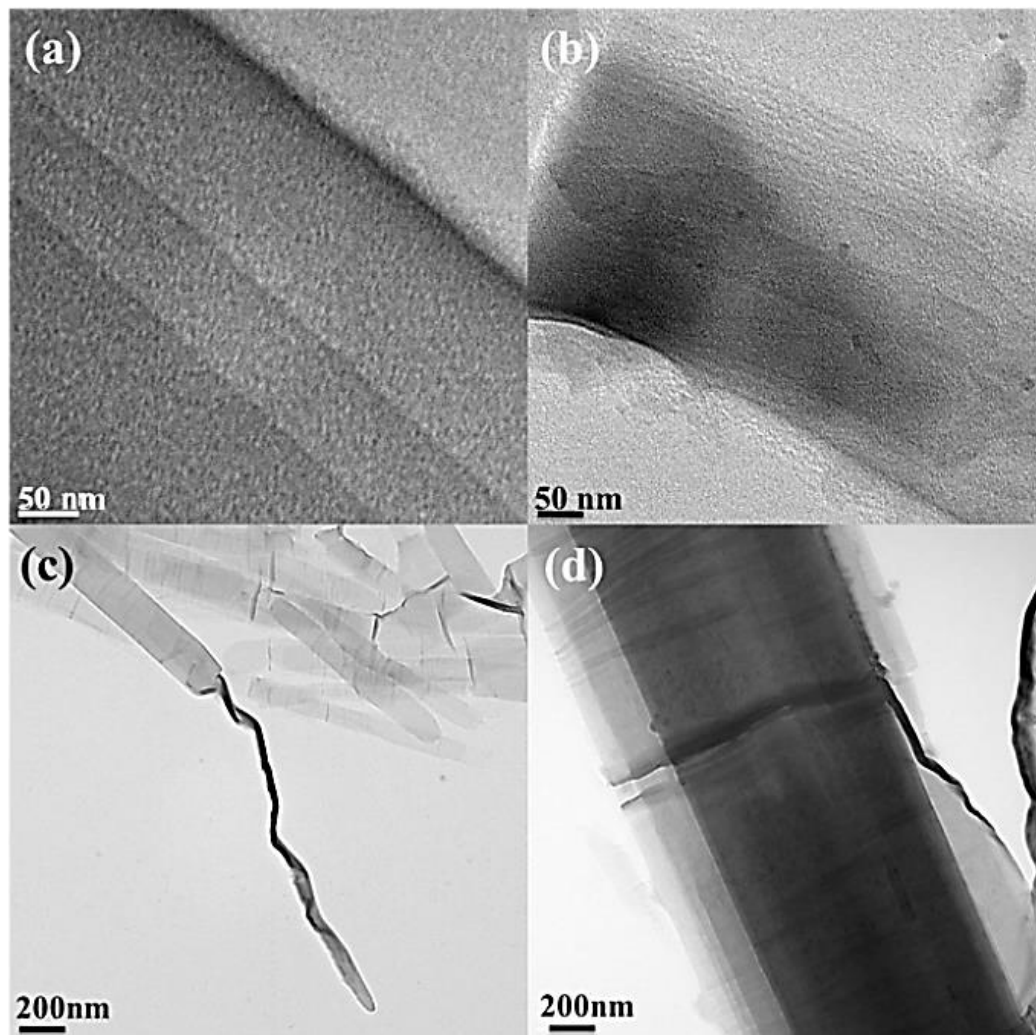
Figure 2.10. TEM images of ST-treated samples at 250 °C for a) 15 min., b) 30 min., c) and d) 1h. Samples were synthesized using both ethanol and water as solvent and dodecylamine as structure-directing template.

In Figure 2.10, TEM observations show the scrolling of the layered structure is initiated (Figure 2.10c and d) after 1h of ST-treatment. Finally, 2h ST treatment led to the complete formation of vanadate NScs as shown in Figure 2.1e and 2.1f. ST treatment of the same mixtures at lower temperatures showed a similar trend in the formation of NScs, though more time was needed for the scrolling to start (Figure 2.11).
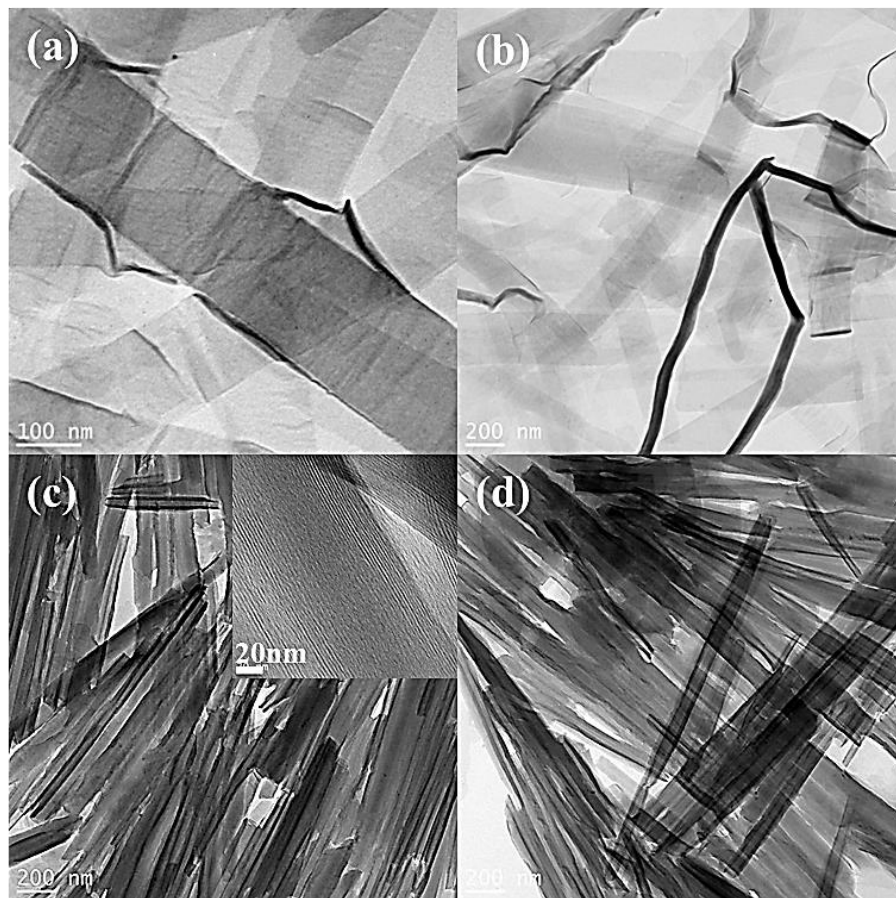
Figure 2.11. TEM images of synthesized samples at different times and temperatures: a) 180 °C, 12 h; (b) 230 °C, 1.5 h; c) 230 °C, 3 h; and d) 230 °C, 6 h. The insets in c) shows high resolution image of NScs. Samples were synthesized using both ethanol and water as solvent and DDA as structure-directing agent.

AFM topography and amplitude as well as TEM images of the sample obtained after 1.5h of ST-treatment at 230°C are seen in Figure 2.12. Circled regions in Figure 2.12a, b and d show the scrolling process proceeding from individual or sets of NSs. Formation of staggered layered structures could also be observed (Figure 2.12c). For the lower temperatures, the formation of NScs from layered structures with an increase in ST reaction times; for example, vanadate NScs were obtained after ST treatment at 250 °C in 2h (Figure 2.1e and f) or 230°C in 3h (Figure 2.11).
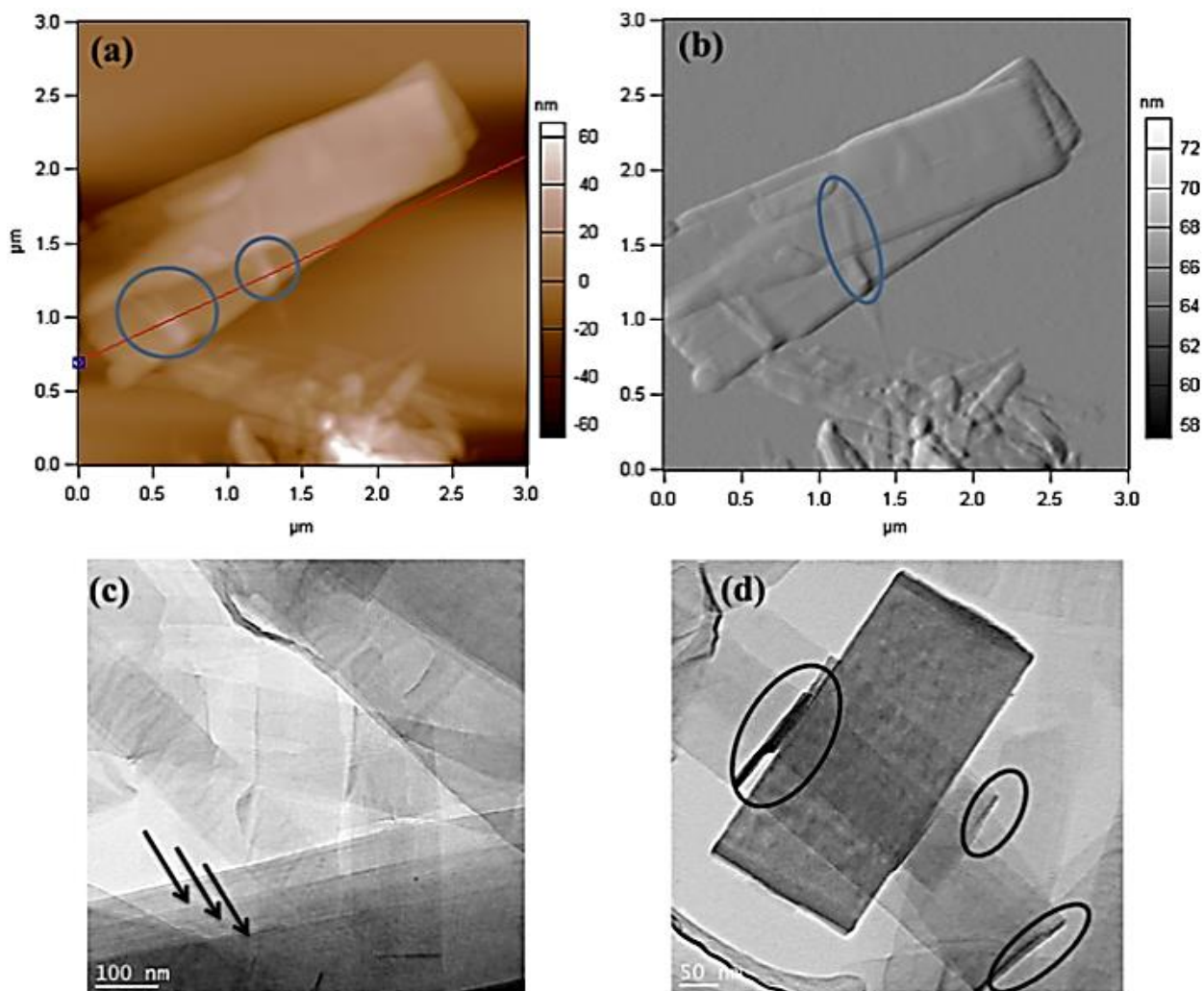
Figure 2.12. a) AFM Topography, b) amplitude images showing the scrolling process c, and d) TEM images; arrows indicate the formation of exfoliated layers, while circled areas show the scrolling process from the edge of lamellar structure. The sample was obtained after 1.5h ST treatment at 230 °C.

In order to investigate variations in vanadium valence states as they relate to the formation mechanism of NScs, X-ray photoelectron spectroscopic (XPS) data were examined. The survey spectrum (Figure 2.13) showed no elements other than C, N, V, and O; the C and N peaks arise from surfactant molecules while the V and O are due to the vanadium oxide scrolls themselves.
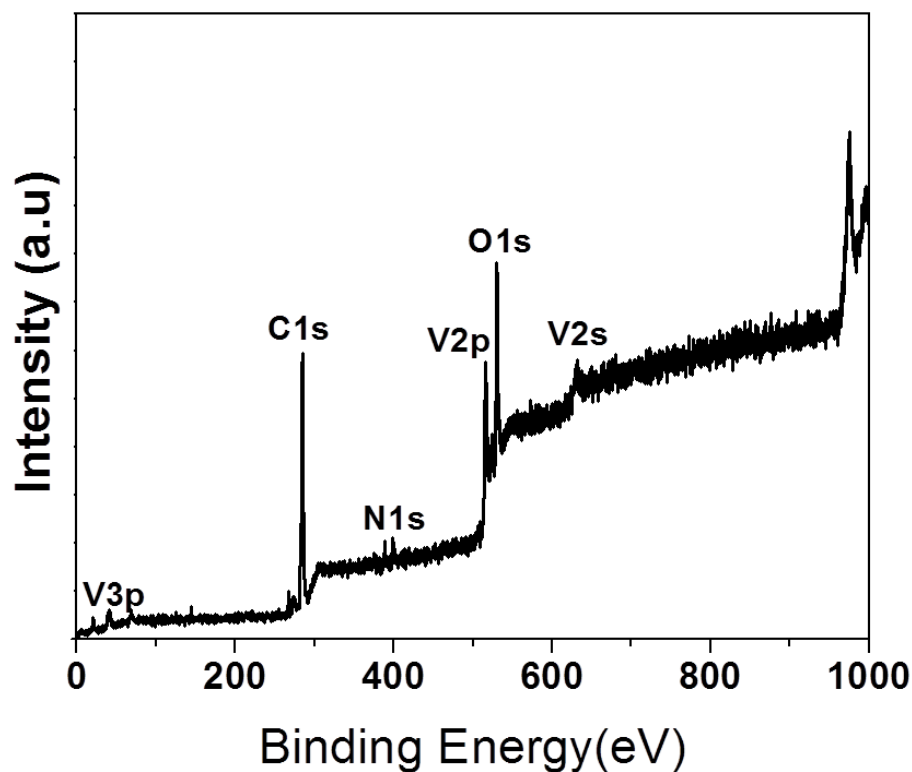
Figure 2.13. A general survey spectrum of vanadate NScs. C and N peaks show the existence of surfactant molecules located between the layers. Excitation source is Al Kα radiation.

Detailed studies were carried out to examine the variation in vanadium valence as a function of reaction time. Figure 2.14 shows the V $2p_{3/2}$, V $2p_{1/2}$ and O1s XPS spectra of the V_2O_5 starting material relative to samples collected at different reaction times. The V 2p has a typical two-peak structure originating from the spin-orbit splitting of V $2p_{3/2}$ at 514-519 eV and V $2p_{1/2}$ at 521-526 eV.[15] The relative abundance of V^{4+} and V^{5+} is calculated from the deconvoluted peak areas. Figure 2.15 shows a plot of the variation in percent V^{4+} as a function of time for reactions carried out at 250 °C. Initially vanadium is fully oxidized (V^{5+}) and on reaction, is rapidly reduced to mostly V^{4+} within the first 15 minutes of the ST treatment. After 30 minutes of ST treatment, greater than 90% of vanadium is in the V^{4+} oxidation state. As shown earlier (Figure 2.10b), NScs are not yet formed. Interestingly, after 1h of ST treatment, the fraction of V^{4+} decreased and in the black product obtained after 2h of ST treatment, 76% of V^{4+} and 24% of V^{5+} are present (Figure 2.15).
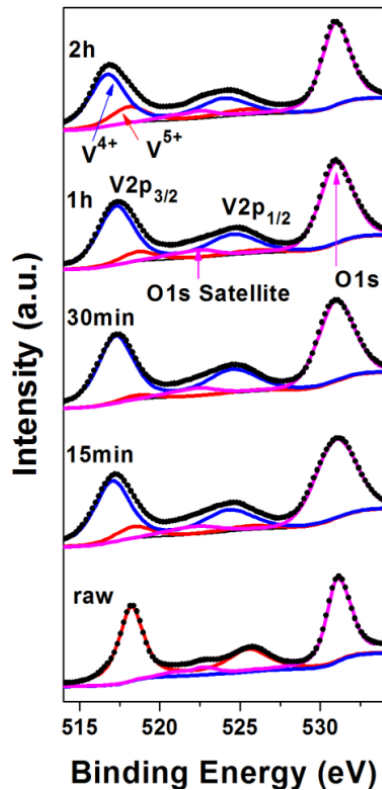
Figure 2.14. V 2p, and O1s XPS spectra for the V_2O_5 raw sample and solvothermally-treated samples at 250 °C for different ST-duration as 0.25, 0.5, 1, and 2h. For better comparison the binding energy of ST 0.25 h spectrum is fixed while other spectra are shifted so that all of them have their O1s peaks aligned. V^{5+} and V^{4+} are marked in the figure. (Mg Kα excitation source is used.)
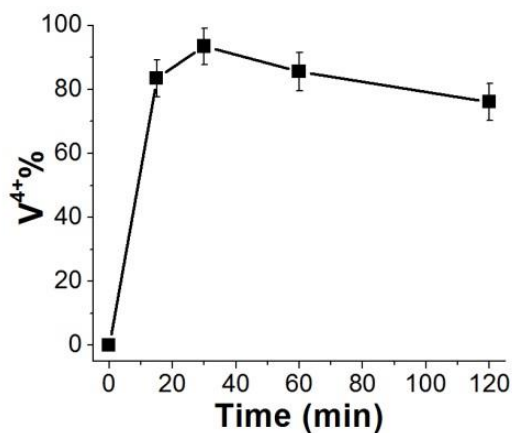
Figure 2.15. Calculated $\%V^{4+}$ with respect to the ST duration obtained using the fitted and deconvoluted XPS data shown in Figure 2.14.

43

2.4 Discussion

The development of the various applications of vanadate NScs would benefit from fast, low-cost production methods as well as size and morphological control. In this chapter, the rapid preparation of bulk quantities of vanadate NScs in distinct size ranges have been presented. Careful attention to experimental details provides an effective synthetic route for the high-yield (> 95%) formation of vanadate NScs using vanadium pentoxide as a cheap, readily available vanadium source. The main key parameters for the fast synthesis of VO_x-NScs were an increase in the molar ratio of surfactant to vanadium precursor and a high ST-temperature. By upwardly adjusting the molar ratio of the structure-directing agent, dodecylamine to vanadium oxide, lamellar structures form immediately after starting materials are combined (Figure 2.9b) and by increasing the temperature to 250°C relative to the previously reported 180°C,[5b] formation times of vanadate NScs were reduced from several days to two hours. Production of up to 20 g of product per synthesis was also possible in the same time period of ST-treatment. Further, the commonly used stirring and aging steps could be eliminated while still resulting in the same quality products; this is likely due to the use of high pressure and temperature which readily produces a homogeneous mixture within the reaction vessel. We expect that larger-scale production[10b] in higher volume commercially-available Teflon-lined autoclaves (e.g. 750 mL) should make it possible to rapidly obtain hundreds of grams of product in a single synthesis.

The ability to control the size range and morphology of NScs directly relates to variations in the molar ratio of structure directing agent to vanadium precursor as well as solvent composition. Though more detailed studies on the formation of NScs with different lengths is needed, differences in oxidation/reduction potentials of related synthesis media likely plays an important role.

Our group has recently shown that noble metal/metal oxide NPs could be encapsulated/inserted inside the vanadate NScs leading to the formation of vanadate based nanopeapods (NPPs).[16-17] Different approaches for making vanadate NPPs with different lengths and encapsulated NPs are being sought. It has been shown that amine groups located between the layers can be exchanged with various cations.[11b] These unique controls over the morphology, composition, and the structure of vanadate NScs could further optimize and improve their possible applications as catalysts and cathode materials for lithium ion batteries.

Structural evolution and formation of vanadate NScs with respect to different temperatures and time were tracked and investigated using XRD and TEM. Formations of nanosheets prior to ST treatment and formation of NScs were observed (Figure 2.9b), which is consistent with what has previously been reported for the formation of vanadate NScs.[5b] During the ST treatment, structural rearrangements in terms of both layer spacings as well as nanosheet orientations occurs, as indicated by low and high angle XRD reflections, respectively (Figure 2.9). And finally, after 1h of ST treatment at 250 °C these lamellar sheets start scrolling from the edge of the layered structures (Figure 2.10d, and 2.12). The rolling process upon heating [18] and under electron beam irradiation[19] have previously been observed in the case of graphite sheets. Our results indicate that higher temperature encourages rapid formation of vanadate NScs probably due to an increase in the reduction/oxidation potential of synthesis media, thermal motion of surfactant located between the lamellar structures, as well as mean diffusion lengths/migration rates of O atoms to form an appropriate defect structure from which NScs could start forming.

Our XPS results also indicate that at the beginning of the ST-treatment, fast reduction of V^{5+} to V^{+4} occurs (Figure 2.15), after which the lamellar structure is still preserved (Figure 2.10a, and b). However, oxidation of V^{4+} to V^{5+}, which had occurred after 30 minutes of ST treatment and continued until the complete formation of NScs (2h), likely plays a significant role in the formation of vanadate NScs. Difference in V^{5+} and V^{4+} ionic radiuses may induce strain in the crystal structure which could be decreased on scrolling.[20] Over the past decade, different vanadium precursors with different oxidation states for synthesizing of NScs have been reported.[5b] During the ST treatment, depending on the oxidation state of vanadium source, either a partial reduction of vanadium from V^{5+} to V^{4+} [14, 21] or a partial oxidation from V^{4+} to V^{5+} [20] were considered to be as a possible driving force for the formation of nanotubes from lamellar vanadium oxide structure. For example, using a comparable synthesis media but vanadyl (IV) acetate, Vera-Robles et al.[20] showed the formation of vanadate NScs due to the oxidation of V^{+4} to V^{+5}. Our XPS analysis, however, shows that oxidation of V^{4+} to V^{5+} could also be important for the formation of vanadate NScs even when fully oxidized V_2O_5 is used as a vanadium source.

2.5 References

1. (a) Arico, A. S.; Bruce, P.; Scrosati, B.; Tarascon, J.-M.; Van Schalkwijk, W., Nanostructured Materials for Advanced Energy Conversion and Storage Devices. *Nature materials* **2005,** *4* (5), 366-377; (b) Sathiya, M.; Prakash, A.; Ramesha, K.; Tarascon, J. M.; Shukla, A., V_2O_5-Anchored Carbon Nanotubes for Enhanced Electrochemical Energy Storage. *Journal of the American Chemical Society* **2011,** *133* (40), 16291-16299; (c) Zhan, G.; Zeng, H. C., General Strategy for Preparation of Carbon-Nanotube-Supported Nanocatalysts with Hollow Cavities and Mesoporous Shells. *Chemistry of Materials* **2015,** *27* (3), 726-734.

2. Zhu, G.-m.; Qu, Z.-b.; Zhuang, G.-l.; Xie, Q.; Meng, Q.-q.; Wang, J.-g., CO Oxidation by Lattice Oxygen on V_2O_5 Nanotubes. *The Journal of Physical Chemistry C* **2011,** *115* (30), 14806-14811.

3. (a) Jin, W.; Yan, S.; Chen, W.; Yang, S.; Zhao, C.; Dai, Y., Enhanced Ethanol Sensing Characteristics by Decorating Dispersed Pd Nanoparticles on Vanadium Oxide Nanotubes. *Materials Letters* **2014,** *128*, 362-365; (b) Jin, W.; Dong, B.; Chen, W.; Zhao, C.; Mai, L.; Dai, Y., Synthesis and Gas Sensing Properties of Fe_2O_3 Nanoparticles Activated V_2O_5 Nanotubes. *Sensors and Actuators B: Chemical* **2010,** *145* (1), 211-215.

4. (a) Hagrman, P. J.; Finn, R. C.; Zubieta, J., Molecular Manipulation of Solid State Structure: Influences of Organic Components on Vanadium Oxide Architectures. *Solid State Sciences* **2001,** *3* (7), 745-774; (b) Liu, X.; Täschner, C.; Leonhardt, A.; Rümmeli, M.; Pichler, T.; Gemming, T.; Büchner, B.; Knupfer, M., Structural, Optical, and Electronic Properties of Vanadium Oxide Nanotubes. *Physical Review B* **2005,** *72* (11), 115407.

5. (a) Nordlinder, S.; Nyholm, L.; Gustafsson, T.; Edström, K., Lithium Insertion into Vanadium Oxide Nanotubes: Electrochemical and Structural Aspects. *Chemistry of Materials* **2006,** *18* (2), 495-503; (b) McNulty, D.; Buckley, D. N.; O'Dwyer, C., Synthesis and Electrochemical Properties of Vanadium Oxide Materials and Structures as Li-Ion Battery Positive Electrodes. *Journal of Power Sources* **2014,** *267*, 831-873; (c) Chernova, N. A.; Roppolo, M.; Dillon, A. C.; Whittingham, M. S., Layered Vanadium and Molybdenum Oxides: Batteries and Electrochromics. *Journal of Materials Chemistry* **2009,** *19* (17), 2526-2552; (d) Wang, Y.; Takahashi, K.; Lee, K.; Cao, G., Nanostructured Vanadium Oxide Electrodes for Enhanced Lithium-Ion Intercalation. *Advanced Functional Materials* **2006,** *16* (9), 1133; (e) Wei, Q.; Tan, S.; Liu, X.; Yan, M.; Wang, F.; Li, Q.; An, Q.; Sun, R.; Zhao, K.; Wu, H., Novel Polygonal Vanadium Oxide Nanoscrolls as Stable Cathode for Lithium Storage. *Advanced Functional Materials* **2015,** *25* (12), 1773-1779.

6. (a) Demishev, S.; Chernobrovkin, A.; Glushkov, V.; Grigorieva, A.; Goodilin, E.; Ohta, H.; Okubo, S.; Fujisawa, M.; Sakurai, T.; Sluchanko, N., Magnetic Properties of Vanadium Oxide Nanotubes and Nanolayers. *Physical Review B* **2011,** *84* (9), 094426; (b) Saleta, M.; Lopez, C.; Granada, M.; Troiani, H.; Sanchez, R.; Malta, M.; Torresi, R., Thermal Stability and the Magnetic Properties of Hybrid Vanadium Oxide-Tetradecylamine Nanotubes. *Journal of Applied Physics* **2012,** *112* (5), 053912; (c) Popa, A. I.; Vavilova, E.; Täschner, C.; Kataev, V.; Büchner, B.; Klingeler, R. d., Electrochemical behavior and magnetic properties of vanadium oxide nanotubes. *The Journal of Physical Chemistry C* **2011,** *115* (13), 5265-5270; (d) Krumeich, F.; Muhr, H.-J.; Niederberger, M.; Bieri, F.; Schnyder, B.; Nesper, R., Morphology and Topochemical Reactions of Novel Vanadium Oxide Nanotubes. *Journal of the American Chemical Society* **1999,** *121* (36), 8324-8331; (e) Magon, C.; Lima, J.; Donoso, J.; Lavayen, V.; Benavente, E.; Navas, D.; Gonzalez, G., Deconvolution of the EPR Spectra of Vanadium Oxide Nanotubes. *Journal of Magnetic Resonance* **2012,** *222*, 26-33.

7. Spahr, M. E.; Bitterli, P.; Nesper, R.; Müller, M.; Krumeich, F.; Nissen, H. U., Redox-Active Nanotubes of Vanadium Oxide. *Angewandte Chemie International Edition* **1998,** *37* (9), 1263-1265.

8. Mai, L.; Chen, W.; Xu, Q.; Zhu, Q.; Han, C.; Peng, J., Cost-Saving Synthesis of Vanadium Oxide Nanotubes. *Solid State Communications* **2003,** *126* (10), 541-543.

9. (a) Jaber, M.; Ribot, F. o.; Binet, L.; Briois, V. r.; Cassaignon, S.; Rao, K.; Livage, J.; Steunou, N., Ex Situ X-ray Diffraction, X-ray Absorption Near Edge Structure, Electron Spin Resonance, and

Transmission Electron Microscopy Study of the Hydrothermal Crystallization of Vanadium Oxide Nanotubes: an Insight into the Mechanism of Formation. *The Journal of Physical Chemistry C* **2012,** *116* (47), 25126-25136; (b) Corr, S. A.; Grossman, M.; Furman, J. D.; Melot, B. C.; Cheetham, A. K.; Heier, K. R.; Seshadri, R., Controlled Reduction of Vanadium Oxide Nanoscrolls: Crystal Structure, Morphology, and Electrical Properties. *Chemistry of Materials* **2008,** *20* (20), 6396-6404; (c) Patzke, G. R.; Krumeich, F.; Nesper, R., Oxidic Nanotubes and Nanorods—Anisotropic Modules for a Future Nanotechnology. *Angewandte Chemie International Edition* **2002,** *41* (14), 2446-2461.

10. (a) Bieri, F.; Krumeich, F.; Muhr, H. J.; Nesper, R., The First Vanadium Oxide Nanotubes Containing an Aromatic Amine as Template. *Helvetica Chimica Acta* **2001,** *84* (10), 3015-3022; (b) Niederberger, M.; Muhr, H.-J.; Krumeich, F.; Bieri, F.; Günther, D.; Nesper, R., Low-Cost Synthesis of Vanadium Oxide Nanotubes via Two Novel Non-Alkoxide Routes. *Chemistry of Materials* **2000,** *12* (7), 1995-2000; (c) Muhr, H. J.; Krumeich, F.; Schönholzer, U. P.; Bieri, F.; Niederberger, M.; Gauckler, L. J.; Nesper, R., Vanadium Oxide Nanotubes—a New Flexible Vanadate Nanophase. *Advanced Materials* **2000,** *12* (3), 231-234.

11. (a) Dobley, A.; Ngala, K.; Yang, S.; Zavalij, P. Y.; Whittingham, M. S., Manganese Vanadium Oxide Nanotubes: Synthesis, Characterization, and Electrochemistry. *Chemistry of Materials* **2001,** *13* (11), 4382-4386; (b) Reinoso, J. M.; Muhr, H. J.; Krumeich, F.; Bieri, F.; Nesper, R., Controlled Uptake and Release of Metal Cations by Vanadium Oxide Nanotubes. *Helvetica Chimica Acta* **2000,** *83* (8), 1724-1733.

12. Souza Filho, A.; Ferreira, O.; Santos, E.; Mendes Filho, J.; Alves, O., Raman Spectra in Vanadate Nanotubes Revisited. *Nano Letters* **2004,** *4* (11), 2099-2104.

13. Chen, X.; Sun, X.; Li, Y., Self-Assembling Vanadium Oxide Nanotubes by Organic Molecular Templates. *Inorganic Chemistry* **2002,** *41* (17), 4524-4530.

14. Sun, D.; Kwon, C. W.; Baure, G.; Richman, E.; MacLean, J.; Dunn, B.; Tolbert, S. H., The Relationship Between Nanoscale Structure and Electrochemical Properties of Vanadium Oxide Nanorolls. *Advanced Functional Materials* **2004,** *14* (12), 1197-1204.

15. Rostamzadeh, T.; Adireddy, S.; Wiley, J. B., Formation of Scrolled Silver Vanadate Nanopeapods by Both Capture and Insertion Strategies. *Chemistry of Materials* **2015**.

16. Nordlinder, S.; Augustsson, A.; Schmitt, T.; Guo, J.; Duda, L. C.; Nordgren, J.; Gustafsson, T.; Edström, K., Redox Behavior of Vanadium Oxide Nanotubes as Studied by X-ray Photoelectron Spectroscopy and Soft X-ray Absorption Spectroscopy. *Chemistry of Materials* **2003,** *15* (16), 3227-3232.

17. (a) Adireddy, S.; Carbo, C. E.; Rostamzadeh, T.; Vargas, J. M.; Spinu, L.; Wiley, J. B., Peapod-Type Nanocomposites through the In Situ Growth of Gold Nanoparticles within Preformed Hexaniobate Nanoscrolls. *Angewandte Chemie International Edition* **2014,** *53* (18), 4614-4617; (b) Adireddy, S.; Rostamzadeh, T.; Carbo, C. E.; Wiley, J. B., Particle Placement and Sheet Topological Control in the Fabrication of Ag–Hexaniobate Nanocomposites. *Langmuir* **2014,** *31* (1), 480-485; (c) Yao, Y.; Chaubey, G. S.; Wiley, J. B., Fabrication of Nanopeapods: Scrolling of Niobate Nanosheets for Magnetic Nanoparticle Chain Encapsulation. *Journal of the American Chemical Society* **2011,** *134* (5), 2450-2452.

18. Heidenreich, R. D.; Hess, W.; Ban, L., A Test Object and Criteria for High Resolution Electron Microscopy. *Journal of Applied Crystallography* **1968,** *1* (1), 1-19.

19. Ugarte, D., Curling and Closure of Graphitic Networks nder Electron-Beam Irradiation. *Nature* **1992,** *359* (6397), 707-709.

20. Vera-Robles, L. I.; Campero, A., A Novel Approach to Vanadium Oxide Nanotubes by Oxidation of V^{4+} Species. *The Journal of Physical Chemistry C* **2008,** *112* (50), 19930-19933.

21. Worle, M.; Krumeich, F.; Bieri, F.; Muhr, H.-J.; Nesper, R., Flexible V_7O_{16} Layers as the Common Structural Element of Vanadium Oxide Nanotubes and a New Crystalline Vanadate. *Zeitschrift fur Anorganische und Allgemeine Chemie* **2002,** *628* (12), 2778-2784.

Chapter 3 Formation of Scrolled Silver Vanadate Nanopeapods by both Capture and Insertion Strategies[†]

3.1 Introduction

Two- and three-dimensional nanoparticle (NP) assemblies have been the focus of much recent research.[1,2] Among these studies there are relatively few reports on the self-organization of NPs into one-dimensional structures due to the inherent difficulty in synthesis and subsequent characterization.[3] Such 1-D nanostructures are of fundamental interest for a variety of reasons such as dipolar magnetic coupling, surface plasmonic interactions, sensor applications, and catalysis.[3-9] The interaction of light, for example, with self-assembled noble metal NPs may produce strong electric fields in the gaps between them leading to potential applications of these constructs as nanodevices and nanosensors based on surface enhanced Raman spectroscopy (SERS).[10-13]

One promising nanoarchitecture in which to explore NP-NP interactions are nanopeapods (NPPs). These assemblies consist of ordered arrays of NPs encapsulated within the hollow space of nanotubes (NT) or nanoscrolls (NScs). Advanced nanoarchitectures featuring controlled syntheses and well-designed encapsulation of different NPs into various types of nanosheets (NSs) promise to show novel properties arising from both the intrinsic behavior of the individual NPs as well as the NP-NP and NP-NScs interactions.[14-16] A simple and versatile synthetic method for forming Fe_3O_4@hexaniobate NPPs by the capture of preformed magnetic NPs in scrolled nanosheets has previously been developed by our group.[17] Bi-functional Au-Fe_3O_4@hexaniobate NPPs were also synthesized using in-situ growth of gold inside partially-filled Fe_3O_4@hexaniobate NPPs.[18] Optical measurements of the bi-functional NPPs showed a progressive red shift in plasmonic behavior between Au NPs and Au-Fe_3O_4 NPPs. This approach could be further optimized to include the encapsulation of different types of NPs inside hexaniobate NScs.

NTs and NScs constructed of transition metal oxides with variable oxidation states, in particular vanadium oxide, hold enormous promise for applications such as lithium ion batteries, catalysis, and electrochemical devices.[19,20] Vanadium oxide NScs with multi-walled tubular structures can be synthesized through a solvothermal treatment of lamellar vanadium oxide in the presence of structure-directing agents.[21,22] The formation of hybrids based on the attachment of NPs either on the outer or inner surfaces of vanadium oxide NScs may improve their properties as well as their electrochemical performance. There are a few published reports on the functionalization of vanadium pentoxide NScs with noble metal/metal oxide NPs. Zhang et al. have reported the synthesis of Pd NPs on the surface of vanadium oxide NTs with subsequent improvement of the electrochemical performance for methanol oxidation.[23] Jin et al. have also shown that the attachment of 15 nm Fe_2O_3 NPs to the surface of vanadium oxide NScs could considerably improve ethanol sensing properties in terms of both sensor response and selectivity.[24] To the best of our knowledge, however, formation of high-quality vanadium oxide NPPs, in which noble metal NPs are encapsulated inside the NScs, has not been reported. Herein we report two distinct methods for the rapid synthesis of vanadate NPPs. These strategies are quite effective and offer high productivity, simplicity, and versatility as demonstrated in the production of Ag@vanadate NPPs.

3.2 Experimental Section

Materials. Hexane (anhydrous, 95%), benzyl ether (99%), toluene (99.8%, anhydrous) oleylamine (>70%, OAm), dodecylamine (98%), vanadium (V) oxide (≥ 99.6%), silver nitrate (99%), and iron (III) oxide (hydrated; catalyst grade, 30−50 mesh) were purchased from Sigma-Aldrich. Pure grade ethanol (Pharmco-Aaper, 200 Proof, absolute) was used in all preparations.

Synthesis of silver NPs. A modified procedure reported by Wang et al.[25] was used to prepare Ag NPs. $AgNO_3$ (1 mmol) and 10 mL of OAm were mixed under Ar flow in a three-neck flask. The mixture was dehydrated by heating it to 110 °C for 30 minutes. It was then further heated to 180 °C at the rate of 10 °C/min and held at this temperature for 30 minutes before cooling to room temperature. The Ag NPs were separated by centrifugation after the addition of more ethanol. The resulting monodispersed Ag NPs (Figure 1a) are highly soluble in nonpolar solvents.

Synthesis of Fe₃O₄ NPs. Magnetite NPs ~ 9 nm in diameter were synthesized using a modified procedure from Xu *et al.*[26] Iron oxide (1 mmol), benzyl ether (4 mL) and OAm (6 mL) were mixed and stirred in a three-neck flask under Ar flow. The mixture was heated at 110 °C for 1 h and after that the temperature was raised to 300 °C at the rate of 10 °C/min. The mixture was then kept at 300 °C for 1h and slowly cooled to room temperature. The product was washed with acetone and separated from the solution by centrifugation.

Synthesis of vanadate nanoscrolls. Vanadate NScs were synthesized using a modified procedure reported by Corr et al.[27] Vanadium (V) oxide (1 mmol, 0.18 g) was dispersed in 1.5 mL of deionized water and added to a solution containing 1 mmol (0.18 g) dodecylamine in 1.5 mL of ethanol. After the mixture was magnetically stirred at room temperature for 8 h, 1 mL toluene and 3 mL of deionized water were added. The final mixture was transferred into a 23 mL Teflon-lined stainless-steel autoclave and solvothermally treated at 230 °C for 6 h after which it was gradually cooled to room temperature (1 °C/min). The obtained black product was washed first with ethanol and then hexane in order to remove the unreacted amine. Vanadate nanoscrolls were finally separated from hexane by centrifugation. This method can be scaled up to make bulk quantities of nanoscrolls.[28]

Solvothermal synthesis of Ag@vanadate NPPs. The procedure is similar to the synthesis of vanadate nanoscrolls. A mixture consisting of V_2O_5 (1 mmol, 0.18 g) in 1.5mL of deionized water was combined with 1 mmol (0.18 g) dodecylamine in 1.5mL of ethanol. Ag NPs (0.1 g) were first dispersed in toluene before addition to the V_2O_5 mixture. The combination of Ag NPs and vanadate solution was stirred for 8 h. As with the synthesis of vanadate nanoscrolls, the combination was placed in a sealed autoclave, heated to 230 °C for 6 h, and then cooled gradually to room temperature (1 °C/min). The resulting precipitate was washed first with ethanol and then hexane, and finally isolated by centrifugation. In order to remove free Ag NPs from the peapods, the black product was redispersed in 20 mL toluene and further centrifuged (1000 rpm, 1min). This final step was repeated twice.

Solvent evaporation approach for making Ag@vanadate NPPs. Ag NPs were inserted into preformed V_2O_5 nanoscrolls (scrolls prepared by the methods described above) to form Ag@vanadate NPPs. Ag NPs (0.05 g) and 0.04 g of vanadate NScs were dispersed in 1.5 mL of toluene and magnetically stirred for 1 min. Toluene evaporation was done at room temperature

over ~24 h under a fume hood. Vanadate nanopeapods were lastly separated from the free particles by adding extra toluene, followed by redispersion and a final centrifugation.

Solvent evaporation approach for making Fe₃O₄@vanadate NPPs. Similar experimental conditions for making $Ag@V_2O_5$ NPPs were used to insert Fe_3O_4 NPs into preformed vanadate NScs.

Characterization. For transmission electron microscopy (TEM) measurements, samples were dispersed in toluene and then drop cast onto a 200 mesh carbon-coated copper grid. Samples were then characterized with a TEM JEOL 2010 operated at an accelerating voltage of 200 kV. The unit is equipped with EDAX genesis energy dispersive spectroscopy (EDS) system. The same sample drop cast method was used in scanning electron microscopy (SEM) observation. SEM was carried out on a Carl Zeiss 1530 VP field-emission scanning electron microscope (FESEM). A Philips X-Pert PW 3040 MPD equipped with a curved graphite monochromator operating at 40 kV accelerating voltage and 40 mA current, was used to collect X-ray powder diffraction (XRD) data. Absorption spectra were recorded in reflectance mode on a Cary 500 UV-Vis spectrophotometer.

3.3 Results and discussion

Ag@vanadate NPPs were prepared by two distinct routes which are schematically shown if Figure 3.1. In the first, the NPPs were formed via a 6 h solvothermal treatment at 230 °C using a combination of preformed oleylamine-capped ~12 nm Ag NPs (Figure 3.2a), an aqueous-ethanol mixture of vanadium (V) oxide, and dodecylamine surfactant. This approach resulted in high quality NPPs with high loadings (Figure 3.2b and c). NPPs typically exhibited one-dimensional NP chains with interparticle distances of about 1-3 nm; single- or double-chains with larger inter-particle distances can also be seen from SEM and TEM images (Figure 3.3 and 3.4). Interestingly, unlike with Ag@hexaniobate NPPs with a clear 2-3 nm separation of NPs from the scrolled nanosheet,[29] the Ag NPs in Ag@vanadate NPPs appear to be in immediate contact with the NScs and in some instances, the scroll can be seen to undulate along the NP-chain topology (Figure 3.2c), similar to what is seen for single walled Co@hexaniobate NPPs.[30]
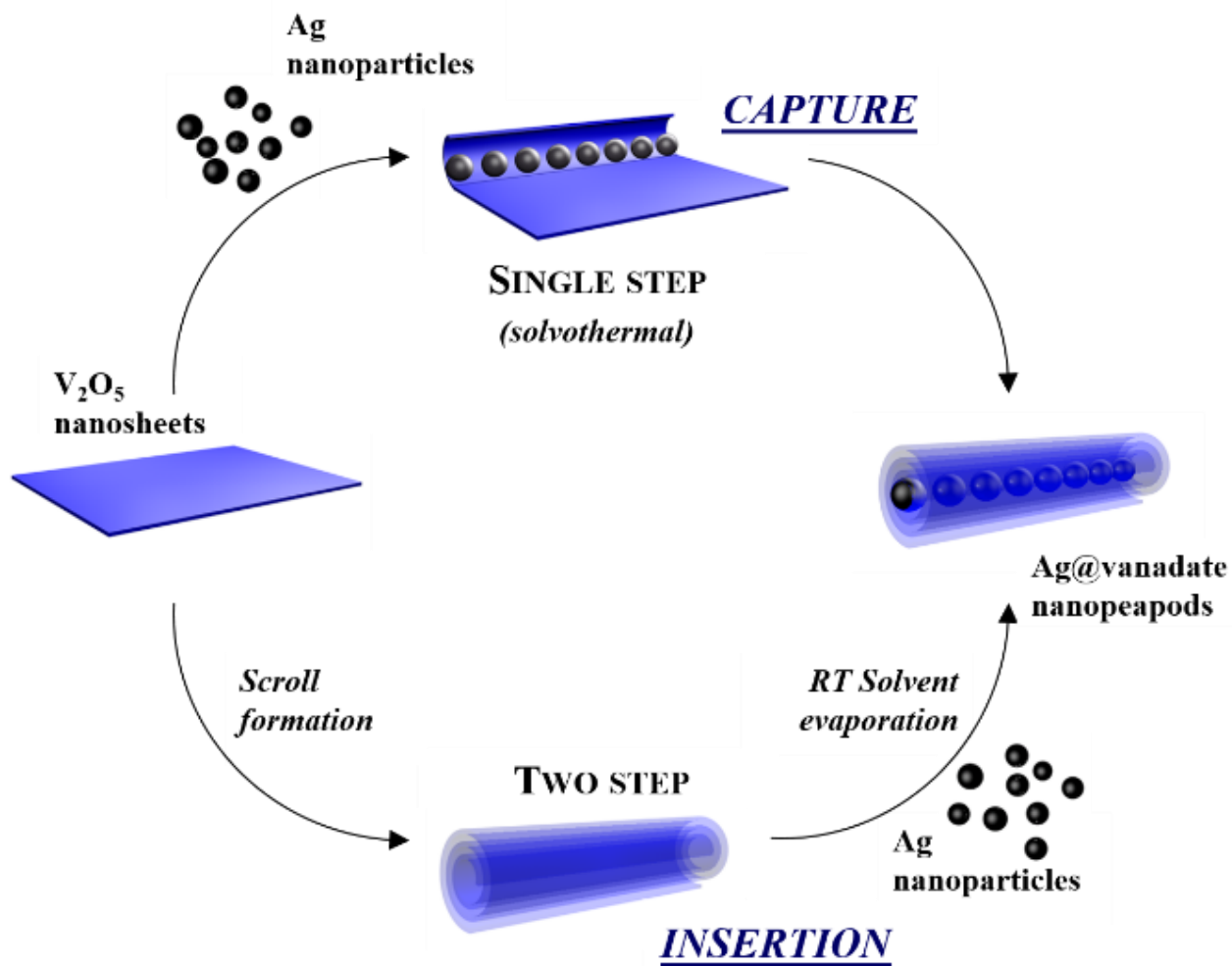
Figure 3.1. Schematic showing the formation of Ag@vanadate nanopeapods using two distinct approaches.

An estimate of the filling fraction of NPs to the empty space was obtained for 250 different NPPs from low magnification TEM images; the corresponding pie chart is shown in Figure 3.2d. We observed that almost 2/5 of the NPPs are at least 80% filled and that nearly 2/3 have a filling fraction of more than 60%. Note that some uncaptured free NPs can also be seen from the TEM images, though these numbers can be minimized using additional centrifugation steps.
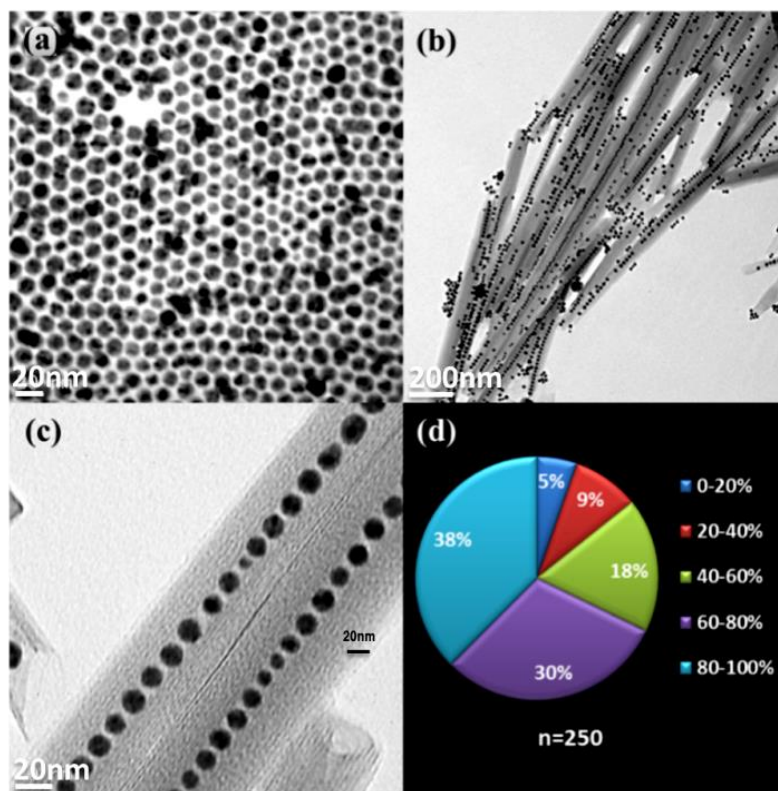
Figure 3.2. TEM images of Ag NPs, b, c) TEM images of solvothermally-made Ag@vanadate NPPs, and d) pie chart representing the NPs filling fraction obtained by considering 250 NPPs.
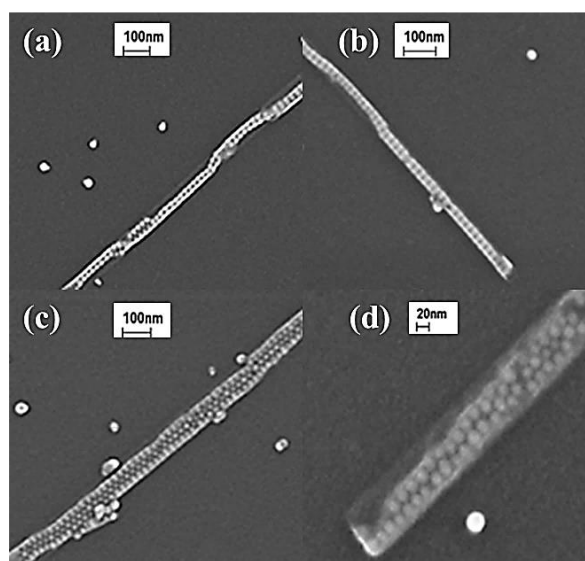
Figure 3.3. FESEM images of ST-synthesized NPPs showing different arrangement of NPs chain encapsulated inside vanadate NSs.
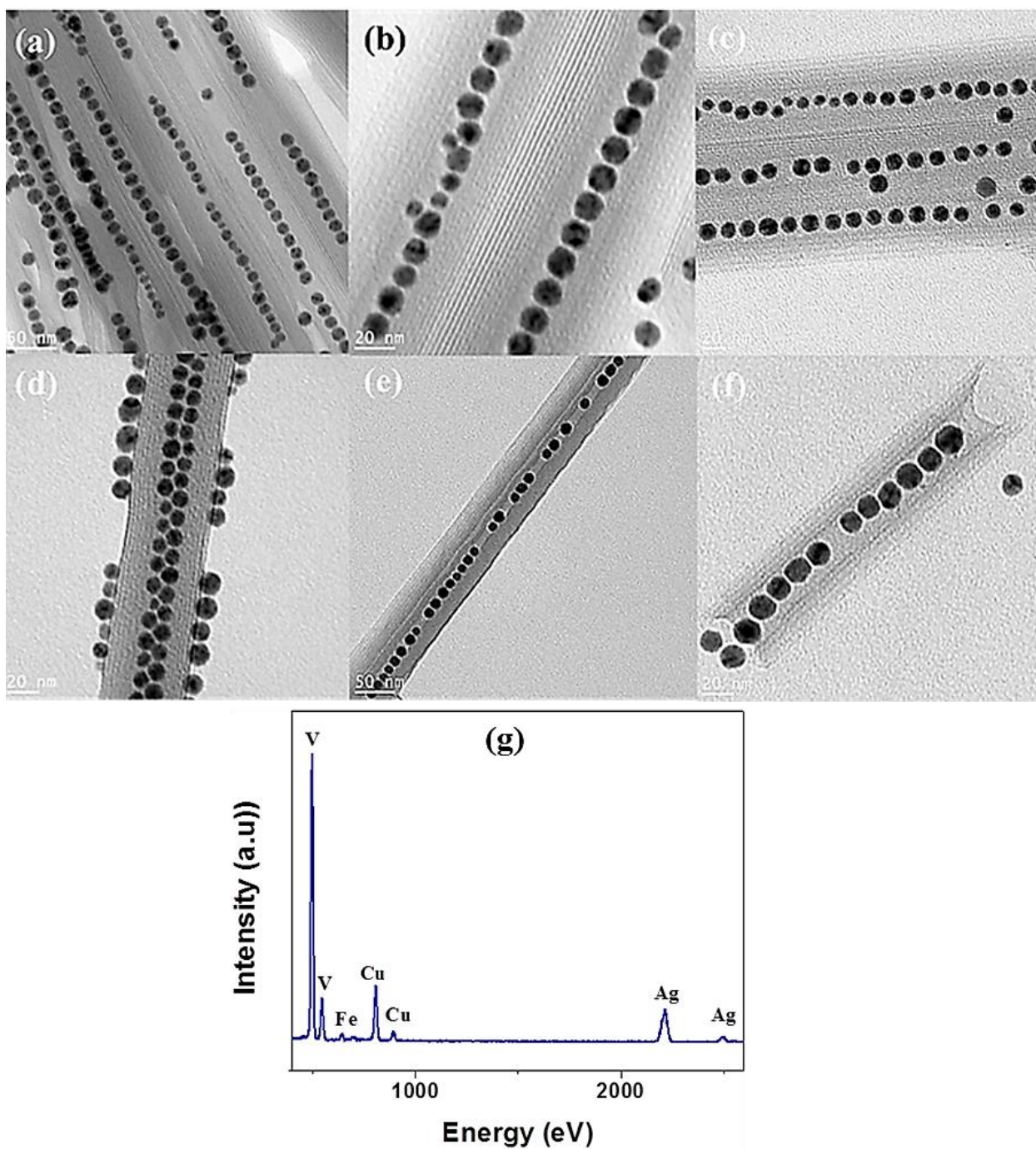
Figure 3.4. (a-c) Additional TEM images of solvothermally-synthesized Ag@vanadate. (d) NPPs decorated with Ag NPs. (e) NPPs with different inter-particle spacings. (f) Short length NPPs. (g) EDS analysis of NPPs. Fe and Cu came from sample holder and TEM grid, respectively.

The second synthetic method for the fabrication of Ag@vanadate NPPs is a new room temperature approach involving the insertion of NPs into preformed NScs. Vanadate NScs were first synthesized using the same experimental conditions as solvothermally-synthesized NPPs, except that no Ag NPs were added. Preformed vanadate NScs (Figures 3.5a and b) were then combined with Ag NPs in toluene and the solvent was allowed to slowly evaporate to dryness over ~24 hrs. Removal of the solvent draws some of the NPs to the interior of the NScs by capillary forces to create the peapod structures. Figures 3.5c and d show TEM images of the Ag@vanadate NPPs obtained using this approach.
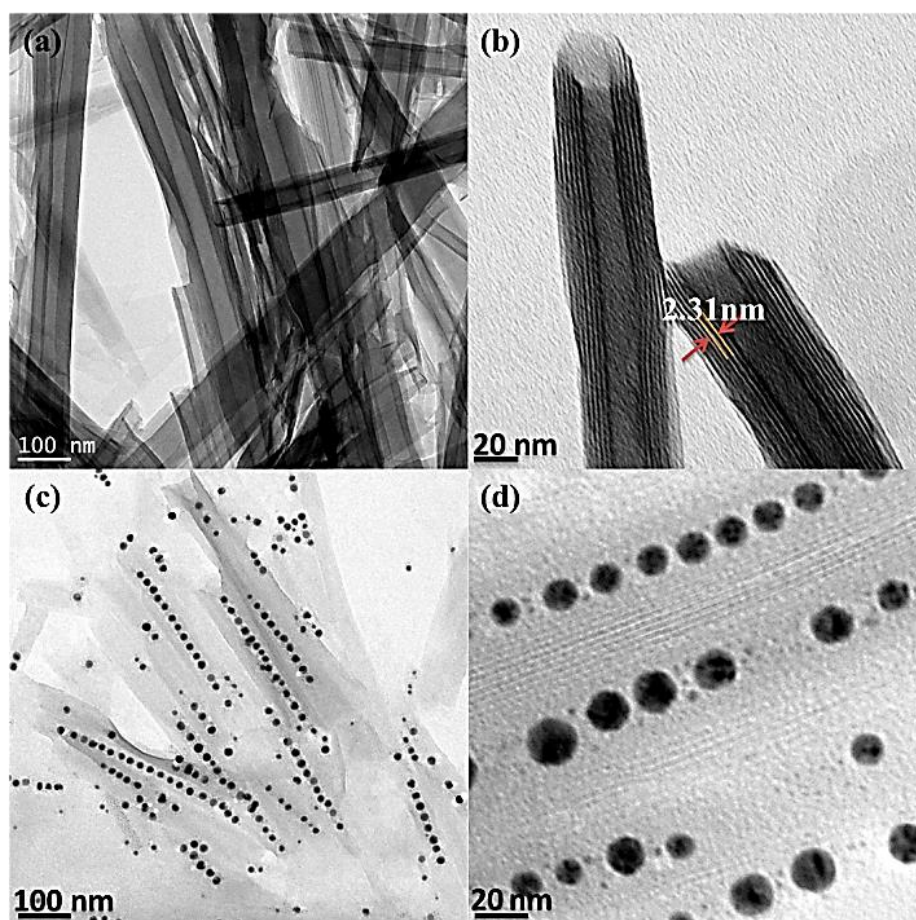
Figure 3.5. a) Low magnification TEM image of empty vanadate NScs, b) high resolution TEM images of vanadate NScs, c, d) low and high magnification TEM images of Ag@vanadate NPPs synthesized using Ag NPs and preformed NScs through a solvent evaporation approach.

The filling fraction of the peapods formed using the solvent evaporation approach is approximately half that obtained using the solvothermal approach and on average the NP-NP separation is greater. This insertion strategy is not limited to Ag NPs and has also been applied to the preparation of Fe_3O_4@vanadate NPPs, though the extent of NP uptake and quality of the resulting NPPs is not as good as seen with Ag NPs. Cong et al.[11] have recently reported the formation of gold@silica NPPs by first forming silica NTs in an AAO template and then using a similar solvent evaporation approach for the insertion of NPs. As a control experiment, Ag NPs and vanadate NScs were combined under the same conditions but without evaporation of the solvent. As shown in Figure 3.6, this approach shows no NP uptake implying that complete solvent evaporation is essential for the formation of NPPs.

As compared to the vanadate NScs, the inner diameter of the solvothermally-synthesized Ag@vanadate NPPs has a narrower size distribution (Figure 3.7). This is similar to what was previously reported in the case of hexaniobate NPPs where the inner diameter of the NPPs was dictated by the size of the encapsulated NPs.[17]
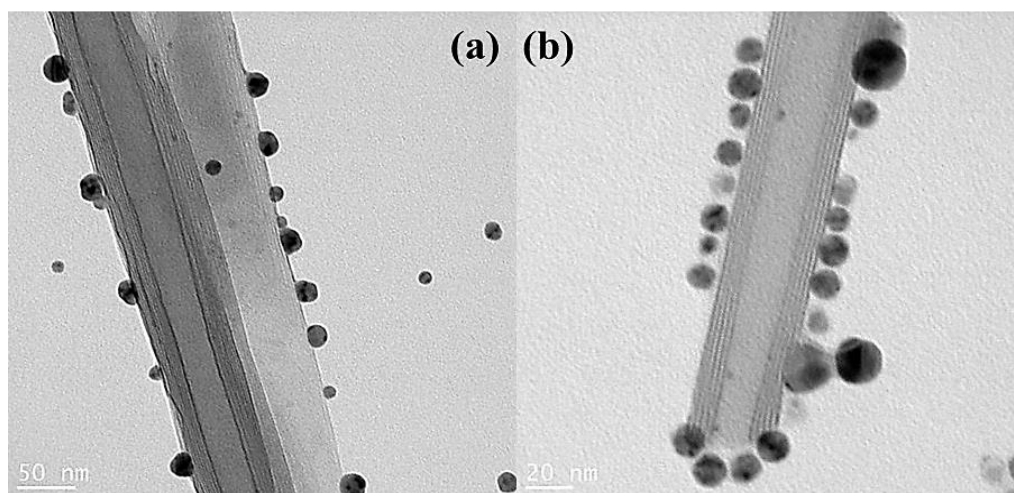
Figure 3.6. TEM images showing the structure obtained after simple mixing of preformed V_2O_5 and Ag NPs in toluene – no solvent evaporation. In this experiment 10mg of Ag NPs and 10mg preformed V_2O_5 were dispersed in 1mL of toluene inside a vial and after simple mechanical shaking, components were separated by centrifugation and redispersed in toluene. TEM grid was heated at 200°C for 2 minutes after drop casting.

Unlike the solvothermally-prepared NPPs, peapods made by the insertion technique show a range of inner diameter values as seen in the preformed NScs. These results are consistent with a mechanism where in the formation of the solvothermally-prepared NPPs, the NPs are first attached to the surface of the nanosheets, captured during the scrolling process to form the NPPs, and finally, separated from the larger nanosheets during a detachment process.
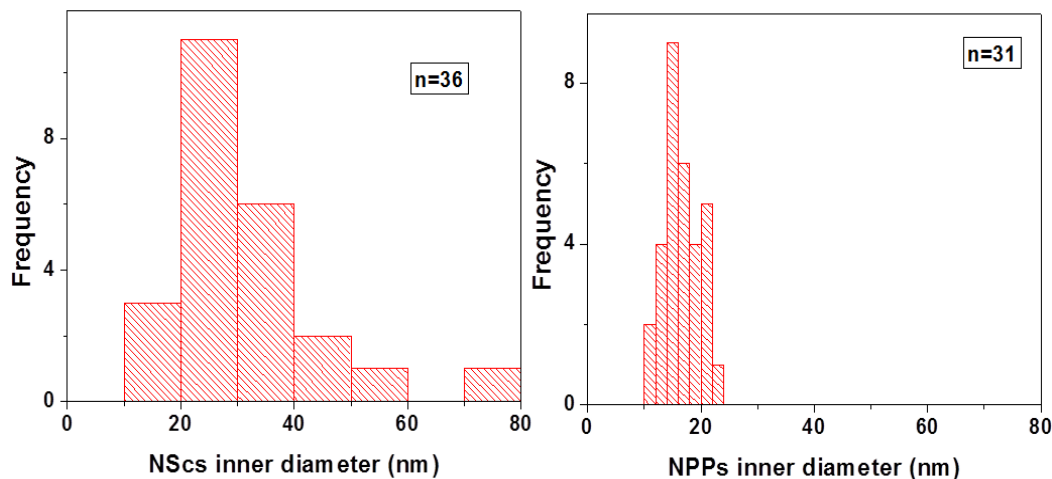
Figure 3.7. Histograms showing inner diameter size distribution of (a) NScs; values obtained from inner diameters of 36 NScs using low magnification TEM images. (b) Solvothermally-synthesized NPPs; values obtained by measuring the inner diameter of 31 NPPs using low magnification TEM images.

Figure 3.8 shows scrolled NPPs prior to detachment from the large vanadate nanosheets, consistent with this mechanism. This is similar to what was previously proposed in the formation of hexaniobate NPPs.[17] Chen et al. investigated the formation mechanism of vanadate NScs and also observed the formation of nanosheets prior to scrolling.[31] Solvothermal treatment of preformed NScs and Ag NPs, even with different solvents, did not lead to the formation of NPPs (Figure 3.9), further supporting the suggested NPP formation mechanism for encapsulation of the NPs during the scrolling process. Additionally, these experiments suggest that formed NScs could be opened up and large nanosheets formed after the solvothermal treatment of the preformed nanoscrolls in the presence of both water (5mL) and toluene (1mL) as solvent (Figure 3.9c).
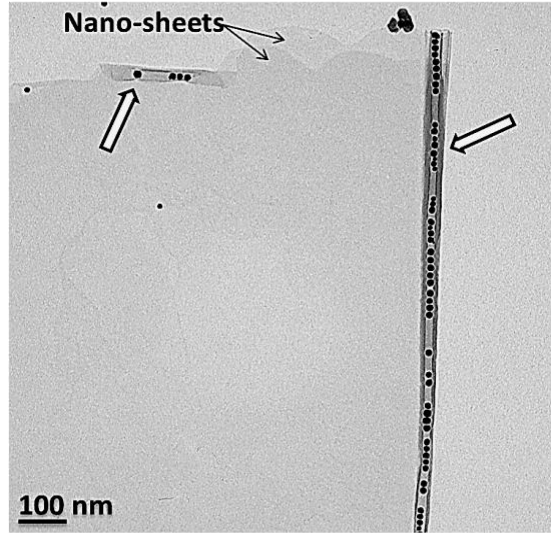
Figure 3.8. TEM image showing scrolling process after attachment of NPs. Formed NPPs are still attached to the nanosheets. The next step would be detachment of NPPs from the nanosheets.
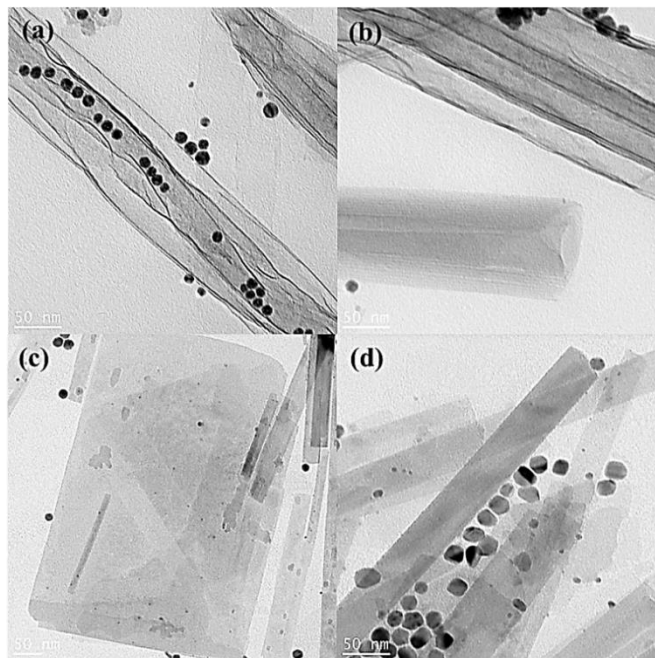
Figure 3.9. Solvothermal reactions using preformed nanoscrolls; a, b) TEM images showing the structure obtained after solvothermal treatment of preformed V_2O_5 NScs and Ag NPs dispersed in 6 mL of toluene. c, d) mixture of 1 mL of toluene and 5 mL of water. Solvothermal treatment was done at 220 °C for 2 h which did not lead to the formation of peapods. These experiments suggest that NPs encapsulation likely happens during the scrolling process.

The X-ray diffraction patterns of vanadate NScs, solvothermally-synthesized Ag@vanadate NPPs, and the Ag metal reference pattern are shown in Figure 3.10. The low intensity high-angle peaks (*hk0*) are related to the two-dimensional structure of the layers and are independent of the surfactant used. These peaks can be indexed according to a square lattice with a = 6.1 Å.[20,32] The low-angle reflection peaks (*00l*) of the NScs and solvothermally-synthesized NPPs are related to the well-ordered layered structure of NScs and the highest-intensity peak reveals the distance between the vanadium oxide layers within the scroll structure.[33] This interlayer distance can be varied with a change in the length of the surfactant hydrocarbon chain.[20,32] The interlayer spacing for the NScs and solvothermally-synthesized NPPs is calculated using the low-angle reflection peaks (*00l*) which corresponds to d-spacing values of about 27.2(3) and 27.01(2) Å, respectively.
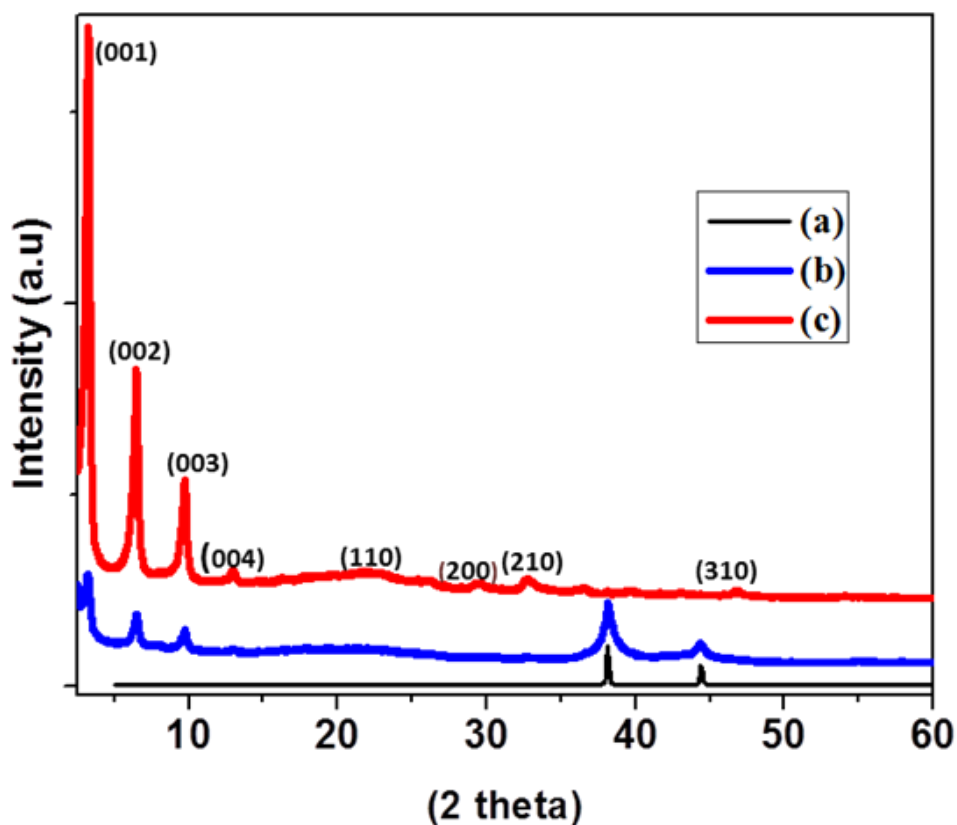
Figure 3.10. Powder XRD pattern of a) reference pattern of Ag NPs, b) solvothermally synthesized Ag@vanadate NPPs, and c) solvothermally-synthesized vanadate NScs.

Using the TEM image of the NScs shown in Figure 3.5b, the interlayer spacing was found to be roughly 23.1 Å. Further TEM analysis showed that different NScs can, however, have different interlayer spacings ranging from 10 to approximately 40 Å. The intercalation of water molecules may possibly be responsible for the larger interlayer spacings than what is expected for the length of dodecylamine.[34]

In order to investigate the effect of NP interactions on the optical properties of NPPs, UV-Vis absorption spectra of Ag NPs and the Ag@vanadate NPPs were collected. The surface plasmon resonance (SPR) peak of the Ag NPs is shape, size, and environment dependent. In a chain of assembled NPs, plasmon coupling also depends on the interactions between adjacent NPs[35-38] where it is known that the plasmon resonance peak can shift to higher wavelengths relative to those of single NPs.[36, 38] This is due to interparticle coupling effects which lead to energy shifts and energy confinement between NPs. [35-38] In Figure 3.11, UV−Vis absorption spectra of a) free Ag NPs, b) Ag@vanadate NPPs obtained through solvent evaporation, and c) solvothermally-prepared Ag@vanadate NPPs are shown.
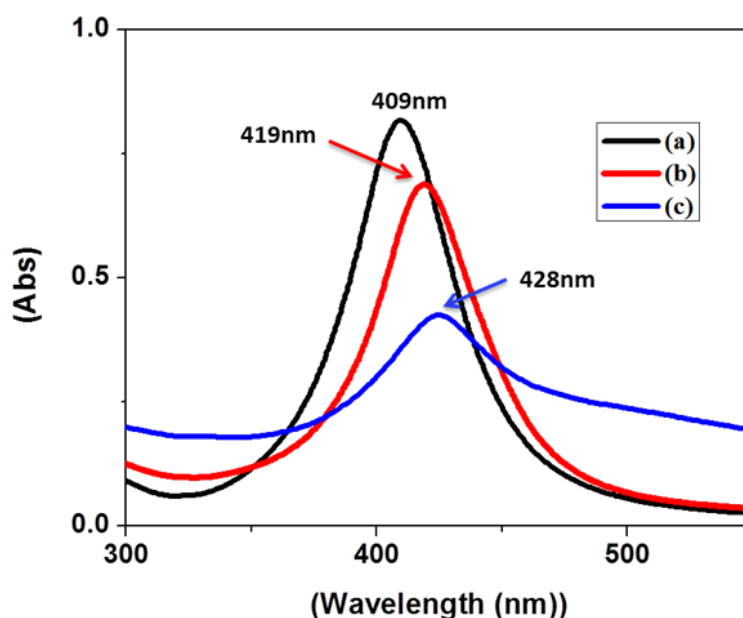
Figure 3.11. UV−Vis absorption spectrum of a) Ag NPs, b) Ag@vanadate NPPs obtained using solvent evaporation approach, and c) solvothermally-synthesized Ag@vanadate NPPs.

While the free Ag NPs show an SPR at 409 nm, the Ag@vanadate NPPs, synthesized by both solvent evaporation and solvothermal approaches, are progressively shifted to higher wavelengths of 419 nm and 428 nm, respectively. The red shift in the SPR of the NPPs is attributed to NP-NP interactions as well as interactions with the vanadate nanoscrolls. The higher loadings and smaller average interparticle distances seen in the solvothermally-prepared Ag@vanadate NPPs (Figure 3.2c) appear to lead to the greater overall redshift. Our group recently observed similar relative SPR behavior in solvothermally-prepared Au@hexaniobate NPPs.[18]

Of further interest in these vanadate systems is an unusual scrolling feature seen in some of the solvothermally-prepared NScs and NPPs. Asymmetrical structures, where unequal interlayer spacings within opposite walls of the same NScs or NPPs, are observed (Figure 3.12). For example, the top left of the scrolls in both Figures 3.12a and 3.12b show an eccentric interlayer spacing that is approximately three times larger on the right side than the left. Interestingly, in the asymmetric NPPs the NPs appear to always align towards the side of the scroll with the smaller interlayer spacing (Figures 3.12b and 3.13).
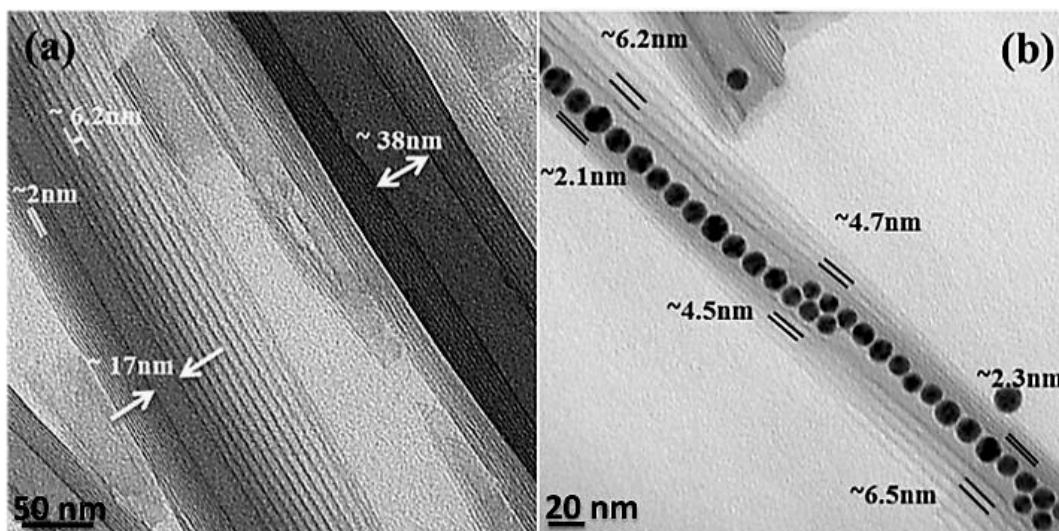
Figure 3.12. TEM images showing different layers spacing of a) asymmetric NScs and b) solvothermally-synthesized asymmetric NPP; NPs in the NPP are aligned towards the compressed set of walls versus the more open side of asymmetric scroll.
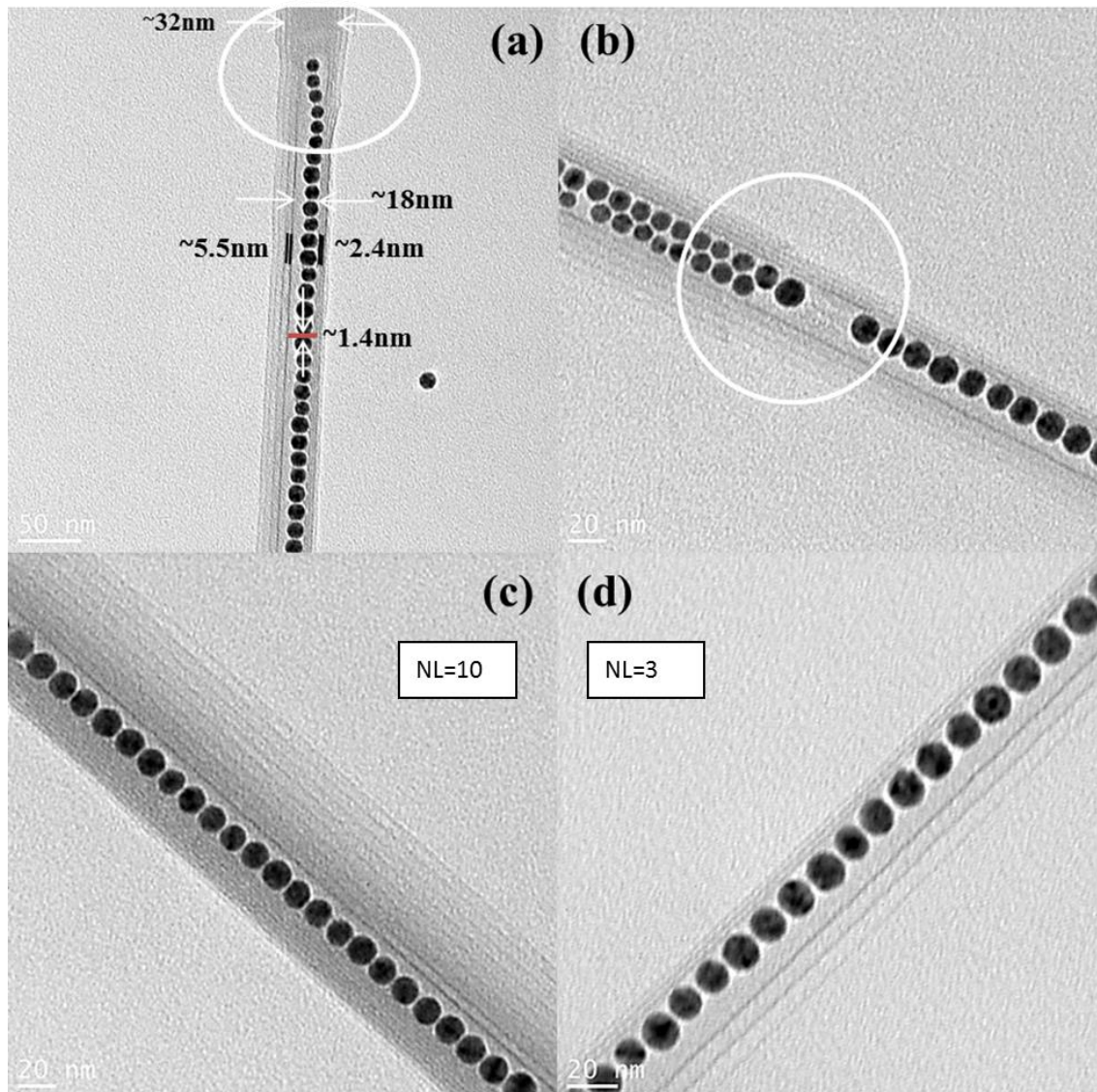
Figure 3.13. TEM images showing asymmetric Ag@vanadate NPPs synthesized using ST approach. (a) NPP shows different interlayer spacings (right side = 2.4 and left side = 5.2 nm), variation in inner diameter with (i.d. = 18 nm) and without NP encapsulation (i.d. = 32 nm), and an inter-particle distance of 1.4 nm. Circled areas in (a) shows the variation in both morphology and NSs inner diameter with and without NPs. Circled area in (b) shows a change in the number of layers in respect to the different NPs arrangement. (c,d) Asymmetric NPPs with different numbers of layers; 10 and 3 (NL = number of layers).

Although the formation mechanism of asymmetric NPPs is not completely clear, it does relate to an uneven distribution of surfactant within the interlayers of the scroll structure. The arrangement and attachment of NPs to one side of the NScs may induce deformation due to

internal strain in the structure that might be released by an increase in layer spacing on the opposite side of the NScs. (Figure 3.14).
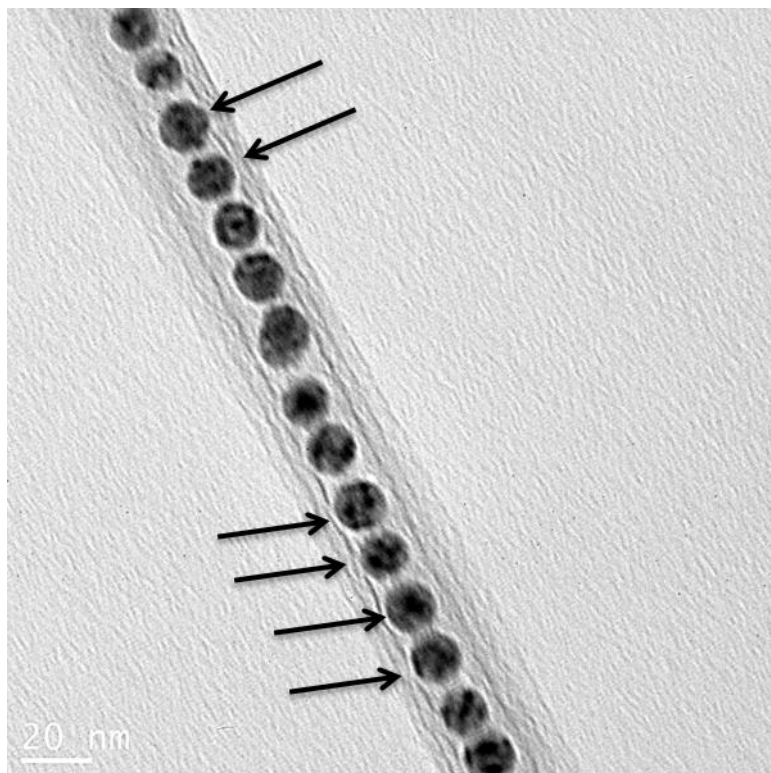
Figure 3.14. TEM image showing the dark line contrast for the deformation of layers and strain induced by attachment of NPs to one side of asymmetric solvothermally-synthesized Ag@vanadate NPPs.

The interlayer spacing ratio for the asymmetric NPPs varies from 1.3 to approximately 3.8. Based on TEM observations, it can be estimated that the fraction of eccentric NScs as well as NPPs formed using solvent evaporation approach is about 5-10%, while in the case of solvothermally synthesized NPPs, it's approximately 10-15%. Methods are currently being sought to make bulk quantities of these asymmetric nanostructures.

3.4 Conclusions

Two distinct methods for the formation of vanadate based NPPs have been developed. These synthetic approaches are simple and versatile so that by optimizing reaction parameters a variety of NPs could easily be encapsulated inside vanadate NScs. These novel NPPs can open captivating possibilities for the physical and chemical exploration of advanced nanocomposites and hold great potential for future technologies such as those involving sensors, catalysts, and lithium ion batteries. Furthermore, the formation of peapods with layered vanadates suggests that these fabrication methods could be readily extended to a range of other layered hosts where peapod composites made with materials like layered perovskites, metal dichalcogenides, hexagonal boron nitride, or graphene might be readily obtained.

3.5 References

1. Pileni, M.-P., Nanocrystal Self-Assemblies: Fabrication and Collective Properties. The *J. Phys. Chem. B* **2001**, 105, 3358.
2. Taleb, A.; Petit, C.; Pileni, M., Optical Properties of Self-Assembled 2D and 3D Superlattices of Silver nanoparticles. *J. Phys. Chem. B*,**1998**, 102, 2214.
3. Tang, Z.; Kotov, N. A., One-Dimensional Assemblies of Nanoparticles: Preparation, Properties, and Promise. *Adv. Mater.***2005**, 17, 951.
4. Zhu, Z.; Liu, W.; Li, Z.; Han, B.; Zhou, Y.; Gao, Y.; Tang, Z., Manipulation of Collective Optical Activity in One-Dimensional Plasmonic Assembly. *ACS Nano***2012**, 6, 2326.
5. Liu, S.; Tang, Z.-R.; Sun, Y.; Colmenares, J. C.; Xu, Y.*-J.,* One-Dimension-Based Spatially Ordered Architectures for Solar Energy Conversion. *Chem. Soc. Rev.* **2015**.
6. Weng, B.; Liu, S.; Tang, Z.-R.; Xu, Y.-J., One-Dimensional Nanostructure Based Materials for Versatile Photocatalytic Applications. *RSC Advances* **2014**, 4, 12685.
7. Zhang, N.; Fu, X.; Xu, Y.-J., A Facile and Green Approach to Synthesize Pt@ CeO $_2$Nanocomposite with Tunable Core-Shell and Yolk-Shell Structure and its Application as a Visible Light Photocatalyst. *J. Mater. Chem.* **2011**, 21, 8152.
8. Kitching, H.; Shiers, M. J.; Kenyon, A. J.; Parkin, I. P., Self-assembly of Metallic Nanoparticles into One Dimensional Arrays. *J. Mater. Chem.* A **2013**, 1, 6985.
9. Zhang, N.; Xu, Y.-J., Aggregation-and Leaching-Resistant, Reusable, and Multifunctional Pd@ CeO$_2$ as a Robust Nanocatalyst Achieved by a Hollow Core–Shell Strategy. *Chem. Mater.* **2013**, 25, 1979.
10. Campion, A.; Kambhampati, P., Surface-Enhanced Raman Scattering. *Chem. Soc. Rev.***1998**, 27, 241.
11. Kneipp, K.; Wang, Y.; Kneipp, H.; Perelman, L. T.; Itzkan, I.; Dasari, R. R.; Feld, M. S., Single Molecule Detection using Surface-Enhanced Raman Scattering (SERS). *Phys. Rev. Lett.***1997**, 78, 1667.
12. Schlücker, S., urface-Enhanced Raman Spectroscopy: Concepts and Chemical Applications. *Angew. Chem. Int. Ed.***2014**, 53, 4756.
13. Graham, D., The Next Generation of Advanced Spectroscopy: Surface Enhanced Raman scattering from Metal Nanoparticles. *Angew. Chem. Int. Ed.***2010**, 49, 9325.
14. Hunyadi, S. E.; Murphy, C. *J.,* Tunable One-Dimensional Silver-Silica Nanopeapod Architectures. *J. Phys. Chem. B.***2006**, 110, 7226.

15. Cong, V. T.; Ganbold, E.-O.; Saha, J. K.; Jang, J.; Min, J.; Choo, J.; Kim, S.; Song, N. W.; Son, S. J.; Lee, S. B., Gold Nanoparticle Silica Nanopeapods. *J. Am. Chem. Soc.***2014**, *136*, 3833.

16. Zhang, H.; Bai, Y.; Zhang, Y.; Li, X.; Feng, Y.; Liu, Q.; Wu, K.; Wang, Y., Designed Synthesis of Transition Metal/Oxide Hierarchical Peapods Array with the Superior Lithium Storage Performance. *Sci. Rep. s***2013**, *3*.

17. Adireddy, S.; Carbo, C. E.; Yao, Y.; Vargas, J. M.; Spinu, L.; Wiley, J. B., High-Yield Solvothermal Synthesis of Magnetic Peapod Nanocomposites via the Capture of Preformed Nanoparticles in Scrolled Nanosheets. *Chem. Mater.***2013**, *25*, 3902.

18. Adireddy, S.; Carbo, C. E.; Rostamzadeh, T.; Vargas, J. M.; Spinu, L.; Wiley, J. B., Peapod-Type Nanocomposites through the In Situ Growth of Gold Nanoparticles within Preformed Hexaniobate Nanoscrolls. *Angew. Chem. Int. Ed.***2014**, *53*, 4614.

19. Patzke, G. R.; Krumeich, F.; Nesper, R., Oxidic Nanotubes and Nanorods—Anisotropic Modules for a Future Nanotechnology. *Angew. Chem. Int. Ed.***2002**, *41*, 2446.

20. Krumeich, F.; Muhr, H.-J.; Niederberger, M.; Bieri, F.; Schnyder, B.; Nesper, R., Morphology and Topochemical Reactions of Novel Vanadium Oxide Nanotubes. *J. Am. Chem. Soc.***1999**, *121*, 8324.

21. Mai, L.; Chen, W.; Xu, Q.; Zhu, Q.; Han, C.; Peng, J., Cost-Saving Synthesis of Vanadium Oxide Nanotubes. *Solid State Commun.***2003**, *126*, 541.

22. Corr, S. A.; Grossman, M.; Furman, J. D.; Melot, B. C.; Cheetham, A. K.; Heier, K. R.; Seshadri, R., Controlled Reduction of Vanadium Oxide Nanoscrolls: Crystal Structure, Morphology, and Electrical Properties. *Chem. Mater.***2008**, *20*, 6396.

23. Zhang, K.-F.; Guo, D.-J.; Liu, X.; Li, J.; Li, H.-L.; Su, Z.-X., Vanadium Oxide Nanotubes as the Support of Pd Catalysts for Methanol Oxidation in Alkaline Solution. *J. Power Sources* **2006**, *162*, 1077.

24. Jin, W.; Dong, B.; Chen, W.; Zhao, C.; Mai, L.; Dai, Y., Synthesis and Gas Sensing Properties of Fe_2O_3 Nanoparticles Activated V_2O_5 Nanotubes. *Sensor Actuat B-Chem.***2010**, *145*, 211.

25. Wang, C.; Yin, H.; Chan, R.; Peng, S.; Dai, S.; Sun, S., One-Pot Synthesis of Oleylamine Coated AuAg Alloy NPs and Their Catalysis for CO Oxidation.*Chem. Mater.***2009**, *21*, 433.

26. Xu, Z.; Shen, C.; Hou, Y.; Gao, H.; Sun, S., Oleylamine as Both Reducing Agent and Stabilizer in a Facile Synthesis of Magnetite Nanoparticles. *Chem. Mater.***2009**, *21*, 1778.

27. Corr, S. A.; Grossman, M.; Furman, J. D.; Melot, B. C.; Cheetham, A. K.; Heier, K. R.; Seshadri, R., Controlled Reduction of Vanadium Oxide Nanoscrolls: Crystal Structure, Morphology, and Electrical Properties. *Chem. Mater.***2008**, *20*, 6396.

28. Rostamzadeh, T.; Wiley, J. B. "Rapid Large-Scale Synthesis of Vanadate Nanoscrolls with Controllable Lengths" (manuscript in preparation).

29. Adireddy, S.; Rostamzadeh, T.; Carbo, C. E.; Wiley, J. B., Particle Placement and Sheet Topological Control in the Fabrication of Ag–Hexaniobate Nanocomposites. *Langmuir***2014**.

30. Yao, Y.; Chaubey, G. S.; Wiley, J. B., Fabrication of Nanopeapods: Scrolling of Niobate Nanosheets for Magnetic Nanoparticle Chain Encapsulation. *J. Am. Chem. Soc.***2011**, *134*, 2450.

31. Chen, X.; Sun, X.; Li, Y., Self-Assembling Vanadium Oxide Nanotubes by Organic Molecular Templates. *Inorg. Chem.***2002**, *41*, 4524.

32. Niederberger, M.; Muhr, H.-J.; Krumeich, F.; Bieri, F.; Günther, D.; Nesper, R., Low-Cost Synthesis of Vanadium Oxide Nanotubes via Two Novel Non-Alkoxide Routes. *Chem. Mater.***2000**, *12*, 1995.

33. Spahr, M. E.; Bitterli, P.; Nesper, R.; Müller, M.; Krumeich, F.; Nissen, H. U., Redox-Active Nanotubes of Vanadium Oxide. *Angew. Chem. Int. Ed.***1998**, *37*, 1263.

34. Chen, W.; Peng, J.; Mai, L.; Zhu, Q.; Xu, Q. , Synthesis of Vanadium Oxide Nanotubes from V_2O_5 Sols. *Mater. Lett.***2004**, *58*, 2275.

35. Zhao, L.; Kelly, K. L.; Schatz, G. C., The Extinction Spectra of Silver Nanoparticle Arrays: Influence of Array Structure on Plasmon Resonance Wavelength and Width. *J. Phys. Chem. B.***2003**, *107*, 7343.

36. Lamprecht, B.; Schider, G.; Lechner, R.; Ditlbacher, H.; Krenn, J.; Leitner, A.; Aussenegg, F., Metal Nanoparticle Gratings: Influence of Dipolar Particle Interaction on the Plasmon Resonance. *Phys. Rev. Lett.***2000**, *84*, 4721.

37. Su, K.-H.; Wei, Q.-H.; Zhang, X.; Mock, J.; Smith, D. R.; Schultz, S., Interparticle Coupling Effects on Plasmon Resonances of Nanogold Particles. *Nano Lett.***2003**, *3*, 1087.

38. Wei, Q.-H.; Su, K.-H.; Durant, S.; Zhang, X., Plasmon Resonance of Finite One-Dimensional Au Nanoparticle Chains. *Nano Lett.***2004**, *4*, 1067.

Chapter 4 Formation of MoO_x-Organic Hybrid Structures and MoO_x Nanosheets

4.1 Introduction

After the discovery of the free standing monolayer of graphene and its distinctive properties,[1] several attempts have been made to explore different synthetic approaches for making other inorganic nanosheets (NSs) including hexagonal boron nitrate (h-BN),[2] clays,[3] transitional metal dichalcogenides (TMDs),[4] metal oxides and other 2D NSs.[5] Layered materials are usually composed of strong chemical bonds in-plane and weak ones out of plane (e.g. van der Waals).[5, 6] The large interlayer distances of layered materials can be further expanded upon intercalation of guest molecules/ions between the layers.[7] This expansion may result in additional weakening of interlayer attractions in such a way that single or a few layers of 2D NSs can be separated via subsequent sonication.[5-7] Though there are a large number of publications on the formation of variety of 2D materials from their 3D counterparts, only a few of these reports focus on the formation of MoO_3 NSs.[8, 9]

MoO_3, an important layered transition metal oxide, has been of interest for its functional behavior including photochromic, thermochromics, and electrochromic properties.[8] α-MoO_3 and β-MoO_3 are two most common crystal phases of molybdenum trioxide.[10,11] β-MoO_3 is thermodynamically metastable phase and spontaneously transforms to α-MoO_3 at between 370-400°C.[12] Orthorhombic α-MoO_3, in contrast, is the most stable phase at room temperature. It is a wide band gap semiconductor with a band gap of 3.2 eV. α-MoO_3 has a layered structure with lattice constants of a=3.944 Å, b=13.982 Å, and c=3.737 Å where the layers are positioned parallel to (010) crystal plane, along the b axis (Figure 4.1).[10,11] Each layer consists of two sublayers composed of distorted edge-sharing MoO_6 octahedra that corner-share along the [100] direction.[10–12] Due to the large layer spacings and weak layer interactions, organic compounds can be inserted between the α-MoO_3 layers leading to the formation of organic-inorganic hybrids where new properties arise from the interplay of both organic and inorganic components.[13, 14]

Although localized surface plasmon resonance (LSPR)[15,16] is widely studied and known in the case of noble metals, it can also be achieved for heavily doped semiconductors.[8,17] For example, copper chalcogenide,[18,19] zinc oxide,[20] and tin oxide[21] have been reported to show

tunable LSPR through different amounts of doping and, thus, through the achievement of a suitable free-carrier concentration. Among the few reports published on the formation of MoO_3
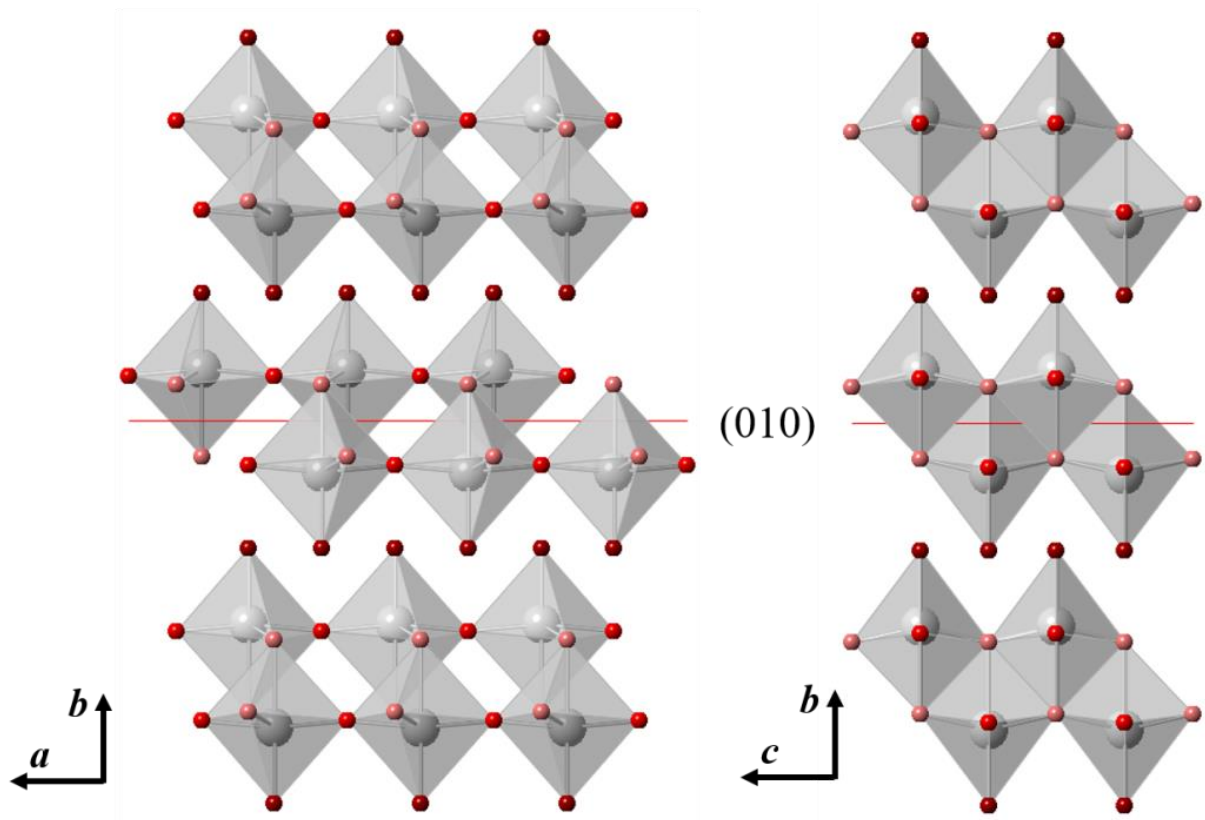
Figure 4.1. Crystal structure of MoO_3 viewed from two perpendicular directions.

NSs is the synthesis of plasmonic oxygen-deficient MoO_{3-x} NSs that are seen when molybdenum powders are oxidized with hydrogen peroxide followed by solvothermal treatment (ST) in ethanol.[17] Huang *et al.* also reported the ST formation of an oleylamine (OAm) hybrid, MoO_{3-x}-OAm NSs, from an ammonium molybdate precursor.[22]

In this chapter, large (≤ 4 μ) hexagonal MoO_3 NSs (individual or ultrathin) are formed using a ST treatment of MoO_3 with dodecylamine (DDA), followed by sonication. Moreover, a novel ST synthetic route is reported for the formation of highly-ordered plasmonic MoO_{3-x}-OAm NSs from widely available MoO_3 and oleylamine. Reduction and subsequent phase transformation of hybrid MoO_{3-x}-OAm to layered MoO_2 NPs is also observed.

4.2 Experimental

Reagents. Toluene (99.8%, anhydrous), Oleic acid (99.8%, OAc), oleylamine (>70%, OAm), dodecylamine (98%, DDA), octadecylamine (98%, ODA), hexadecylamine (98%, HDA), tetrabutylammonium hydroxide 30-hydrate (97%, TBAOH), and molybdenum (VI) oxide ($\geq$ 99.6%), were purchased from Sigma-Aldrich.

Solvothermal synthesis of molybdenum oxide-DDA hybrid and formation of hexagonal-shaped molybdenum oxide NSs. Hexagonal-shaped molybdenum oxide NSs with up to four micrometers in their lateral size were synthesized. First, dodecylamine (0.4 g, 2.15 mmol) was dissolved in 5.5 mL of ethanol. Then, molybdenum (VI) oxide (0.4 g, 2.788 mmol), toluene (5.5 mL), and OAc (2 mL) were added to the ethanol solution and magnetically stirred for 5 minutes. The final mixture was transferred into a 23 mL Teflon-lined stainless-steel autoclave (Parr, model 4749, 1800 psig, 23 mL) and solvothermally treated at 180 °C for different reaction times. After each reaction the autoclave was removed from the oven and cooled down to room temperature (~1 °C/min). The obtained product was washed first with toluene and then with ethanol and precipitated by centrifugation. Via multiple rapid centrifugation steps (<30 seconds), the lighter part of the sample, which consists of intercalated/exfoliated layers, was separated from the rest of the sample by isolating the supernatant. After each centrifugation step, the obtained supernatant was transferred to another centrifuge tube and further centrifuged (toluene used as the solvent). For the last step, the acquired supernatant was transferred to another tube and a longer centrifugation (≈5 minutes) was done to precipitate the exfoliated/intercalated products. These steps are referred to as the separation process throughout the paper.

Solvothermal Synthesis of highly-oriented MoO$_{3-x}$–OAm hybrid nanostructures. Molybdenum (VI) oxide (0.2 g, 1.389 mmol), TBAOH (0.2 g, 0.77 mmol), OAm (5 mL), and toluene (5 mL) were mixed in a vial and sonicated for one minute. The final mixture was transferred into a 23 mL Teflon-lined stainless-steel autoclave (Parr, model 4749, 1800 psig, 23 mL) and solvothermally treated at 180°C for several days. After the reaction, the autoclave was removed from the oven and cooled down to room temperature (~1°C/min). In order to remove the unreacted amine, the product was washed twice with toluene and separated by centrifugation. For transmission electron microscopy (TEM) measurements, samples were dispersed in toluene,

sonicated for 10 seconds and then drop cast onto a 200 mesh carbon-coated copper grid. ST times and temperatures were varied to investigate their effect on NS formation.

Characterization. A JEOL 2010 TEM operated at an accelerating voltage of 200 kV, equipped with an EDAX genesis energy dispersive spectroscopy (EDS) system, was used to characterize various products. A Philips X-Pert PW 3040 MPD equipped with a curved graphite monochromator operating at 45 kV accelerating voltage and 40 mA current was used to collect X-ray diffraction (XRD) data. Formation of NSs and highly ordered layered structures was also investigated at room temperature with an Asylum Research MFP-3D atomic force microscopy (AFM) working in the dual amplitude resonance tracking (DART) mode. Absorption spectra were recorded with a Cary 500 UV-Vis spectrophotometer on samples dispersed in toluene. A TA Instruments (TGA-DSC SQ600 system) was used to collect thermogravimetric (TGA) and differential scanning calorimetry (DSC) data; samples were heated in alumina pans under a dilute oxygen atmosphere (ca. 50% argon) up to 1000 °C at a heating rate of 25 °C/min.

4.3 Results

4.3.1. Formation of molybdenum oxide-DDA hybrid structures and hexagonal-shaped molybdenum oxide NSs

Hexagonal-shaped molybdenum oxide NSs with up to four micrometers in lateral size were synthesized via a ST treatment of molybdenum trioxide using dodecylamine (DDA) as an intercalating agent followed by a sonication and separation step. TEM images of the separated product obtained after 24 h of ST treatment at 180 °C are shown in Figure 4.2. TEM images display that the presented NSs are of hexagonal shape and have an average size of about 4 μm (Figure 4.2). The presence of ordered/assembled NSs with large interlayer spacings can clearly be perceived from Figure 4.2a and b. Single or a few layers of exfoliated NSs were also observed as displayed in Figure 4.2d.
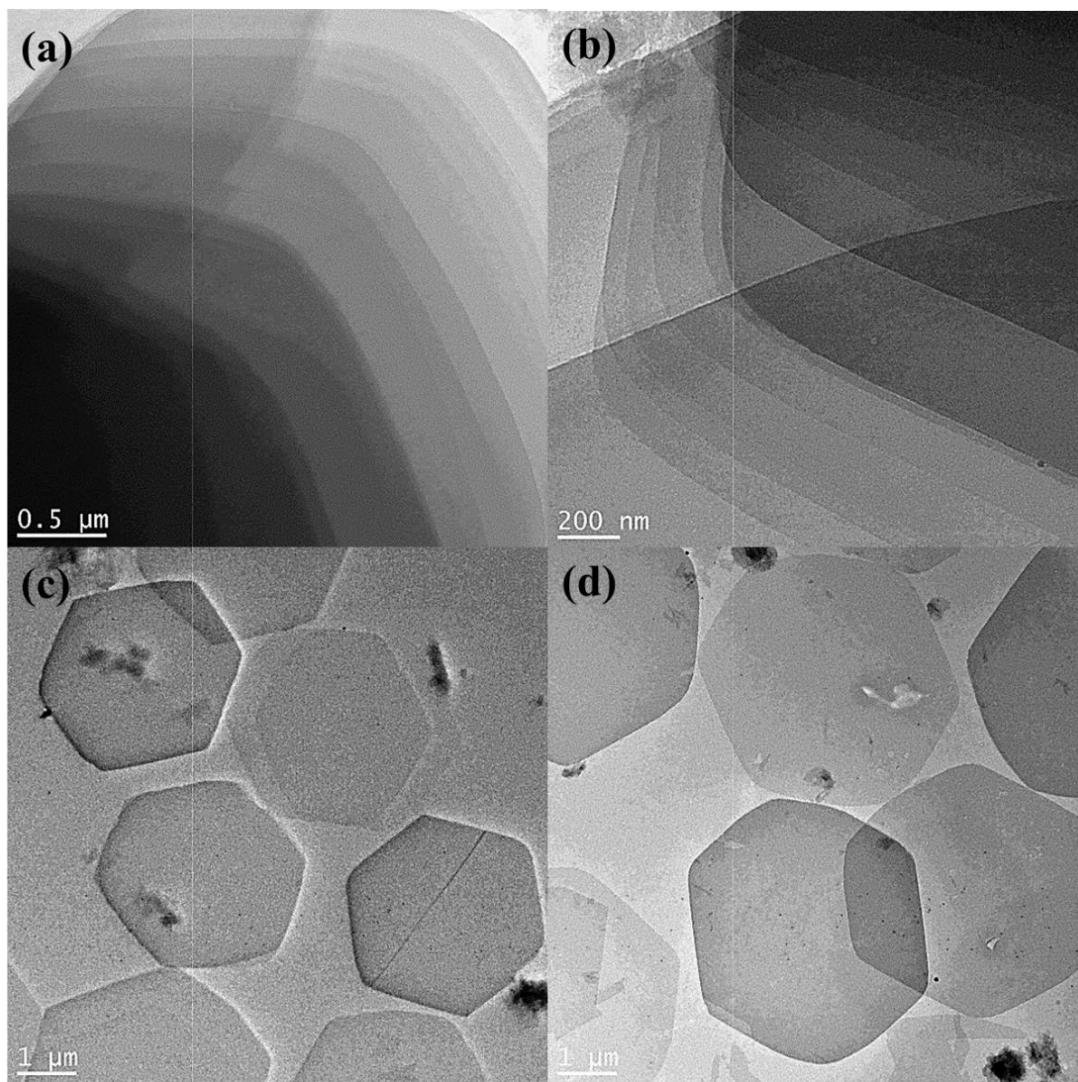
Figure 4.2. TEM images of single and multiple layers of hexagonal molybdenum oxide NSs obtained after 24 h of ST treatment at 180 °C in the presence of DDA.

XRD patterns of the product obtained before and after the separation process for the sample ST treated at 180 °C for 24 h are shown in Figure 4.3. The formation of inorganic-organic hybrid structures can be confirmed by the presence of low angle peaks with high intensity.[23] While the XRD pattern of the sample before the separation process shows two series of low and high angle reflections (Figure 4.3b), The XRD pattern of samples obtained after the separation process shows only low angle peaks (Figure 4.3c). Since the layers are positioned parallel to (010) crystal plane and along the *b* axis (Figure 4.1), low angle peaks appeared due to the intercalation of DDA between the (010) planes of MoO_x and, therefore, are indexed as (*0l0*) reflections

(Figure 4.3c). Using the lowest angle reflection (010), d-spacing of about 27.1 Å was calculated, which is equal to the layer spacings of the lamellar structure/intercalated compound. Comparable interlayer spacings were obtained in our previous studies on the formation of vanadate NScs where DDA was intercalated between the layers of vanadium pentoxide crystals.[24, 25]
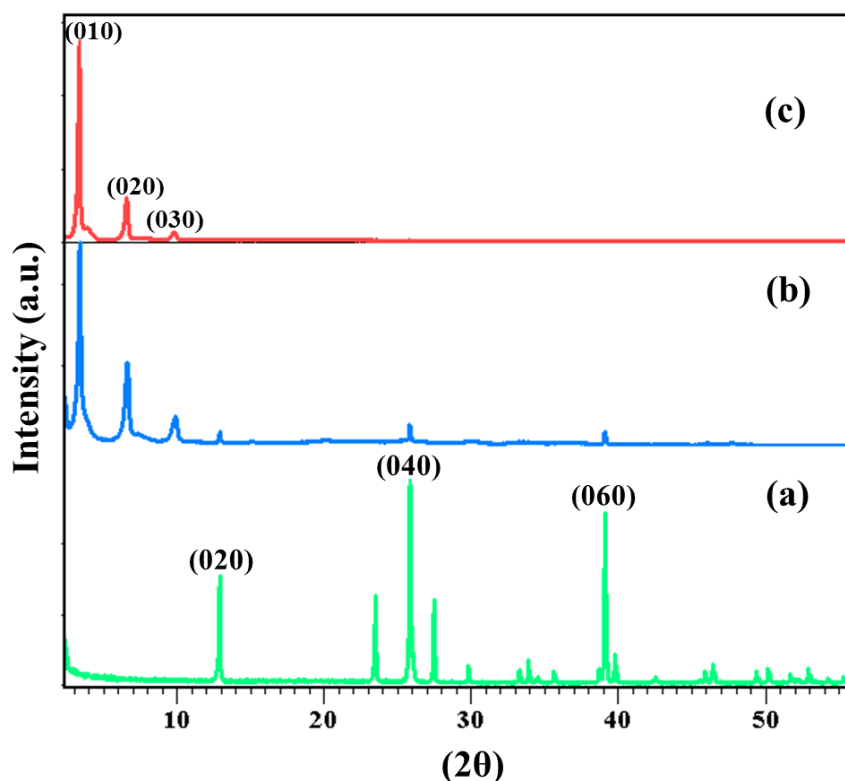
Figure 4.3. XRD patterns of (a) molybdenum oxide precursor ST-treated products obtained after 24 h of ST treatment at 180 °C in the presence of DDA (b) before and (c) after the separation process.

Control of layer spacings as a function of hydrocarbon chain lengths was also achieved. XRD patterns of molybdenum oxide intercalated using dodecylamine, hexadecylamine, and octadecylamine shown in Figure 4.4 exhibit the different layer spacings, 27.1Å, 32.6 Å, and 35.5 Å, respectively. The effects of time on the intercalation process of DDA into the layered structure of molybdenum oxide were also investigated. XRD patterns of the as-synthesized product, without any purification/separation obtained after different ST duration, are shown in Figure 4.5.
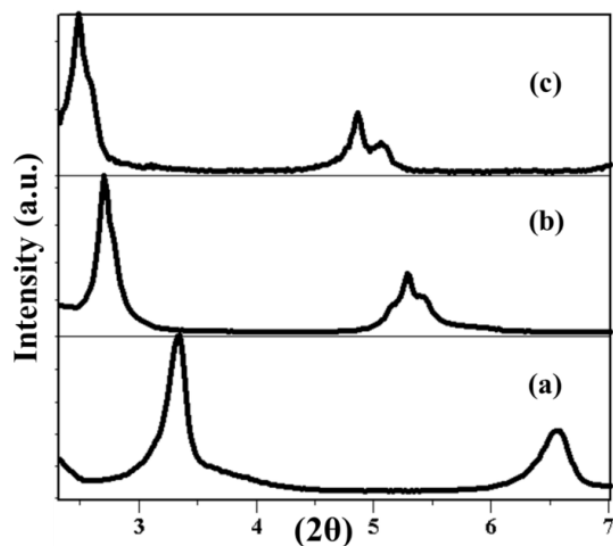
Figure 4.4. XRD patterns of a) dodecylamine, b) hexadecylamine, and c) octadecylamine intercalated molybdenum oxide structure.
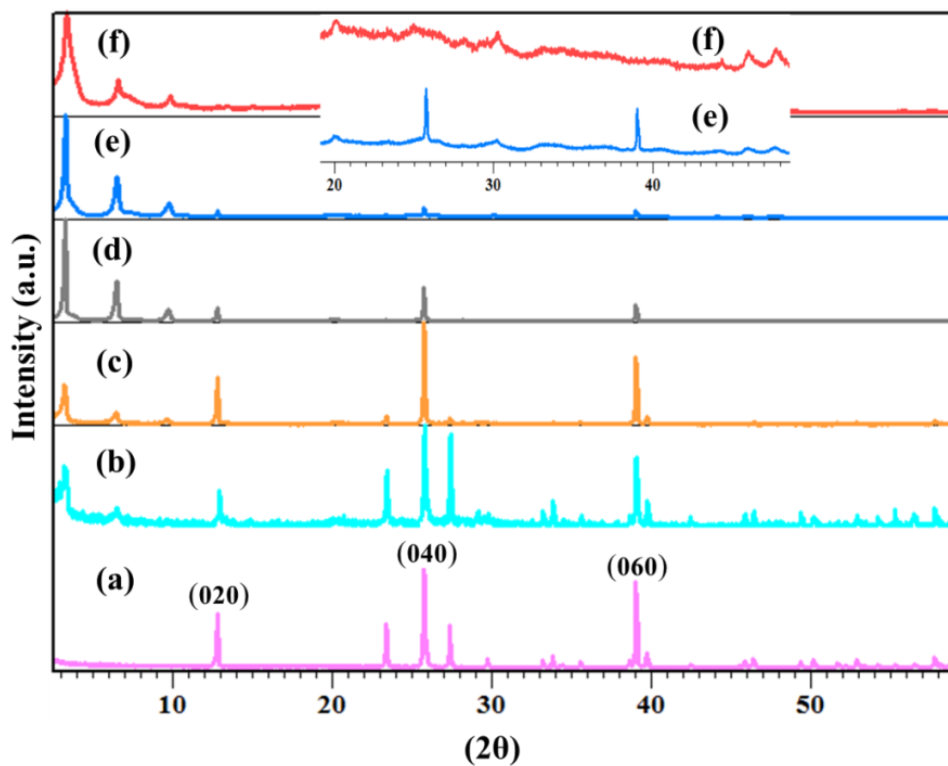
Figure 4.5. XRD patterns of a) molybdenum oxide precursor and obtained samples treated at 180°C in the presence of DDA for different durations of ST: b) 0.5h, c) 1h, d) 7h, e) 24h, and f) 72h. High angle peaks for e and f are highlighted in the inset.

The intensity ratio of low angle to high angle peaks coming from the intercalation of DDA and the (002), (004), and (006) reflections of starting materials, respectively, clearly increases with respect to ST duration (Figure 4.5). The XRD pattern of the sample obtained after 72h shows no peaks related to the starting materials, but the existence of several low intensity and broad peaks located at $2\theta = 20.09, 30.34, 46.06$, and $47.78°$. Weak traces of these reflections could also be noticed from the XRD pattern of the sample obtained after 24h. These peaks could not be indexed on any of the known molybdenum oxide crystal structures. TEM images (Figure 4.6) of the sample obtained after 72 h of ST treatment show decomposed/broken NSs possibly due to the strain induced by the formation of a new phase.
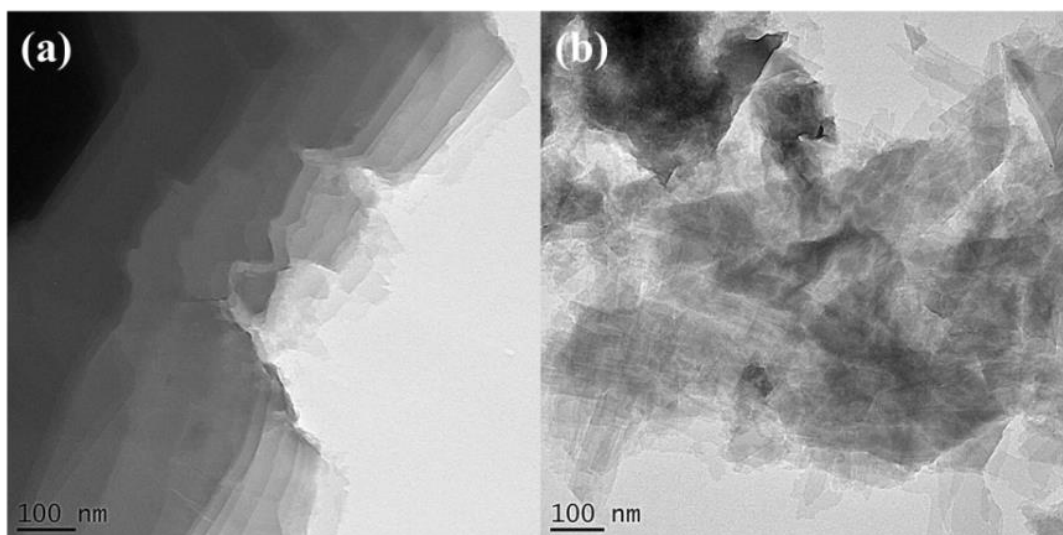
Figure 4.6. a and b) TEM images of NSs obtained after 72 h of ST treatment at 180 °C in the presence of DDA as an intercalating agent.

4.3.2 Formation of MoOx-OAm highly ordered nanosheets

A ST-treatment at 180°C utilizing the mixture of MoO_3, OAm, TBAOH, and toluene were applied for the formation of molybdenum oxide-OAm hybrid structure. Highly-oriented NSs with hexagonal shape were achieved after the ST-treatment at 180°C for several days (Figure 4.7a-c). It can also be perceived from Figure 4.7b that single layer or a few layers of MoO_x could easily be separated upon sonication.
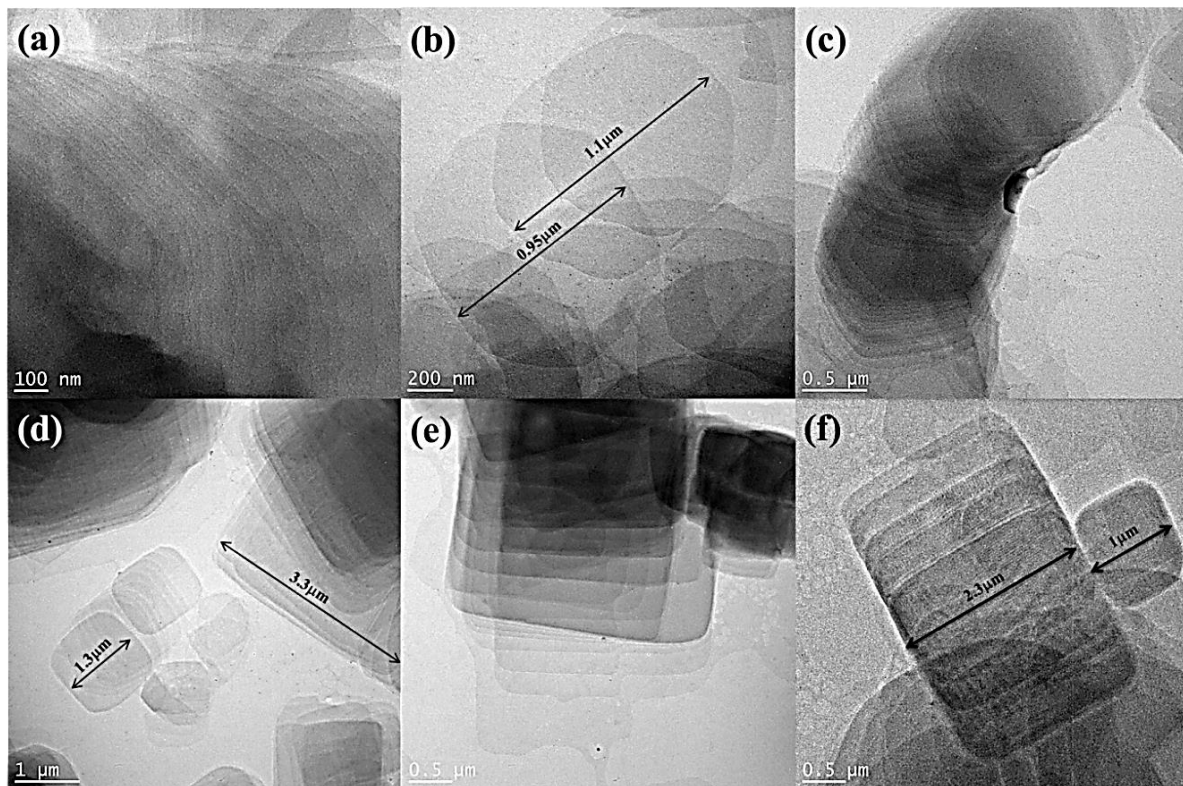
Figure 4.7. TEM images of molybdenum oxide NSs obtained after ST treatment at a, b) 180 °C for 72 h, c) 180 for 336 h (two weeks), and d, e, f) sample was first treated at 250 °C for 80 minutes and then 180 °C for 24 h.

Highly-oriented hexagonal NSs have a narrow size distribution with an estimated average size of ~ 1 μm. Increasing the reaction time from 72 h to 336 h (two weeks) did not have a noticeable influence on the shape and size of obtained NSs (Figure 4.7a-c); though it increased the ordering of NSs and intensity of (*0l0*) reflections revealed by XRD data. AFM images shown in Figure 4.8 further display the presence of assembled/ordered MoO_x NSs and are in a good agreement with presented TEM images (Figure 4.7a, and c).

Size and shape of NSs could further be modified via a two-step ST treatment. Square/rectangular like NSs were obtained after 80 minutes of ST treatment at 250°C and subsequent treatment at 180°C for 24h (Figure 4.10 d-f). The size of NSs varied between 800 nm to 5μm; estimated using low magnification TEM images.

75
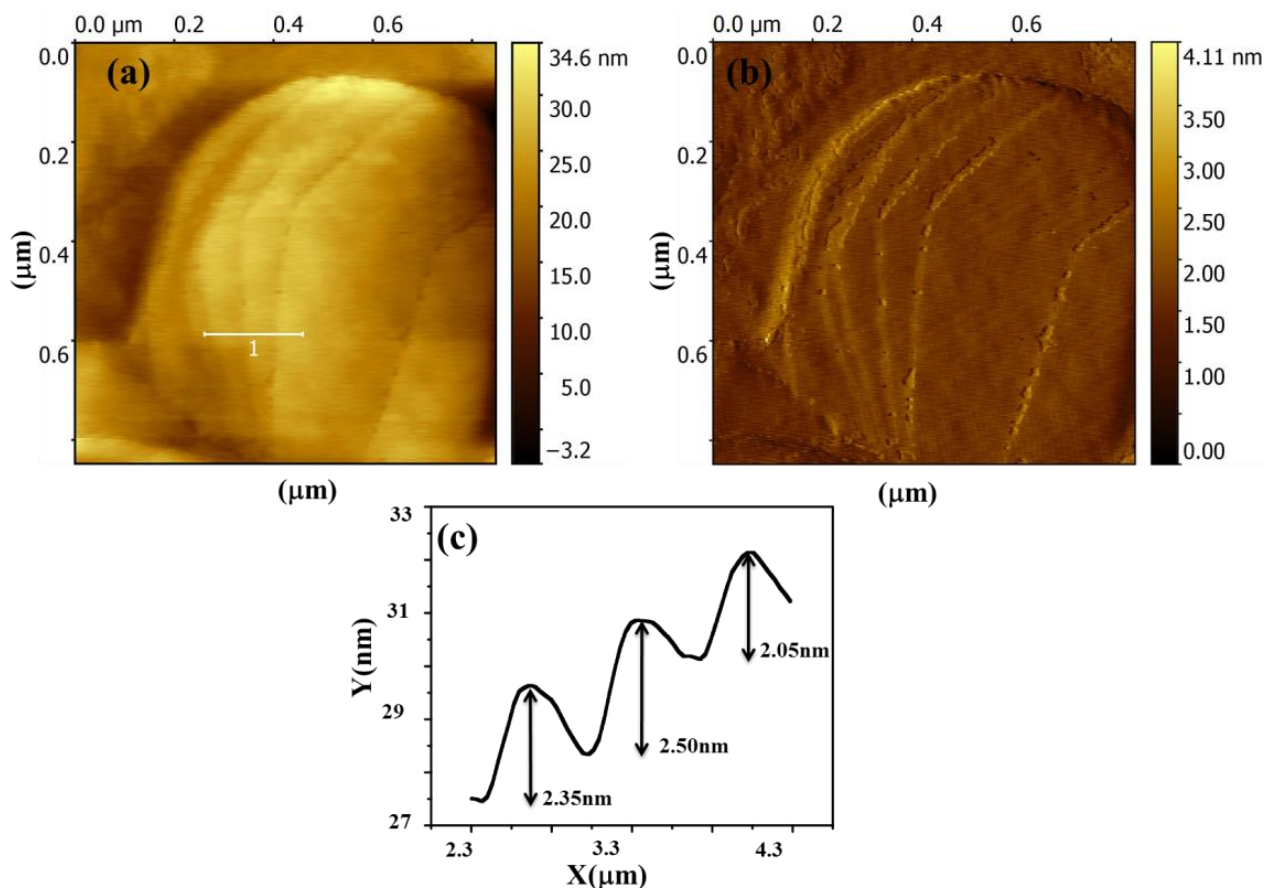
Figure 4.8. AFM (a) topography (b) amplitude and (c) height profile along the line shown in b. NSs were synthesized via a ST-treatment at 180°C for 72h.

XRD patterns for the sample solvothermally treated at 180°C for 336 h and the sample obtained after two steps of ST treatment (250°C for 80 minutes followed by another ST treatment at 180°C for 24 h) are presented in Figure 4.9. Formation of highly–oriented molybdenum oxide NSs is further confirmed by a series of extremely high intensity peaks at low angles as well as high angle peaks that could all be indexed as (*0l0*) reflections with b = 35.95 Å (Figure 4.9a). From the high intensity peaks at low angles, *d*-spacings for the sample obtained after two steps of ST-treatment were also calculated to be 38.95 Å (Figure 4.9b). There are, however, several high angle peaks shown in the inset for this particular sample which could not be indexed to any of the known MoO$_x$ crystal structures (Figure 4.9b, inset).
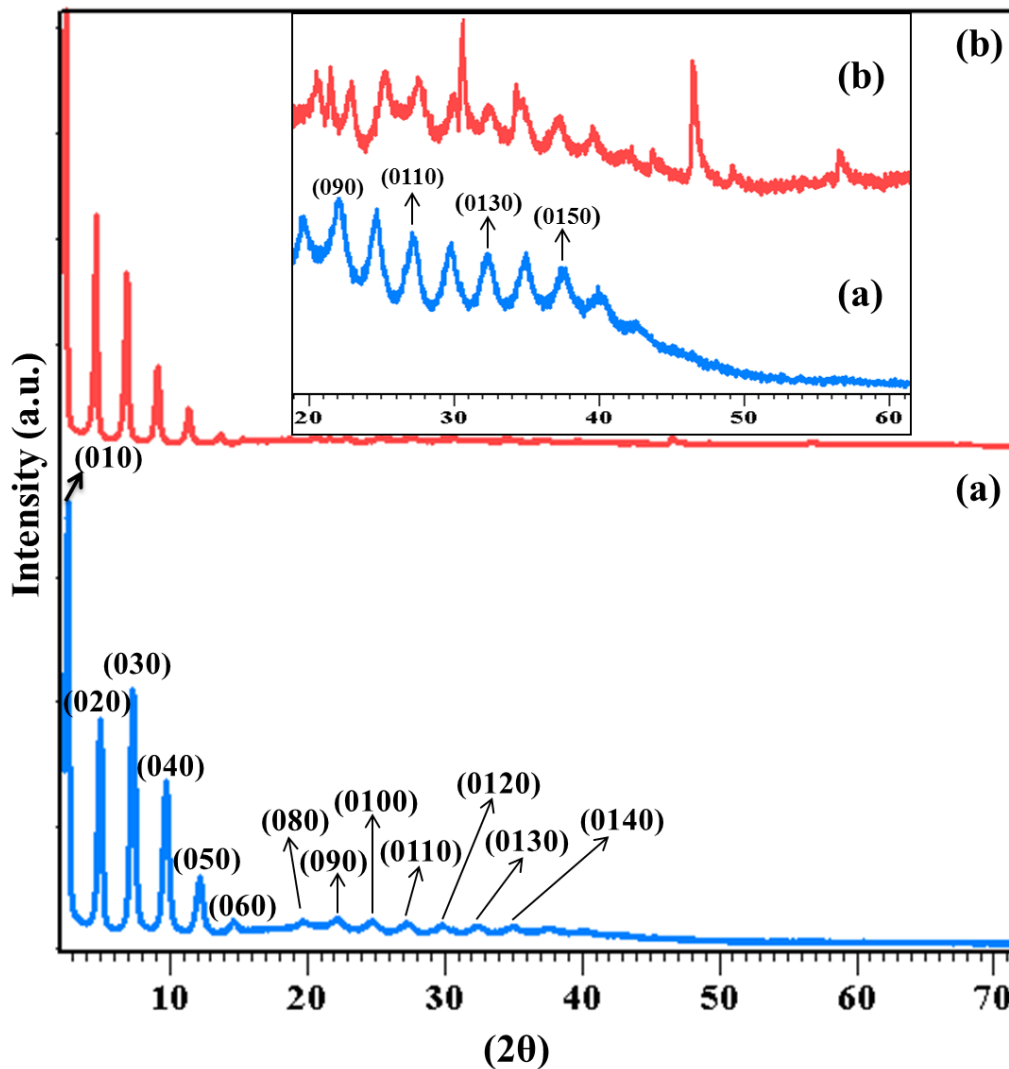
Figure 4.9. XRD patterns of molybdenum oxide NSs obtained after ST treatment a) at 180 °C for 336 h (b = 35.95 Å), and at b) at 250 °C for 80 minutes followed by another ST treatment at 180 °C for 24 h (layer spacings = 38.95 Å). The inset highlights the high angle peaks.

In order to further investigate the ST duration and temperature on the formation of MoO_x – OAm NSs, similar ST treatment was conducted at 240°C for different time intervals. XRD patterns of molybdenum oxide precursor and obtained products at different ST duration are shown in Figure 4.10. The presence of low angle peaks for the sample obtained after 30 minutes of ST treatment (Figure 4.10b) indicate the intercalation of OAm between the layers of α-MoO_3 ((*0l0*) planes).[22] High angle peaks were also located at 2θ =12.93, 25.84, and 39.02°, corresponding to the (020), (040), and (060) reflections of MoO_3 precursor, respectively (Figure

4.10b). When the ST duration is increased to 40 and 70 minutes, the high angle peaks of MoO_3 precursor are no longer observed (Figure 4.10c, and d). Complete intercalation of OAm and formation of highly ordered structure is confirmed by a series of extremely high intensity reflections at low angles as well as high angle peaks that could all be indexed as (*0l0*) reflections with b = 35.198Å and b = 33.822 Å for the samples obtained after 90 minutes and 120 minutes of ST treatment, respectively (Figure 4.10e and f). Similar XRD patterns with small variations for the layer spacings (b) were acquired for the samples obtained after 150 minutes and 180 minutes of ST treatment. The calculated d spacing for MoO_x – OAm hybrid structure obtained at different times and temperatures are comparable to double layers of OAm within the layers.
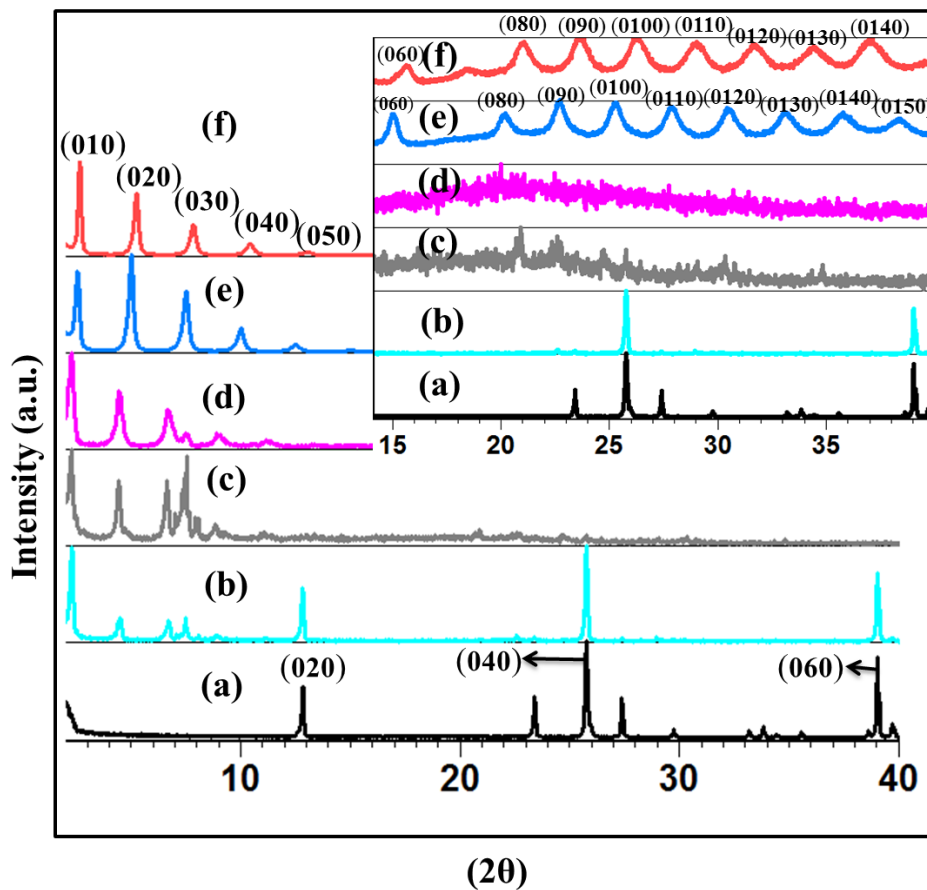
Figure 4.10. XRD patterns of a) molybdenum oxide precursor and obtained samples treated at 240 °C for different ST reaction times: b) 30 min, c) 40 min, d) 70 min, e) 90 min, and f) 120 min.

The obtained products, which are highly hydrophobic, likely due to the presence of OAm on the surface of molybdenum oxide NSs, were dispersed in toluene and drop casted on TEM grids right after the centrifugation process. TEM images of the sample obtained at different ST duration are shown in Figure 4.11. It can be realized that the NSs obtained after 30 and 40 minutes of the reaction do not have a specific shape. Formation of ordered NSs can be seen for the samples obtained after 70 minutes. (Figure 4.11c and d). For the sample treated for 40 minutes, a small portion of NSs were found to form nanoscrolls (NScs); these NScs were only occasionally observed during TEM. However, when the solid product obtained after 40 and 70 minutes of ST treatment were left in the centrifuge tubes in the air atmosphere for several days, NSs converted to a NSc geometry.
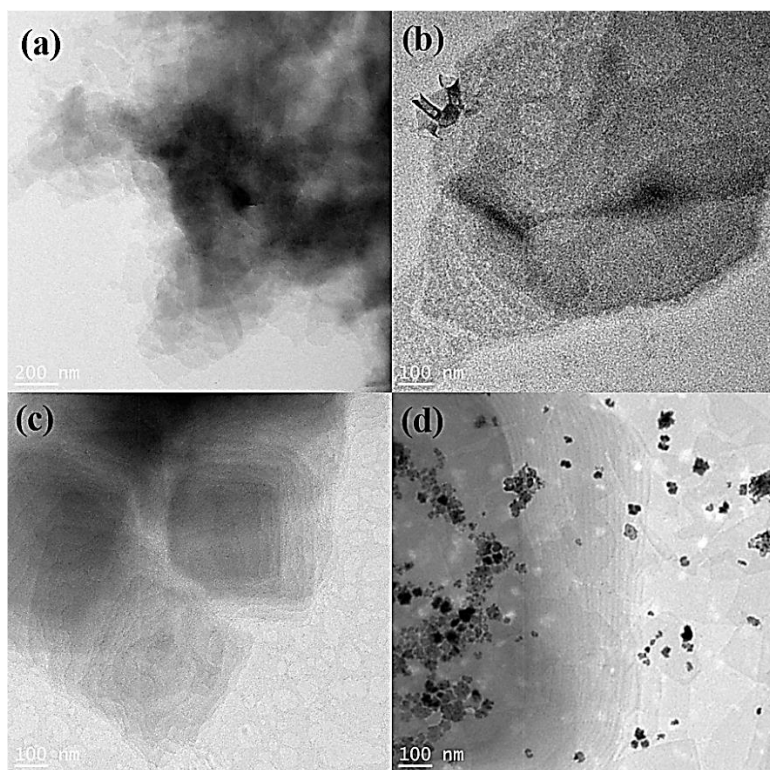
Figure 4.11. TEM images of the samples ST treated at 240°C for a) 30 min, b) 40 min, c) 70 min, and d) 120 min.

TEM images of NScs formed after 10 days are shown in Figure 4.12. As seen in Figure 4.11d, a further increase in reaction time to 120 minutes led to the formation of NPs, which

79

coexist with NSs (Figure 4.11d). The product obtained after 150 minutes of ST treatment also consisted of NPs and NSs (Figure 4.13).
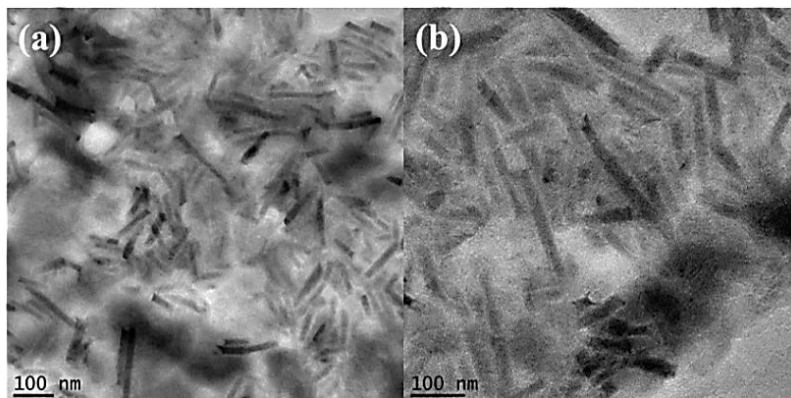
Figure 4.12. a and b) different magnifications TEM images showing the formation of NScs from NSs. Samples were initially treated solvothermally for 70 minutes and after centrifugation process kept for 10 days within the centrifuge tube (solid form).
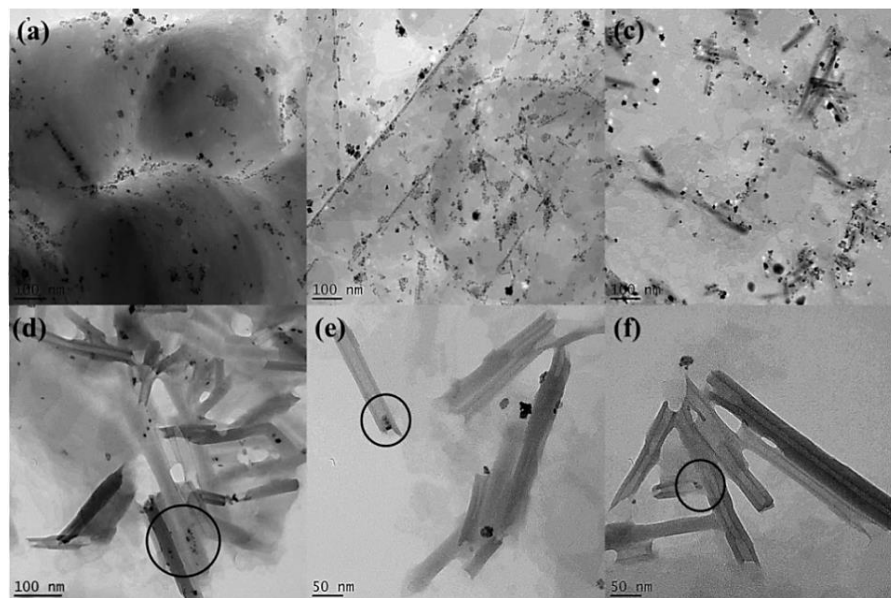
Figure 4.13. TEM images obtained after 150minutes h of ST treatment. a, b) TEM sample were provided right after the ST treatment. TEM sample were prepared after keeping the solid sample inside the centrifuge tube for c) 4 days (96h), d, e, and f) 10 days (240h). Circles in d-f show NPs encapsulated within NScs.

Similarly, TEM images of the solid product, which were obtained after centrifugation process and kept inside the centrifuge tubes for different time intervals, were taken and are shown in Figure 4.13c-f. NSs start their transformation to a NSc geometry after 4 days (Figure 4.13c). Complete scrolling of several NSs was seen after 10 days (Figure 4.13d-f). Interestingly, some of the NPs were captured during the scrolling of MoO_x NSs, thus leading to the formation of nanopeapods (marked area in Figure 4.13d-f). Currently methods for large scale production of MoO_x NPPs following the same ST approach, but with preformed NPs, are being investigated.

In order to further investigate the effect of reaction time on the formation of NPs, ST duration was increased up to 7 h. XRD patterns of the obtained product treated for 4.5 and 7 h, along with XRD reference pattern of MoO_2, are shown in Figure 4.14. For the sample treated for 4.5 h, except for those MoO_2 peaks observed at $2\theta =26.77, 36.99, 49.34$, and $53.53°$, all of the peaks can be indexed as ($0l0$) reflections where b=34.73 Å. The formation of MoO_2 from MoO_3 precursor indicate the reduction of Mo^{6+} to Mo^{4+} and phase transformation with respect to reaction time. When the reaction time increased to 7 h, the product is exclusively composed of MoO_2 phase (Figure 4.14b). TEM images of the layered structures and MoO_2 NPs obtained after 4, and 7 h of ST treatment are shown in Figure 4.15.
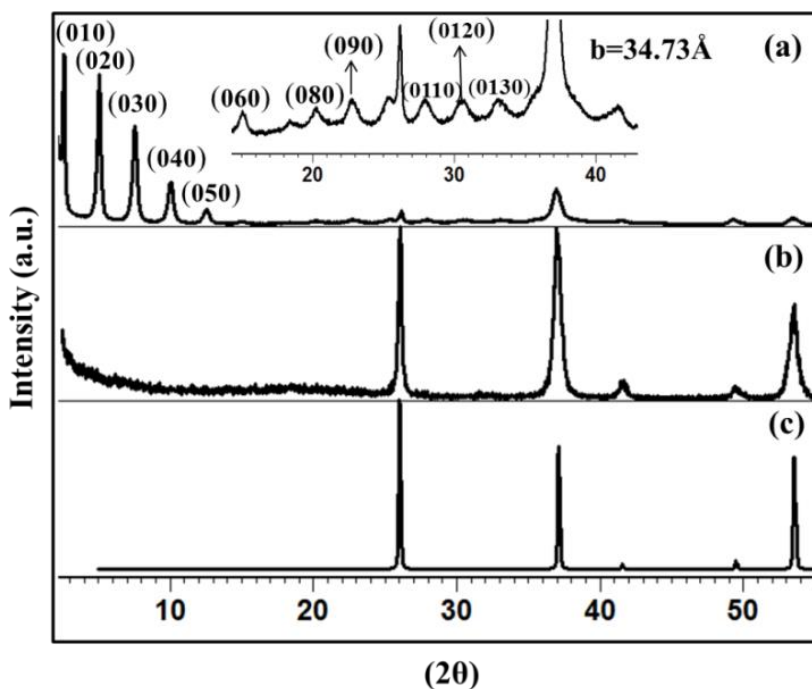
Figure 4.14. XRD patterns of samples treated at 240 °C for a) 4.5 h and b) 7 h. c) MoO_2 reference pattern.
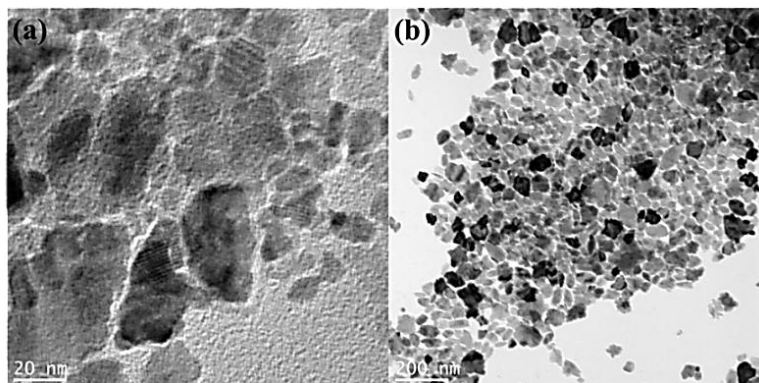
Figure 4.15. TEM images of the samples ST treated at 240°C for a) 4h and b) 7h.

Products treated at 240°C for different reaction times yield different colors. For example, while the sample obtained after 1.5 h of ST treatment shows a blue color, black products were obtained after 7 h of ST treatment and the full reduction of Mo^{6+} to Mo^{4+}. To investigate the effect of time on the optical properties of highly oriented MoO_x-OAm hybrid structure, UV-Vis/NIR absorption data with respect to reaction time were collected and shown in Figure 4.16. While sample treated for 70 minutes shows a weak absorption peak at about 952 nm, strong absorption peaks at around 910 and 926 nm were observed for the samples treated for 90 and 120 minutes, respectively (Figure 4.16).
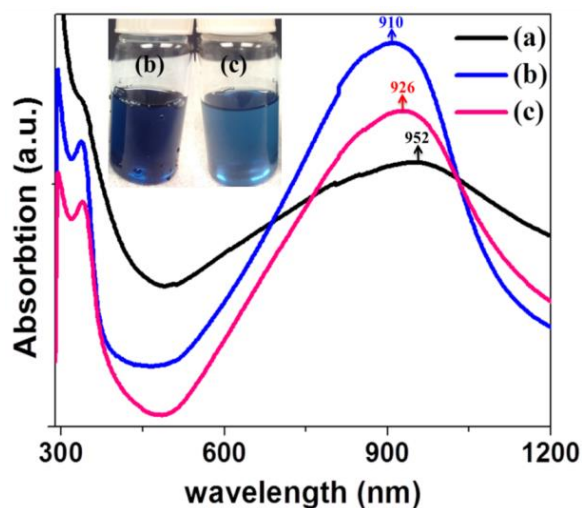
Figure 4.16. UV-Vis/NIR absorption data obtained for the samples ST treated at 240 °C for a) 70 min, b) 90 min and c) 120 min. Inset shows optical images of solutions (b) and (c). Solution *(a)* was opaque.

To further confirm the insertion/intercalation of OAm and DDA between the layers of molybdenum oxide, thermal analysis was carried out and the TGA/DSC data for both MoO_x-OAm and MoO_x-DDA hybrid structures obtained after 1.5 h and 24 h, respectively. These scans are shown in Figure 4.17.
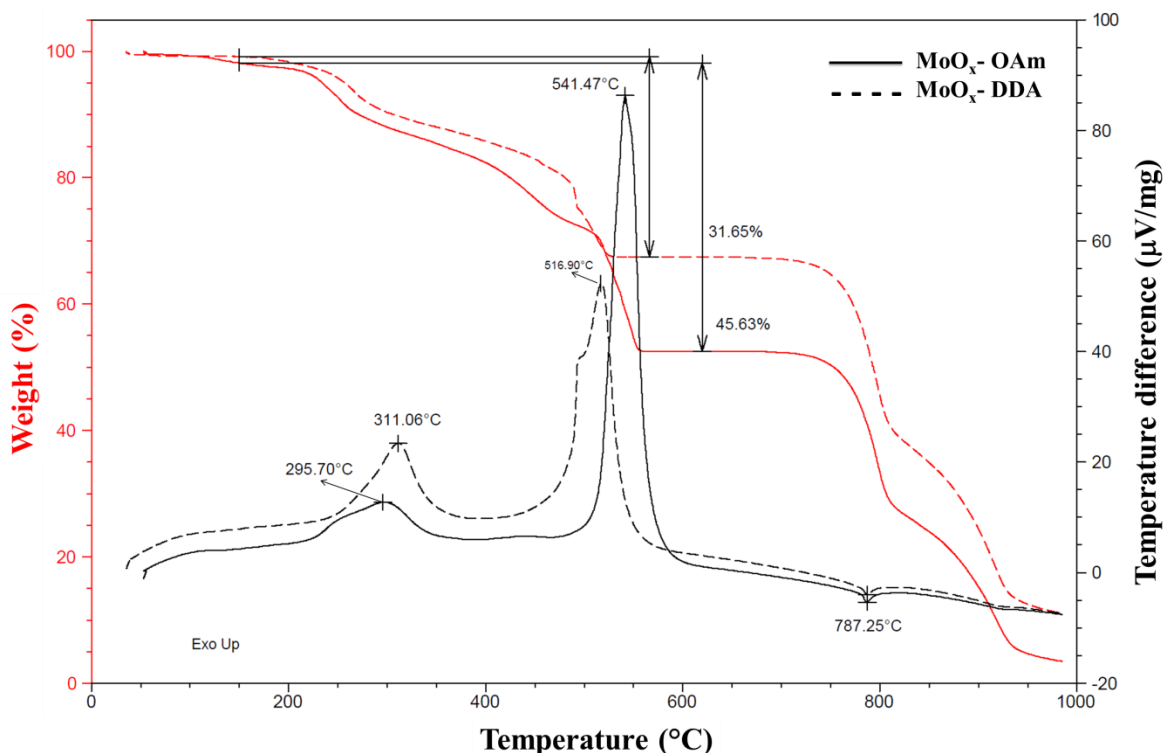
Figure 4.17. TGA (red) and DSC (black) curves showing the thermal behavior of MoO_x-DDA (dashed line) and MoO_x-OAm (solid line) obtained after 1.5 h and 24 h of ST treatment, respectively.

In addition to the weight loss before 150 °C, which could be due to the release of solvent molecules, three major thermal events were observed for both of the samples. The first two exothermic events happened at 311°C and 516°C for MoO_x–DDA, and 296°C and 541°C for MoO_x–OAm; this can be related to the decomposition/combustion of surface amines and intercalated amines, respectively. The difference in the decomposition/combustion temperatures of MoO_x-OAm and MoO_x-DDA can be attributed to different stabilities and/or reactivity of the surfactant located between the molybdenum oxide layers. 45.7% and 31.7% of weight loss were seen for MoO_x–OAm ($C_{18}H_{35}NH_2$) and MoO_x–DDA ($C_{12}H_{27}N$), respectively. The difference in weight losses for these two particular intercalated compounds is likely related to the presence of

different type and amount of hydrocarbons located between the layers. The last thermal event (at 787°C) is due to the sublimation of molybdenum oxide, which is further confirmed by similar TGA/DSC data obtained for MoO_3. XRD patterns of the MoO_x-OAm obtained after 90 minutes of ST treatment and product obtained after different temperature of TGA/DSC is shown in figure 4.18. The presence of low angle peak in the XRD pattern of the sample obtained after thermal treatment up to 400 °C confirm the remaining of the surfactant between the layers and our suggested two step loss of amine groups. Low angle peaks, however, disappear after 650°C and a phase transformation to MoO_3 structure were observed.
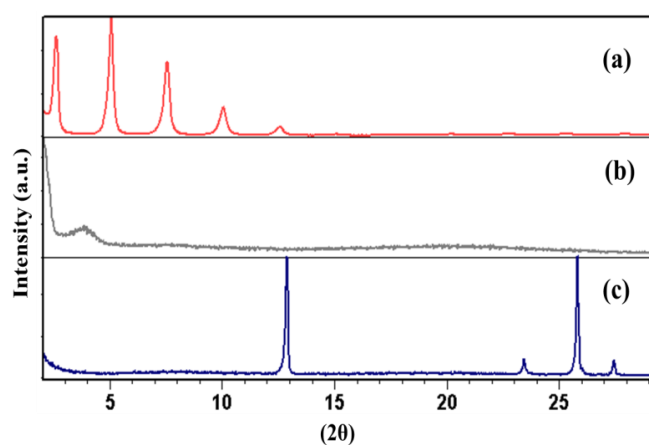
Figure 4.18. XRD patterns of a) MoO_x-OAm obtained after 90 minutes of ST treatment, b) product obtained after thermal analysis stopped at 400 °C, and c) product obtained after thermal analysis stopped at 650 °C.

4.4 Discussion

DDA ($C_{12}H_{27}N$) and OAm ($C_{18}H_{35}NH_2$) were successfully inserted between the layers of molybdenum oxide using two distinct ST–treatments. This was confirmed by the presence of low angle reflections in their XRD patterns (Figures 4.3 and 4.9) as well as the TGA data (Figure 4.17). As expected, the intercalation of DDA and OAm between the molybdenum oxide layers led to the expansion of interlayer distances, which in turn helped facilitate the exfoliation of single layer or a few layers of molybdenum oxide following sonications. The d-spacings of the intercalated molybdenum oxide layers suggest the existence of tilted bilayer organic molecules between the layers of molybdenum oxide[14,26,27] (larger than one and smaller than double chain

length of OAm/DDA). *d-* spacings were also found to be sensitive to reaction parameters such as ST duration and temperature; this could be related to variations in the amount of intercalated surfactant or different orientations of the surfactants achieved under varying reaction conditions.

In the case of molybdenum oxide–DDA hybrid structure, our investigations revealed that the conversion of MoO_3 precursor to intercalated product increases by an increase in the reaction time and that separation step is required for achieving high purity intercalated/exfoliated products. This is concluded based on the XRD data presented in Figures 4.3 and 4.5. The XRD patterns obtained before the separation process (Figure 4.3b and 4.5b-f) show co-existence of low angle peaks related to the intercalation of DDA between (*0l0*) planes of MoO_3 and high angle reflections at 2θ =12.93, 25.84, and 39.02 degrees respectively corresponding to the (020), (040), and (060) reflections of molybdenum oxide precursor. This implies that the product is not fully intercalated. However, in the XRD pattern of the sample obtained after the separation process, high angle peaks related to the (020), (040), and (060) reflections of molybdenum oxide precursor are absent (Figure 4.3c); possibly due to the presence of exclusively intercalated/exfoliated products. A potential reason for the incomplete intercalation of the obtained product even after 24 h of ST treatment could be related to the lack of consistency throughout the layered structure of MoO_3 used as the precursor. When the reaction time increased up to 72 h a gradual formation of a new intercalated MoO_x-DDA structure (Figure 4.5e and f) was perceived. This implies the effect of reaction time and kinetic on the structural rearrangement of NSs and formation of a new intercalated MoO_x-DDA structure. It should be noted that the formation of the new intercalated MoO_x structure/phase after 72 h of ST-treatment at 180°C (Figure 4.5f) was not detected when ST-treatment was conducted at lower temperature such as 160°C. In contrast, higher ST temperature as 250 °C for 10 h led to the formation of MoO_2 phase with the known monoclinic crystal structure. This specifies the effect of temperature on the formation of different MoO_x structures possibly due to its influence on the pressure of reaction vessel and reduction abilities of synthesis media favoring the most stable phase of MoO_x. This product may vary in oxidation state as well as crystal structure based on the reaction time.

MoO_x–OAm hybrid structures were also synthesized using OAm as the intercalating agent via ST treatments at different times and temperatures. When the ST-treatment was conducted at low temperature, 180°C for several days, highly-oriented hexagonal NSs with an average size of

~1µm were obtained (Figure 4.7a-c). XRD patterns for the highly–oriented hexagonal NSs showed that even after 336 h of ST treatment no other reflections except those related to the layer spacing ((*0l0*) peaks) were observed (Figure 4.9a); possibly due to the loss of symmetry in the MoO$_x$ NSs as a result of intercalation/exfoliation and/or the presence of highly defected NSs. In the two-step ST–treatment (250 °C for 80 minutes followed by another ST–treatment at 180 °C for 24 h) led to the formation of rectangular shaped NSs, ~800 nm to ~5µm in lateral size. The XRD pattern of this sample differs from the XRD pattern of the sample obtained after two weeks of ST treatment at 180 °C by the presence of several unindexable high angle peaks (Figure 4.9b). A difference in the structure and possibly in the formation mechanism of NSs obtained after two distinct ST–treatments could be considered as a potential reason for the presence of different size/shape of NSs. Advanced in-situ characterization tools may, however, provide better understanding of the formation mechanism of NSs with different sizes and shapes.

When the ST-treatment was conducted at 240°C for different time intervals, co-existence of low angle reflections related to the intercalation of OAm between the layers of MoO$_3$ and high angle peaks corresponding to the (020), (040), and (060) reflections of the MoO$_3$ precursor were detected from the XRD pattern of the sample obtained after 30 minutes (Figure 4.10b). Similar to molybdenum oxide–DDA, this indicates that the intercalation process is not yet completed and the product obtained after 30 minutes of the reaction time is not uniform. However, complete formation of intercalated product could be achieved by increasing the ST duration to 40 and 70 minutes as the high angle peaks related to the reflections of MoO$_3$ precursor vanished (Figure 4.10c, d). Highly–oriented structures with blue color and plasmonic behavior were further obtained after 90 and 120 minutes. Huang *et al.* have also reported a strong absorption peak around 900 nm for their synthesized MoO$_{3-x}$ NSs related to the localized surface plasmon resonance (LSPR).[22] Since LSPR in MoO$_{3-x}$ is originated from the charge transfer between Mo^{+6} and Mo^{+4}, the blue color could be related to the existence of oxygen vacancies and the possible presence of different MoO$_{3-x}$ phases such as Mo$_4$O$_{11}$, Mo$_8$O$_{23}$, and Mo$_9$O$_{26}$, which are expected to show NIR absorption bands.[17,22,23] The difference between absorption intensities with respect to reaction time (Figure 4.16) could be directly related to the amount of oxygen vacancies.[17,22] This would also indicate that both Mo^{+4} and Mo^{+6} are present in the synthesized plasmonic NSs and their ratios change with the reaction time and reduction of Mo^{6+} to Mo^{4+}. The reducing ability of our synthesis media at 250 °C was furthermore confirmed by the presence of MoO$_2$

observed after 4.5 h of ST-treatment (Figure 4.14a). A full reduction of Mo^{6+} to Mo^{4+} and phase transformation from highly–oriented MoO_x NSs to MoO_2 NPs was also found when the reaction time increased to 7 h (Figure 4.14b). Strain induced into the structure of MoO_x upon the reduction of Mo^{+6} to Mo^{+4} and following phase transformation from MoO_x to MoO_2 can be considered as possible reasons for the formation of NPs from NSs. However, XRD patterns (Figure 4.9a) and TEM images (Figure 4.7a-c) of the sample treated at 180°C even after 336 h show no indication for the formation of MoO_2 NPs. One may conclude that lowering the temperature may decrease the reduction ability of the synthesis media and the amount of presented defects as well as oxygen vacancies in the obtained NSs. Unlike NSs obtained at 240 °C, NSs obtained after ST-treatment at 180°C did not show blue color and strong LSPR peaks possibly due to different structure of NSs and amount of oxygen vacancies. Instability of some of the MoO_x NSs synthesized at 240 °C obtained after different ST duration could also be related to the presence of highly defective NS structures, which possess high free energies possibly due to high surface areas and structural defects. Reductions of the free energy of MoOx NSs were possibly achieved by their transformation to NSc, geometries that likely have lower surface energies as well as less structural defects.

In summary, novel synthetic approaches for the effective construction of MoO_x hybrid structures and NSs have been developed. The synthesized MoO_x-organic hybrid nanostructures and NSs are expected to show great potential for variety of applications including photothermal therapy, lithium ion batteries, catalysis, and nanodevices. Similarly, synthetic approaches introduced here could be potentially applied to the effective construction of different hybrid organic-inorganic nanostructures and NSs from other layered oxides and different organic counterparts.

4.5 References

1. Geim, A. K.; Novoselov, K. S. The Rise of Graphene. *Nat. Mater.* **2007**, *6* (3), 183–191.
2. Lin, Y.; Williams, T. V.; Xu, T.-B.; Cao, W.; Elsayed-Ali, H. E.; Connell, J. W. Aqueous Dispersions of Few-Layered and Monolayered Hexagonal Boron Nitride Nanosheets from Sonication-Assisted Hydrolysis: Critical Role of Water. *J. Phys. Chem. C* **2011**, *115* (6), 2679–2685.
3. Miyamoto, N.; Yamada, Y.; Koizumi, S.; Nakato, T. Extremely Stable Photoinduced Charge Separation in a Colloidal System Composed of Semiconducting Niobate and Clay Nanosheets. *Angew. Chem.* **2007**, *119* (22), 4201–4205.
4. Chhowalla, M.; Shin, H. S.; Eda, G.; Li, L.-J.; Loh, K. P.; Zhang, H. The Chemistry of Two-Dimensional Layered Transition Metal Dichalcogenide Nanosheets. *Nat. Chem.* **2013**, *5* (4), 263–275.

5. Nicolosi, V.; Chhowalla, M.; Kanatzidis, M. G.; Strano, M. S.; Coleman, J. N. Liquid Exfoliation of Layered Materials. *Science* **2013**, *340* (6139), 1226419.

6. Coleman, J. N.; Lotya, M.; O'Neill, A.; Bergin, S. D.; King, P. J.; Khan, U.; Young, K.; Gaucher, A.; De, S.; Smith, R. J.; Shvets, I. V.; Arora, S. K.; Stanton, G.; Kim, H.-Y.; Lee, K.; Kim, G. T.; Duesberg, G. S.; Hallam, T.; Boland, J. J.; Wang, J. J.; Donegan, J. F.; Grunlan, J. C.; Moriarty, G.; Shmeliov, A.; Nicholls, R. J.; Perkins, J. M.; Grieveson, E. M.; Theuwissen, K.; McComb, D. W.; Nellist, P. D.; Nicolosi, V. Two-Dimensional Nanosheets Produced by Liquid Exfoliation of Layered Materials. *Science* **2011**, *331* (6017), 568–571.

7. Shukoor, M. I.; Therese, H. A.; Gorgishvili, L.; Glasser, G.; Kolb, U.; Tremel, W. From Layered Molybdic Acid to Lower-Dimensional Nanostructures by Intercalation of Amines under Ambient Conditions. *Chem. Mater.* **2006**, *18* (8), 2144–2151.

8. MoO_{3-x}-Based Hybrids with Tunable Localized Surface Plasmon Resonances: Chemical Oxidation Driving Transformation from Ultrathin Nanosheets to Nanotubes - Huang - 2012 - Chemistry – A European Journal - Wiley Online Library http://onlinelibrary.wiley.com/doi/10.1002/chem.201202630/full (accessed Apr 4, 2016).

9. Hanlon, D.; Backes, C.; Higgins, T. M.; Hughes, M.; O'Neill, A.; King, P.; McEvoy, N.; Duesberg, G. S.; Mendoza Sanchez, B.; Pettersson, H.; Nicolosi, V.; Coleman, J. N. Production of Molybdenum Trioxide Nanosheets by Liquid Exfoliation and Their Application in High-Performance Supercapacitors. *Chem. Mater.* **2014**, *26* (4), 1751–1763.

10. Huang, P.-R.; He, Y.; Cao, C.; Lu, Z.-H. Impact of Lattice Distortion and Electron Doping on α-MoO3 Electronic Structure. *Sci. Rep.* **2014**, *4*, 7131.

11. Zhang, H.; Gao, L.; Gong, Y. Exfoliated MoO3 Nanosheets for High-Capacity Lithium Storage. *Electrochem. Commun.* **2015**, *52*, 67–70.

12. Kalantar-zadeh, K.; Tang, J.; Wang, M.; Wang, K. L.; Shailos, A.; Galatsis, K.; Kojima, R.; Strong, V.; Lech, A.; Wlodarski, W.; Kaner, R. B. Synthesis of Nanometre-Thick MoO_3 Sheets. *Nanoscale* **2010**, *2* (3), 429–433.

13. Afsharpour, M.; Mahjoub, A.; Amini, M. M. Synthesis of Molybdenum Oxide Nanohybrids as Efficient Catalysts in Oxidation of Alcohols. *J. Inorg. Organomet. Polym. Mater.* **2009**, *19* (3), 298–305.

14. Jing, Y.; Pan, Q.; Cheng, Z.; Dong, X.; Xiang, Y. Direct Thermal Intercalation of Amine into Layered MoO3. *Mater. Sci. Eng. B* **2007**, *138* (1), 55–59.

15. Willets, K. A.; Duyne, R. P. V. Localized Surface Plasmon Resonance Spectroscopy and Sensing. *Annu. Rev. Phys. Chem.* **2007**, *58* (1), 267–297.

16. Hutter, E.; Fendler, J. H. Exploitation of Localized Surface Plasmon Resonance. *Adv. Mater.* **2004**, *16* (19), 1685–1706.

17. Cheng, H.; Kamegawa, T.; Mori, K.; Yamashita, H. Surfactant-Free Nonaqueous Synthesis of Plasmonic Molybdenum Oxide Nanosheets with Enhanced Catalytic Activity for Hydrogen Generation from Ammonia Borane under Visible Light. *Angew. Chem. Int. Ed Engl.* **2014**, *53* (11), 2910–2914.

18. Kriegel, I.; Jiang, C.; Rodríguez-Fernández, J.; Schaller, R. D.; Talapin, D. V.; da Como, E.; Feldmann, J. Tuning the Excitonic and Plasmonic Properties of Copper Chalcogenide Nanocrystals. *J. Am. Chem. Soc.* **2012**, *134* (3), 1583–1590.

19. Zhao, Y.; Pan, H.; Lou, Y.; Qiu, X.; Zhu, J.; Burda, C. Plasmonic Cu2−xS Nanocrystals: Optical and Structural Properties of Copper-Deficient Copper(I) Sulfides. *J. Am. Chem. Soc.* **2009**, *131* (12), 4253–4261.

20. Buonsanti, R.; Llordes, A.; Aloni, S.; Helms, B. A.; Milliron, D. J. Tunable Infrared Absorption and Visible Transparency of Colloidal Aluminum-Doped Zinc Oxide Nanocrystals. *Nano Lett.* **2011**, *11* (11), 4706–4710.

21. Kanehara, M.; Koike, H.; Yoshinaga, T.; Teranishi, T. Indium Tin Oxide Nanoparticles with Compositionally Tunable Surface Plasmon Resonance Frequencies in the Near-IR Region. *J. Am. Chem. Soc.* **2009**, *131* (49), 17736–17737.

22. Huang, Q.; Hu, S.; Zhuang, J.; Wang, X. MoO$_{3-x}$ -Based Hybrids with Tunable Localized Surface Plasmon Resonances: Chemical Oxidation Driving Transformation from Ultrathin Nanosheets to Nanotubes. *Chem. - Eur. J.* **2012**, *18* (48), 15283–15287.

23. Janauer, G. G.; Dobley, A.; Guo, J.; Zavalij, P.; Whittingham, M. S. Novel Tungsten, Molybdenum, and Vanadium Oxides Containing Surfactant Ions. *Chem. Mater.* **1996**, *8* (8), 2096–2101.

24. Rostamzadeh, T.; Adireddy, S.; Zhang, X.; Koplitz, B.; Chrisey, D. B.; Wiley, J. B. Rapid Large-Scale Synthesis of Vanadate Nanoscrolls with Controllable Lengths. *ChemNanoMat* **2016**, *2* (1), 54–60.

25. Rostamzadeh, T.; Adireddy, S.; Wiley, J. B. Formation of Scrolled Silver Vanadate Nanopeapods by Both Capture and Insertion Strategies. *Chem. Mater.* **2015**.

26. Akbarian-Tefaghi, S.; Teixeira Veiga, E.; Amand, G.; Wiley, J. B. Rapid Topochemical Modification of Layered Perovskites via Microwave Reactions. *Inorg. Chem.* **2016**, *55* (4), 1604–1612.

27. Luo, H.; Wei, M.; Wei, K. A Redox-Assisted Molecular Assembly of Molybdenum Oxide Amine Composite Nanobelts. *J. Alloys Compd.* **2011**, *509* (3), 864–867.

28. Greenblatt, M. Molybdenum Oxide Bronzes with Quasi-Low-Dimensional Properties. *Chem. Rev.* **1988**, *88* (1), 31–53.

Chapter 5 Formation and Characterization of Cubic CeO₂@Hexaniobate and Cubic CeO₂-Spherical Au@Hexaniobate Nanopeapods

5.1 Introduction

Exfoliation of inorganic laminated structures has recently been the subject of notable attention due to the new properties and, therefore, various applications of these materials.[1–4] There are several methodologies used for the exfoliation of laminated structures/layered materials: liquid oxidation, ion intercalation, and ion exchange.[5,6] Several 2D crystals including graphene,[5] BN, [6]WS$_2$,[7] MoS$_2$,[8] MnO$_2$,[9] K$_4$Nb$_6$O$_{17}$,[10] and Ruddlesden–Popper[11] and Dion–Jacobson[12] type perovskites can be obtained using different exfoliation techniques.

Scrolling of exfoliated/lamellar nanosheets (NSs) into tubular morphologies has also been investigated and shown possible for a variety of inorganic materials such as V$_2$O$_5$,[13] graphite,[14] layered chalcogenides[15] and K$_4$Nb$_6$O$_{17}$.[16,17] Acid-exchanged hexaniobate (H$_x$K$_{4-x}$Nb$_6$O$_{17}$) is one of the structures that can be exfoliated and, through a simple ST synthesis method, has the capability to transform into NScs geometry in order to relieve structural strain.[16–18] The layered hexaniobate is biocompatible, chemically stable, and is a wide-band gap semiconductor material. It has been shown that the hexaniobate nanosheets show photocatalytic activity under UV-light.[19,20]

Manipulation and incorporation of nanoparticles into the hollow space of nanoscrolls is an important step in the evolution of advanced materials towards nanodevices. These nanostructures can be considered as "peapods" that consist of a chain of desired nanoparticles ("peas") encapsulated/inserted/grown within desired NScs ("pods").[21–24] The ability to encapsulate different kinds of nanoparticles having diverse light harvesting properties inside the hexaniobate nanoscrolls may lead to the formation of new nanoarchitectures that yield new properties and, therefore, are capable of different applications such as those in surface-enhanced Raman scattering (SERS)[25], optical waveguides, photonics, or nanodevices for biological and chemical sensing.[26,27] There exist several characteristics for NPPs such as size, shape and type of encapsulated/inserted NPs, type and morphological features of NScs, structural uniformity,

lengths and interlayer distances of NTs/NScs, filling fraction of encapsulated/inserted NPs, NPs distance that can be controlled to obtain varieties of nanocomposites with tunable properties (Figure 1.12). Bi-functional NPPs in which different types of NPs arranged within hollow space of NSs could also be designed (Figure 1.12).

Although a number of synthetic approaches for the fabrication of NPPs have already been reported by different groups,[22,26,28–38] NPPs fabrication methods require more development in terms of simplicity, flexibility, and efficiency in such a way that different categories of NPPs with controlled compositions and morphological features can be manufactured. A simple and versatile synthesis method for the solvothermal encapsulation of spherical Fe_3O_4 NPs inside hexaniobate NScs and encapsulation/insertion of spherical Ag NPs inside vanadate NScs have already been developed and reported by our group.[21,39] However, formation of faceted NPs in the interior sites of NScs to the best of our knowledge have not been reported. Herein, we first report the encapsulation of cubic shape CeO_2 NPs within hexaniobate NScs using a modified solvothermal approach. Then, the formation of CeO_2-Au@hexaniobate NPPs using an in-situ growth of Au NPs within partially field CeO_2@hexaniobate NPPs used as a template is presented.

5.2 Experimental

Materials. Oleic acid (99.8%, OAc), oleylamine (>70%, OAm), sodium oleate (>97%), cerium (III) nitrate hexahydrate (99.99%), tributylamine (99%), tetrabutylammonium hydroxide 30-hydrate (TBAOH) (97%), gold(III) chloride trihydrate (99.99%), silver nitrate (99.99%), L-ascorbic acid and toluene (99.8%, anhydrous) were all obtained from Sigma-Aldrich. K_2CO_3 (99%) and Nb_2O_5 (99%) were purchased from Alfa Aesar.

Synthesis of $K_4Nb_6O_{17}$ crystallites. $K_4Nb_6O_{17}$ was synthesized through a solid-state reaction of K_2CO_3 and Nb_2O_5 (in the molar ratio of 1.0:1.4) in air at 900 °C for 1h before continuing to heat at 1050 ºC for another 24 h. A slight excess of K_2CO_3 was used to compensate for the loss of volatile potassium oxide species. The product was washed 2 times with distilled water and acetone and finally dried overnight at 80 °C.

Synthesis of $H_xK_{4-x}Nb_6O_{17}$. In order to make $H_xK_{4-x}Nb_6O_{17}$, similar experimental conditions as previously reported by Saupe *et al.* were used.[18] 0.15 g of $K_4Nb_6O_{17}$ powder were mixed with

15 mL of a 3 M HCl solution and stirred at 50 °C for 3 days. The obtained proton-exchange form of hexaniobate was thoroughly washed with the mixture of *ca.* of milli-Q water and acetone and then dried at 80 °C.

Solvothermal synthesis of intercalated multi-walled nanoscrolls (INS). As reported before by Adireddy et al.[17] $H_xK_{4-x}Nb_6O_{17}$ (0.05 g), 0.15 g (0.19 mmol) TBAOH, 5 mL oleylamine (~15 mmol), and 8 mL of toluene were mixed in a 20 mL vial and magnetically stirred for an hour. Final solution was transferred into a Teflon-lined stainless steel autoclave (Parr, model 4749, 1800 psig, 23 mL) and kept at 220 °C for 6 h. The resulting product was washed several times with ethanol and centrifuged for 5 minutes to remove soluble components.

Solvothermal synthesis of cubic CeO$_2$ NPs. Cubic ceria NPs with different sizes were prepared by a modified synthesis approach reported by Saruyama *et al.*[40] In order to make 5 nm cubes, 1mmol of cerium (III) nitrate hexahydrate were dissolved in 5.5 mL of water. After 10 minutes of magnetic stirring, 5.5 mL toluene, 2.5 mL oleic acid, 2.5 mL oleylamine, and 0.15 mL of tributylamine (TBA) were added to the aqueous solution and stirred for about 30 minutes. The solution was transferred into a 23 mL Teflon-lined stainless-steel Parr autoclave. Solvothermal treatment was done at 200°C for 40 h and then cooled down to room temperature. The obtained precipitate was washed with a mixture of ethanol (40 mL) and toluene (5 mL) and then centrifuged for 5 minutes to remove soluble components. For imaging, nanoparticles without any size selection were easily dispersed in toluene, sonicated for one minute and drop caste on a TEM grid.

Similar experimental routes, with some changes in the amount of surfactants, cerium precursor, and solvothermal temperature/time were applied to synthesize ~25nm, ~35 nm, and the mixture of small and big cubes ranging from 5 to 40 nm (Table 5.1). While most reactions were carried out in 23 mL autoclave, one reaction was carried out in a 100mL Teflon-lined stainless steel autoclave; this reaction was carried out for 12 h at 190 °C and then 220 °C for 2.5h.

Table 5.1 Experimental conditions for synthesizing different sized CeO_2 nanocubes.

Cubic NPs	CNH (mmol)	DI water (mL)	Toluene (mL)	OAm (mL)	OAc (mL)	SO (gr)	TBA (mL)	Temp. (°C)	Time (h)
~5 nm	1	5.5	5.5	2.5	2.5	0.0	0.15	200	18
~25 nm	1	29	29	0.0	10	1	0.4	170	48
~35 nm	0.5	7.5	7.5	0.0	0.75	0.065	0.075	180	40
~5-40 nm	4	30	30	0.0	10	0.52	0.6	190, 220	12, 2.5

Solvothermal synthesis of CeO₂@hexaniobate NPPs. 30 mg of CeO_2 NPs dispersed in 8 mL toluene were added to a mixture of 60 mg $H_xK_{4-x}Nb_6O_{17}$, 5 mL OAm, and 0.15 g TBAOH. The reaction solution was magnetically stirred for an hour and transferred to a 23 mL Teflon-lined stainless steel autoclave (Parr, model 4749, 1800 psig). The sealed autoclave was heated to 220 °C for 6 h. The resulting precipitate was washed with toluene and separated via centrifugation. The obtained product was redispersed in hexane and further centrifugation was applied to remove/reduce free ceria NPs.

Synthesis of CeO₂-Au@hexaniobate NPPs. In the first step, partially filled CeO₂@hexaniobate NPPs were synthesized using the same synthetic approach as for CeO₂@hexaniobate NPPs except the amount of preformed ceria NPs was reduced by two-thirds (from 30 to 10 mg). Then, 15 mg of these partially filled NPPs were mixed with HAuCl₄·3H₂O ( ), toluene (3 mL), OAc (160 µL, 0.5 mmol) and OAm (165 µL, 0.5 mmol), and magnetically stirred. The solution was heated to 55 °C and held at this temperature for 2 h. The obtained product was separated using centrifugation and dispersed in toluene.

Characterization. The morphologies of the products were characterized with a TEM JEOL 2010 operated at an accelerating voltage of 200 kV and equipped with a Gatan slow scan CCD camera. The unit also has an EDAX genesis energy dispersive spectroscopy (EDS) system. SEM was carried out using a Carl Zeiss 1530 VP field-emission scanning electron microscope (FESEM). For transmission electron microscopy (TEM) measurements, toluene dispersed samples were drop-caste onto a 200 mesh carbon-coated copper grid and heated in a drying oven at 60 °C overnight. High-angle annular dark-field scanning TEM (HAADF-STEM) and EDS

mapping measurements were carried out using FEI TECNAI G2 F30 FEG TEM (300 kV). Absorption spectra were recorded (in reflectance mode) via a Cary 500 UV-Vis spectrophotometer.

5.3 Results

Different sized cubic-CeO$_2$ NPs ranging from 5 to 40 nm were successively synthesized via a modified ST approach using cerium nitrate as the cerium precursor and oleylamine and oleic acid as the capping agents. TEM images of cubic-ceria NPs with different sizes (5 nm, 25 nm, 35 nm, and a mixture of 5 - 40 nm) presented in Figure 5.1. X-ray diffraction patterns of solvothermally synthesized 5 nm and 35 nm ceria nanocubes along with a reference pattern shown in Figure 5.2 confirm the formation of single phase CeO$_2$ NPs. XRD peak broadening, which is an indication for the formation of smaller size NPs,[41] was observed in the case of 5 nm nanocubes.
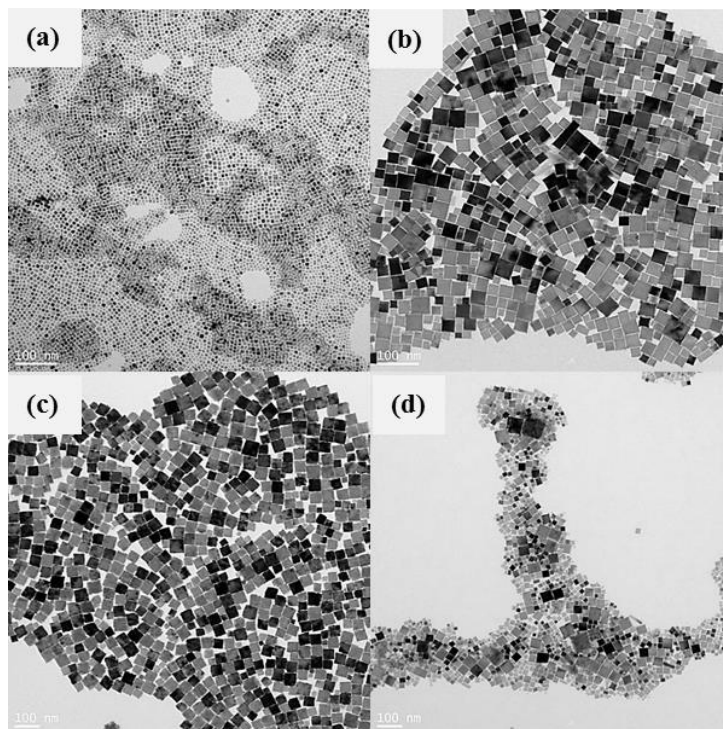
Figure 5.1. TEM images showing different sizes cubic CeO$_2$ NPs (a) 5 nm, (b) 25 nm (c) 35 nm, and (d) mixture of 5 to 40nm.
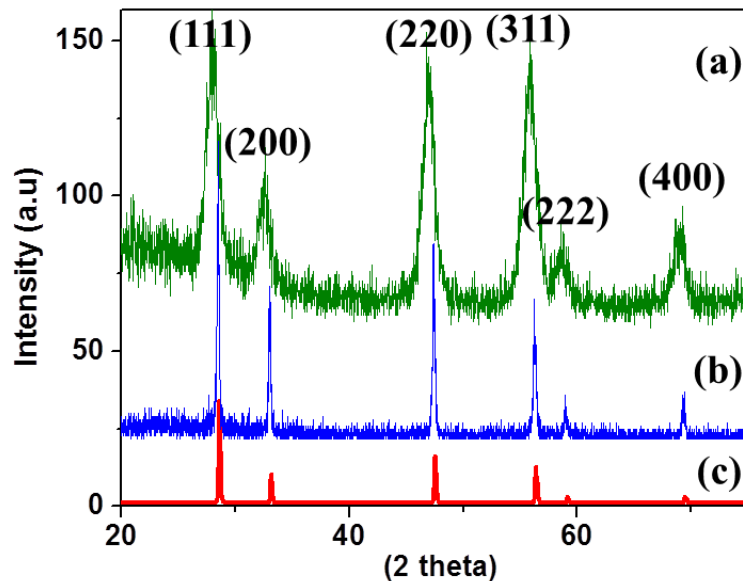
Figure 5.2. XRD patterns of (a) 5nm (b) 35nm ceria NPs versus (c) CeO_2 reference pattern.

TEM images of synthesized 5nm cubic ceria NPs, is furthermore displayed in higher magnification (Figure 5.3a). As can be seen from Figure 3a, 5nm ceria NPs are mainly cubic and could be self-assembled upon a simple drop casting of the colloidal solution on a TEM grid.

Solvothermal treatment of preformed 5 nm ceria NPs in the presence of acid-exchanged hexaniobate ($H_xK_{4-x}Nb_6O_{17}$), OAm, and TBAOH led to the formation of high quality NPPs (Figure 5.3b-d, and Figure 5.4). EDS data collected during TEM measurements also revealed the existence of Ce, and Nb as the main noticeable elements of the peas (ceria) and pods (hexaniobate), respectively. As can be seen from TEM images (Figure 5.3b-d) long chains of cubic ceria NPs with different inter-particle distances (1-3nm) are organized and encapsulated inside the hexaniobate NScs. In some cases, up to 80 NPs are linearly captured and arranged in a single scroll. In some occasions, more than a row of NPs are located in a single scroll as can be realized from the presented SEM image of NPPs (Figure 5.4). Furthermore, different lengths of hexaniobate NScs ranging from approximately 50 nm to 800 nm consisting of up to 5 layers were detected through the TEM observations. Outer diameters were also estimated to be between 20-70 nm. Inner diameter of CeO_2@hexaniobate NPPs appears to have a narrower size distribution than hexaniobate NScs, similar to what has been observed in our previous studies.[21,39] Size selective encapsulation of ceria NPs where similar size NPs located in distinct NScs can further be recognized from the highlighted area shown in Figure 5.3d. Interestingly, no NPs were observed to be encapsulated when ≥ 25 nm nanocubes were solvothermally treated using the same synthetic approach. However, when a mixture of small and big cubes ranging from 5 to 40 nm (Figure 5.1d) were used to make NPPs, smaller

95

than 10 nm particles were encapsulated efficiently, while bigger than 10 nm cubes mainly located outside of the scrolls (Figure 5.5)

Scanning electron microscopy image display the preorganization of cubic NPs on the surface of high energy sites/edges of NSs and scrolling process (Figure 5.6). Size selective attachment of NPs to different parts of hexaniobate NSs could also be noticed from presented SEM image in Figure 5.6b.
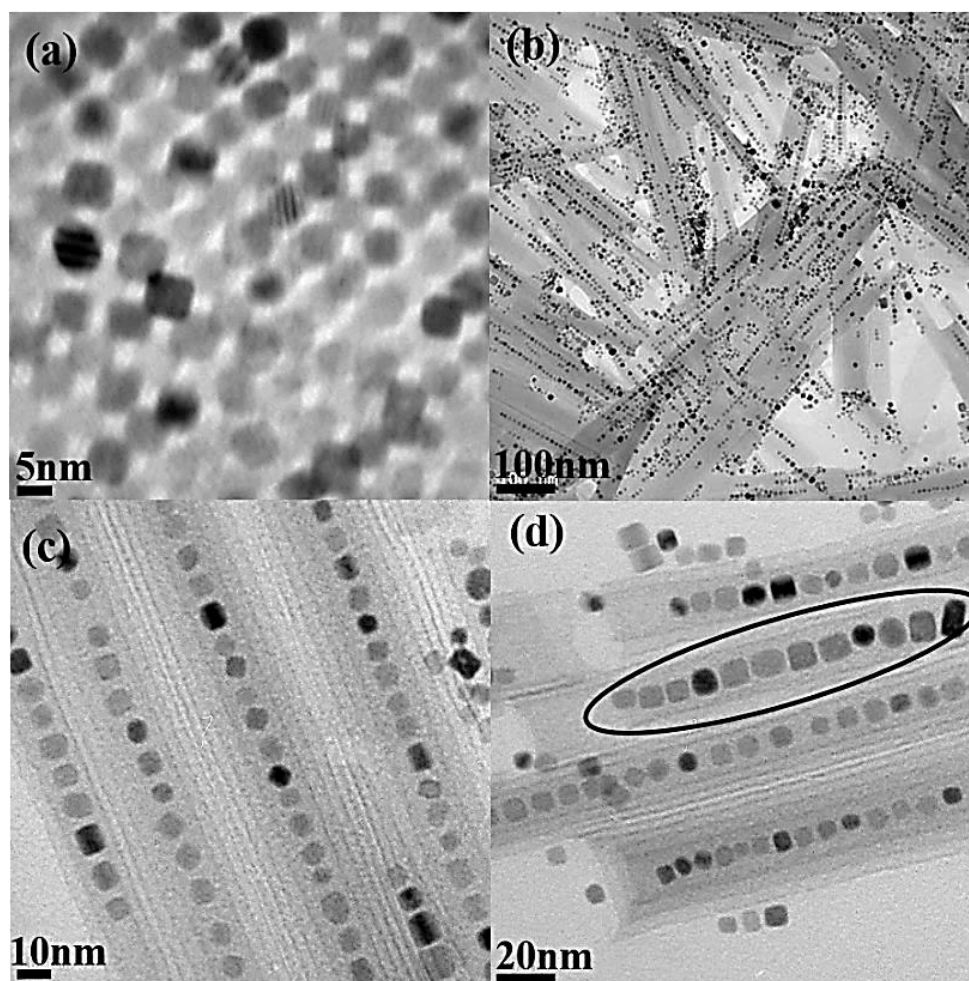
Figure 5.3. TEM image of (a) 5 nm self-assembled CeO_2 NPs obtained upon simple drop casting, (b) low magnification TEM image of CeO_2@hexaniobate NPPs, and (c, d) higher magnification TEM images of the NPPs. Circled area in (d) indicates size selective encapsulation.
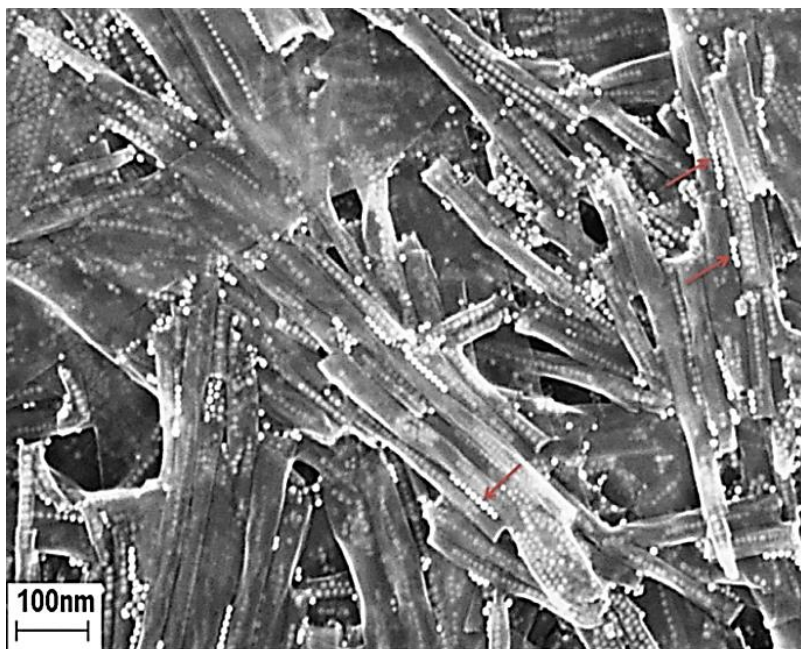
Figure 5.4. SEM image of formed CeO$_2$@hexaniobate NPPs. Some of the NPs chains with a very bright contrast appear to align along the edge of scrolls as indicated by red arrows
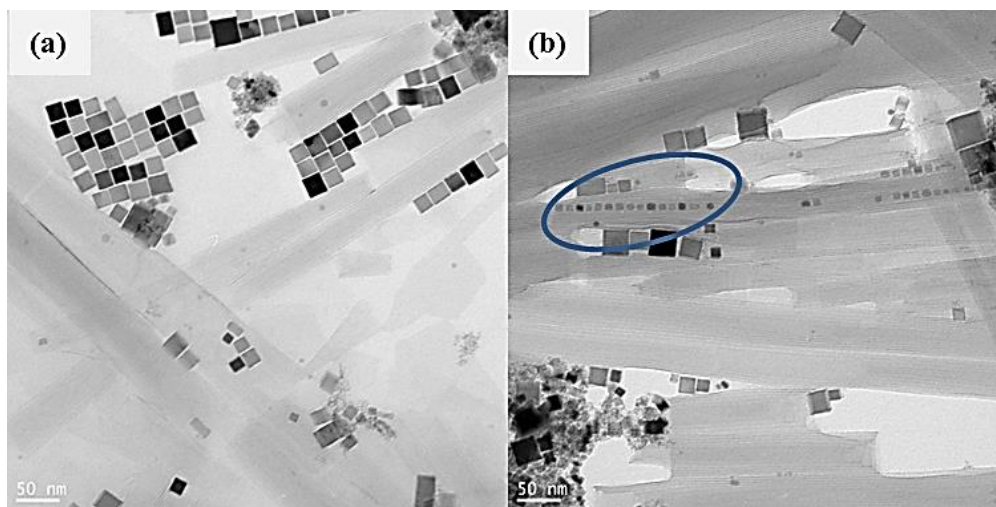
Figure 5.5. TEM images of showing the synthesized sample obtained when mixture of small and big cubes (5-40nm) were used to make peapods. While smaller than 10 nm particles can be efficiently captured (marked area) bigger than 10 nm cubes are mainly outside of the scrolls.
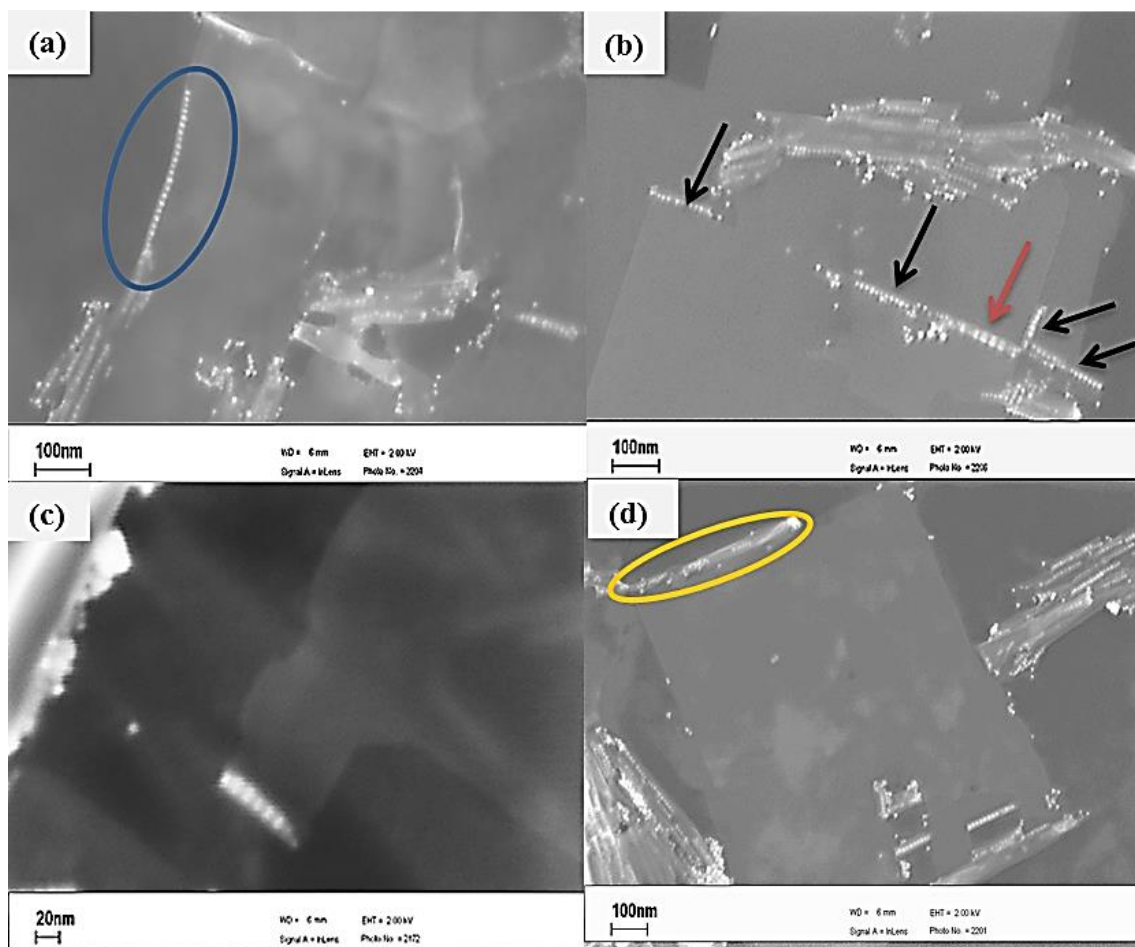
Figure 5.6. Different magnification SEM images show the nanosheets during the preorganization of NPs and scrolling process. Red arrow in (b) shows the size selective attachments of ~8 nm cubes while black ones show size selective encapsulations of ~5 nm cubes.

The scrolling process of hexaniobate NSs likely happened after the size selective attachment of NPs to the edge of NSs (Figure 5.6). It should be mentioned that using similar experimental conditions, but in the absence of cubic ceria NPs, individual Nb_6O_{17} layers can be exfoliated upon the intercalation of TBAOH and, then convolve into tubular morphology to relieve mechanical strain correlated to intrinsic asymmetric layers.[16–18] The final step is detachment of NScs through the nucleation and growth of cracks on the surface of NSs/nanocrystals (Figure 5.7c). SEM images of protonated hexaniobate before the ST treatment, during the detachment process and after the complete formation of NSs are shown in Figure 5.7.
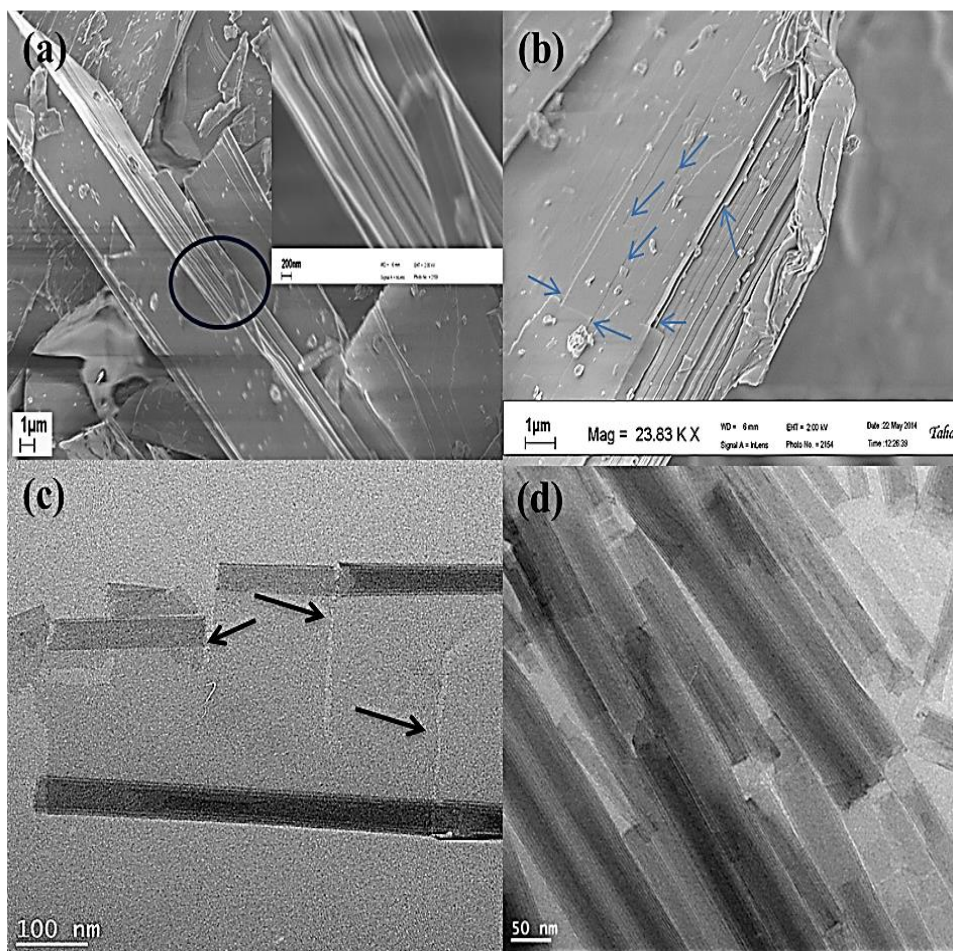
Figure 5.7. (a and b) SEM images of acid-exchanged hexaniobate ($H_xK_{4-x}Nb_6O_{17}$) arrows in (b) indicates the potential sites for scrolling and NPs attachments in the formation of NScs and NPPs respectively, (c) TEM image showing the formation of cracks on the surface of NSs leading to the detachment of formed NScs from NSs. (d) TEM image show completely formed hexaniabate NScs.

CeO$_2$-Au@hexaniobate NPPs were synthesized using partially filled CeO$_2$@hexaniobate NPPs as templates. As seen in the schematic (Figure 5.8), partially filled NPPs is dispersed in a solution containing Au^{3+}, OAm, OAc, and toluene where OAm acts as both surfactant and reducing agent. The final product obtained after 2 h of treatment at 55 °C is composed of free gold NPs as well as CeO$_2$-Au@hexaniobate NPPs. Multiple centrifugation step are needed to separate NPPs from NPs. It should be mentioned that the same synthesis approach in the absence of partially filled NPPs led to the formation of Au NPs and that Au@hexaniobate NPPs could be synthesized using empty hexaniobate NScs as the template.
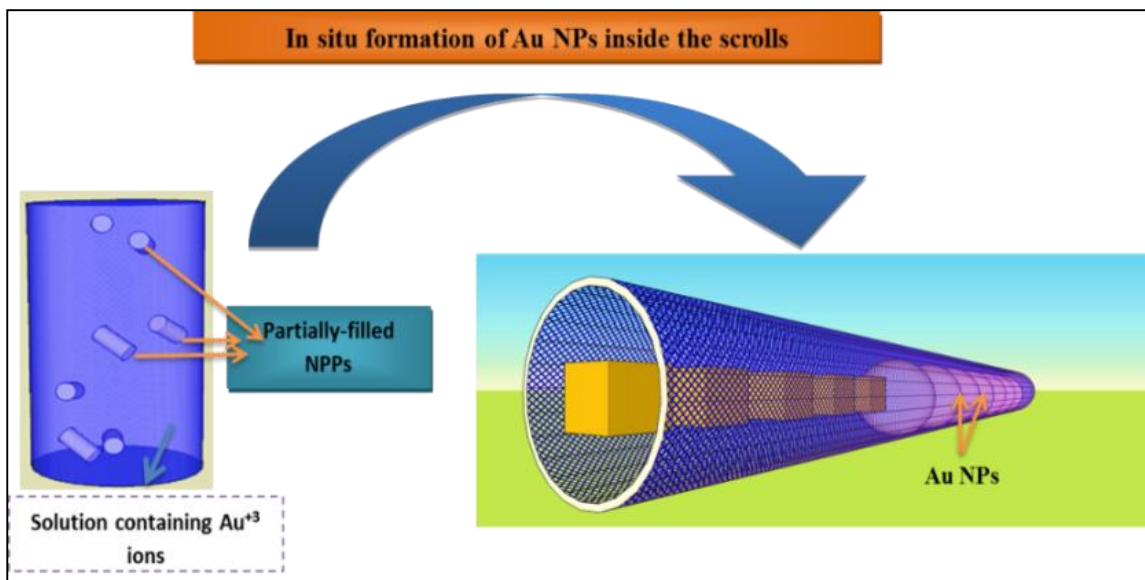
Figure 5.8. Schematic showing the in-situ growth of gold NPs within partially filled CeO_2@hexaniobate NPPs.

TEM images of the obtained product after the separation step are shown in Figure 5.9. High- yield formation of CeO_2-Au@hexaniobate NPPs can be realized from low magnification TEM images. Gold NPs with higher atomic numbers appear to be darker and are mainly spherical, while cubic ceria are brighter except those aligned in the direction of zone axis. Therefore, some of those NPs which are cubic and seem to be brighter, are marked by black arrows indicating likelihood the presence of ceria NPs. Different arrangement of ceria and gold NPs were detected during TEM observation. We have also observed the formation of gold nanorods inside some of the hexaniobate NScs (Figure 5.9d). Formation of Au nanorod was already observed in the case of Au-Fe_3O_4 @hexaniobate NPPs when prolonging the reaction time.[35] Interestingly, no gold nanorods detected outside of the nanoscrolls in both cases. One may conclude the role of hexaniobate NScs acts as a template for the oriented attachment of Au NPs within NScs leading to the formation of nanorods. It is expected that by decreasing the amount of surfactants and prolonging the reaction time the oriented attachment and therefore possibility of gold nanorods formation could be further encouraged.
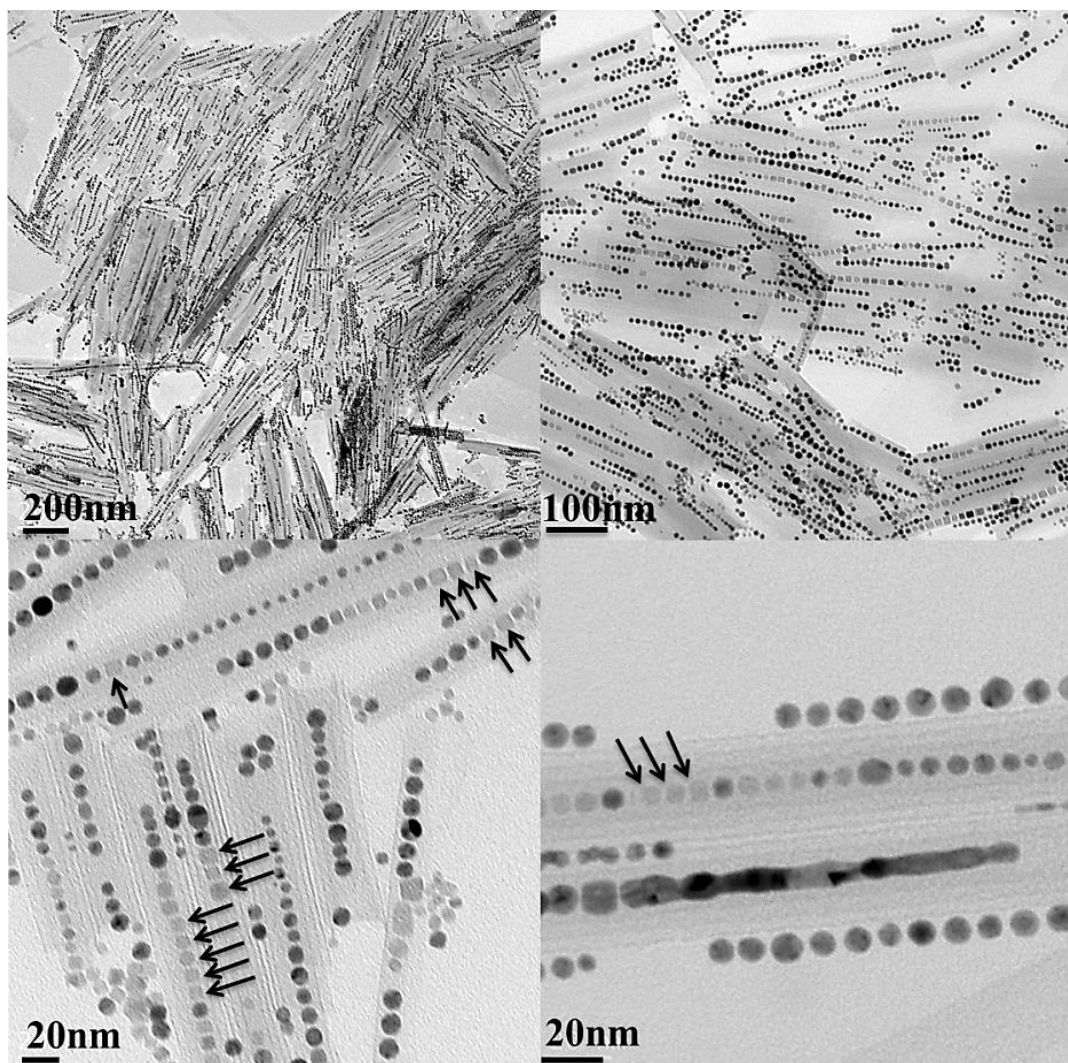
Figure 5.9. a, and b) low magnification (c, and d) higher magnification TEM images of CeO$_2$-Au@hexaniobate NPPs. black arrows in c, and d indicate the existence of cubic ceria NPs.

In order to further confirm the coexistence of Au NPs with ceria NPs inside hexaniobate NScs, the final structures were characterized with high-angle annular dark-field scanning TEM (HAADF-STEM), and EDS elemental mapping. Figure 5.10a shows HAADF-STEM image of CeO$_2$-Au@hexaniobate NPPs which is highlighted in Figure 5.10b. Au NPs appear to be brighter, while CeO$_2$ NPs seem darker. Supplementary EDS elemental mapping analyses of NPPs provide direct evidence for the presence of Au and CeO$_2$ NPs inside the hexaniobate NScs (Figure 5.11c-e). More even distribution of niobium all over the NPPs structure is due to the presence of niobium as one of the main elements of hexaniobate nanosheets (Figure 5.10e).
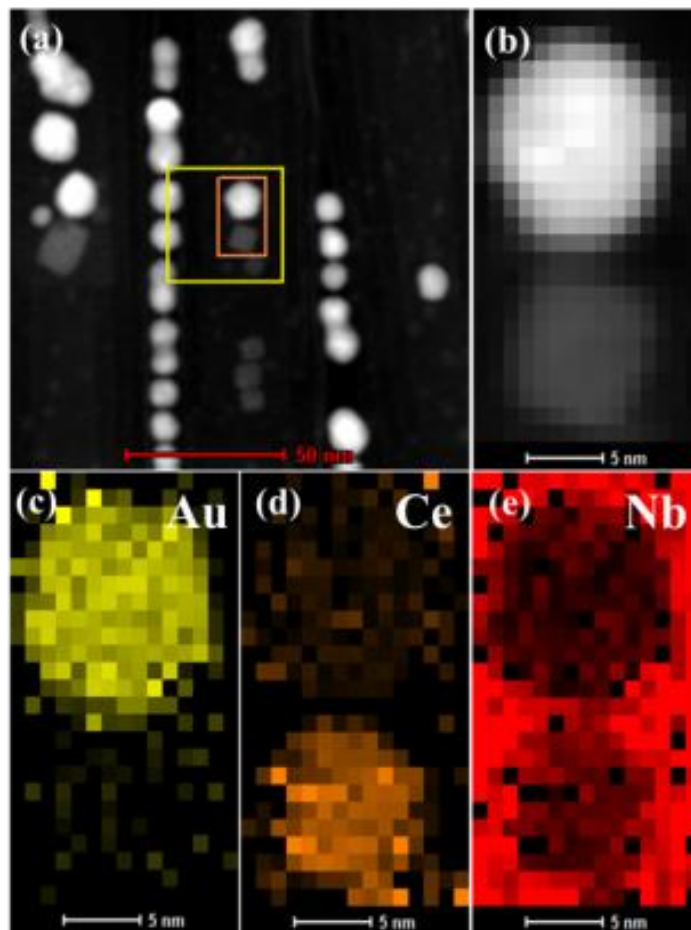
Figure 5.10. (a, and b) HAADF-STEM image of CeO$_2$-Au@hexaniobate NPPs. c–e) EDS elemental mapping analysis of NPPs for c) Au, d) Ce, and e) Nb.

It has been shown that in a chain of NPs, surface plasmon (SPR) peak depends on the coupling between adjacent NPs.[42–45] Moreover, the surface plasmon resonance (SPR) peak of the noble metals NPs are shape, size, and environment dependent.[44–46] In order to examine the optical properties of NPPs, UV−vis absorption spectra of Au@hexaniobate NPPs, and CeO$_2$-Au@hexaniobate NPPs dispersed in toluene collected and shown in Figure 11. The absorption peaks appear at 530 and 543nm for Au@hexaniobate NPPs and CeO$_2$-Au@hexaniobate NPPs, respectively (Figure 5.11). These results are in a good agreement with our previous studies presented on the optical properties of Au@hexaniobate NPPs and bi-functional Fe$_3$O$_4$-Au@hexaniobate NPPs.[35]
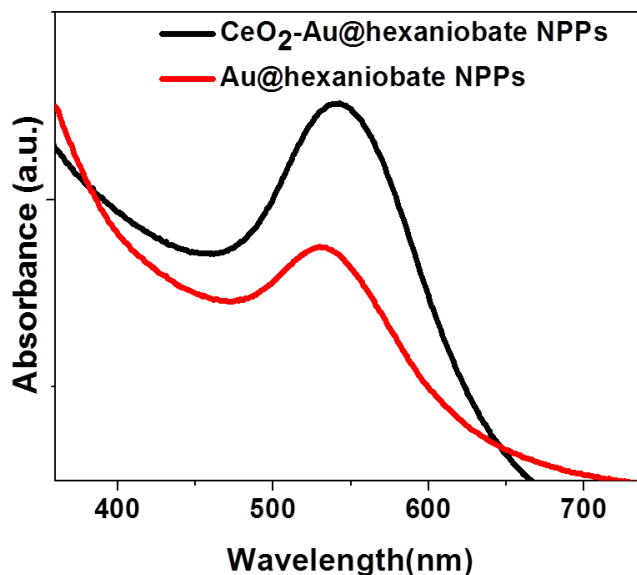
Figure 5.11 UV/Vis absorption spectra for Au@hexaniobate NPPs (red) and CeO$_2$-Au@hexaniobate NPPs (black). The SPR peaks appear at 530 and 543nm for Au@hexaniobate NPPs and CeO$_2$-Au@hexaniobate NPPs, respectively.

5.4 Discussion

Filling different types of NTs using different classes of NPs with distinct shapes and morphological features is very attractive for the improvement of advanced nanocomposites. Innovative properties arising from these constructs can mainly depend on the intrinsic behavior of the NPs ("peas") and the NTs/NSs ("pods") as well as interactions between various NPs and interactions between NPs and NScs.

Solvothermal approaches have previously been used for the formation of spherical magnetite NPPs.39 Similar methods were applied for the formation of cubic-CeO$_2$ nanocomposites using solvothermally synthesized cubic-ceria NPs. High yield encapsulations of cubic ~5 nm ceria NPs within hexaniobate NScs via a 6 h solvothermal approach using protonated hexaniobate crystals were achieved (Figure 5.3b-c). Size selective encapsulations where similar sizes of NPs are located in a distinct NSc were also observed (Figure 5.3d). In terms of the formation mechanism

of cubic CeO$_2$@hexaniobate NPPs, our characterizations support the preorganization and attachment of the cubic ceria NPs to the surface of hexaniobate crystals prior to the scrolling process. This supports the previous suggested mechanism.39 During the solvothermal treatment of hexaniobate crystals/sheets in the presence of high concentration of CeO$_2$ NPs, due to high pressure and, therefore, high rate of particles-crystals collisions, NPs were first attached and self-organized on high energy sites of the hexaniobate crystals. Preorganization of NPs and scrolling was mainly observed on the edge of the crystals (Figure 5.6). Preorganization of smaller and similarly sized NPs on the surface of NSs were recognized from SEM image presented in Figure 5.6b. Attachment of NPs to the surface/edge of hexaniobate NSs may help facilitate the scrolling process by increasing the total strain energy of NSs. Similar detachment process as perceived for hexaniobate NScs (Figure 5.7c), were also observed in the case of CeO$_2$@hexaniobate NPPs. After the detachment of NPPs from the hexaniobate crystals, the edge or other high energy sites of newly created surface/edges (due to the detachment) can be considered as potential sites for further attachments of NPs. The attachment of NPs, scrolling of NSs, formation of cracks, and finally detachment of NPPs continue throughout the solvothermal process leading to the formation of NPPs in high-yield (Figure 5.3b-d). Other types of cubic NPs can also be encapsulated; initial investigations on cubic Mn$_3$O$_4$ showed that modified solvothermal treatment could be used for the formation of Mn$_3$O$_4$@hexaniobate NPPs.

The ability to use partially field NPPs as a template and grow different types of NPs directly inside the empty space of the template can lead to the development of advanced classes of nanocomposites with tunable properties. We further investigate the in-situ growth of spherical gold NPs inside partially field cubic-CeO$_2$@hexaniobate NPPs. High-yield formation of CeO$_2$-Au@hexaniobate nanocomposites (Figure 5.9), where two distinct types of NPs with different shapes, cubic and spherical, are arranged in the hexaniobate NScs, was achieved (Figure 5.9, and 5.10). A similar synthetic approach for the production of bi-functional Fe$_3$O$_4$-Au@hexaniobate NPPs has recently been developed by our group.[35] This further emphasizes the versatility of our synthetic approach in the production of different types of bi-functional NPPs. We have previously shown that surface plasmon resonance peak for Au@hexaniobate (530 nm) NPPs is red shifted in comparison to free Au NPs (524 nm) due to NP coupling effects, which leads to energy shifts and energy confinement between NPs.[35] Remarkably, a greater shift in SPR peak is realized for Au-CeO$_2$@hexaniobate NPPs. The SPR peak observed for CeO$_2$-Au@hexaniobate

NPPs is 14 nm bigger than for Au@hexaniobate, which could be related to different NPs interactions.

In summary, a combination of our developed synthetic approaches (solvothermal, in-situ growth, and insertion) for the formation of NPPs can be used to obtain diverse classes of NPPs composed of different types, shapes, and arrangements of encapsulated/directly grown/inserted NPs as "peas" and distinct morphological features of NTs/NScs as "pods". Encapsulations of more than two different types/shapes of preformed NPs/nanorods (NRs) via a modified solvothermal approach within hexaniobate NScs are also being attempted. Moreover, development of bi-functional NPPs using an adjusted synthetic protocol for the in-situ growth of other noble metal NPs/NRs (Ag, Pd, and Pt) within different types of partially field "pods" such as hexaniobate, vanadate, and halloysite NScs are currently under investigation. Insertion strategy where NPs could be drawn into the hollow space of NScs/NTs upon the solvent evaporation has previously been reported for the formation of Ag@vanadate NScs, and could further be applied for the formation of bi-functional NPPs. This emerging class of nanoarchitectures with distinct morphological features and unique arrangements of different functional NPs could provide a system for the fundamental studies of NP-NP as well as NP-NSc interactions, especially using in-situ characterization tools. Moreover, depending on different combinations of NPs and NScs, this unique class of nanocomposite materials could find several applications including SPR-based nanosensors, rechargeable battery components, photocatalysis, and photonic and electronic devices.

5.5 References

1. Feng, H.; Hu, Z.; Liu, X. Facile and Efficient Exfoliation of Inorganic Layered Materials Using Liquid Alkali Metal Alloys. *Chem Commun* **2015**, *51* (54), 10961–10964.
2. Gupta, A.; Sakthivel, T.; Seal, S. Recent Development in 2D Materials beyond Graphene. *Prog. Mater. Sci.* **2015**, *73*, 44–126.
3. Niu, L.; Coleman, J. N.; Zhang, H.; Shin, H.; Chhowalla, M.; Zheng, Z. Production of Two-Dimensional Nanomaterials via Liquid-Based Direct Exfoliation. *Small* **2016**, *12* (3), 272–293.
4. Liu, B.; Köpf, M.; Abbas, A. N.; Wang, X.; Guo, Q.; Jia, Y.; Xia, F.; Weihrich, R.; Bachhuber, F.; Pielnhofer, F.; Wang, H.; Dhall, R.; Cronin, S. B.; Ge, M.; Fang, X.; Nilges, T.; Zhou, C. Black Arsenic–Phosphorus: Layered Anisotropic Infrared Semiconductors with Highly Tunable Compositions and Properties. *Adv. Mater.* **2015**, *27* (30), 4423–4429.
5. Hernandez, Y.; Nicolosi, V.; Lotya, M.; Blighe, F. M.; Sun, Z.; De, S.; McGovern, I. T.; Holland, B.; Byrne, M.; Gun'Ko, Y. K.; Boland, J. J.; Niraj, P.; Duesberg, G.; Krishnamurthy, S.; Goodhue, R.;

Hutchison, J.; Scardaci, V.; Ferrari, A. C.; Coleman, J. N. High-Yield Production of Graphene by Liquid-Phase Exfoliation of Graphite. *Nat. Nanotechnol.* **2008**, *3* (9), 563–568.

6. Lin, Y.; Williams, T. V.; Connell, J. W. Soluble, Exfoliated Hexagonal Boron Nitride Nanosheets. *J. Phys. Chem. Lett.* **2010**, *1* (1), 277–283.

7. Voiry, D.; Yamaguchi, H.; Li, J.; Silva, R.; Alves, D. C. B.; Fujita, T.; Chen, M.; Asefa, T.; Shenoy, V. B.; Eda, G.; Chhowalla, M. Enhanced Catalytic Activity in Strained Chemically Exfoliated WS2 Nanosheets for Hydrogen Evolution. *Nat. Mater.* **2013**, *12* (9), 850–855.

8. Lukowski, M. A.; Daniel, A. S.; Meng, F.; Forticaux, A.; Li, L.; Jin, S. Enhanced Hydrogen Evolution Catalysis from Chemically Exfoliated Metallic MoS2 Nanosheets. *J. Am. Chem. Soc.* **2013**, *135* (28), 10274–10277.

9. Liu, Z.; Xu, K.; Sun, H.; Yin, S. One-Step Synthesis of Single-Layer MnO_2 Nanosheets with Multi-Role Sodium Dodecyl Sulfate for High-Performance Pseudocapacitors. *Small* **2015**, *11* (18), 2182–2191.

10. Miyamoto, N.; Yamamoto, H.; Kaito, R.; Kuroda, K. Formation of Extraordinarily Large Nanosheets from K4Nb6O17 Crystals. *Chem. Commun.* **2002**, No. 20, 2378–2379.

11. Schaak, R. E.; Mallouk, T. E. Prying Apart Ruddlesden−Popper Phases: Exfoliation into Sheets and Nanotubes for Assembly of Perovskite Thin Films. *Chem. Mater.* **2000**, *12* (11), 3427–3434.

12. Maeda, K.; Mallouk, T. E. Comparison of Two- and Three-Layer Restacked Dion–Jacobson Phase Niobate Nanosheets as Catalysts for Photochemical Hydrogen Evolution. *J. Mater. Chem.* **2009**, *19* (27), 4813–4818.

13. Rostamzadeh, T.; Adireddy, S.; Zhang, X.; Koplitz, B.; Chrisey, D. B.; Wiley, J. B. Rapid Large-Scale Synthesis of Vanadate Nanoscrolls with Controllable Lengths. *ChemNanoMat* **2016**, *2* (1), 54–60.

14. Xu, Z.; Zheng, B.; Chen, J.; Gao, C. Highly Efficient Synthesis of Neat Graphene Nanoscrolls from Graphene Oxide by Well-Controlled Lyophilization. *Chem. Mater.* **2014**, *26* (23), 6811–6818.

15. Li, Y. D.; Li, X. L.; He, R. R.; Zhu, J.; Deng, Z. X. Artificial Lamellar Mesostructures to WS2 Nanotubes. *J. Am. Chem. Soc.* **2002**, *124* (7), 1411–1416.

16. Maeda, K.; Eguchi, M.; Lee, S.-H. A.; Youngblood, W. J.; Hata, H.; Mallouk, T. E. Photocatalytic Hydrogen Evolution from Hexaniobate Nanoscrolls and Calcium Niobate Nanosheets Sensitized by Ruthenium(II) Bipyridyl Complexes. *J. Phys. Chem. C* **2009**, *113* (18), 7962–7969.

17. Adireddy, S.; Yao, Y.; He, J.; Wiley, J. B. Rapid Solvothermal Fabrication of Hexaniobate Nanoscrolls. *Mater. Res. Bull.* **2013**, *48* (9), 3236–3241.

18. Saupe, G. B.; Waraksa, C. C.; Kim, H.-N.; Han, Y. J.; Kaschak, D. M.; Skinner, D. M.; Mallouk, T. E. Nanoscale Tubules Formed by Exfoliation of Potassium Hexaniobate. *Chem. Mater.* **2000**, *12* (6), 1556–1562.

19. Sarahan, M. C.; Carroll, E. C.; Allen, M.; Larsen, D. S.; Browning, N. D.; Osterloh, F. E. K4Nb6O17-Derived Photocatalysts for Hydrogen Evolution from Water: Nanoscrolls versus Nanosheets. *J. Solid State Chem.* **2008**, *181* (7), 1678–1683.

20. Kudo, A.; Sayama, K.; Tanaka, A.; Asakura, K.; Domen, K.; Maruya, K.; Onishi, T. Nickel-Loaded K4Nb6O17 Photocatalyst in the Decomposition of H_2O into H_2 and O_2: Structure and Reaction Mechanism. *J. Catal.* **1989**, *120* (2), 337–352.

21. Rostamzadeh, T.; Adireddy, S.; Wiley, J. B. Formation of Scrolled Silver Vanadate Nanopeapods by Both Capture and Insertion Strategies. *Chem. Mater.* **2015**.

22. Cong, V. T.; Ganbold, E.-O.; Saha, J. K.; Jang, J.; Min, J.; Choo, J.; Kim, S.; Song, N. W.; Son, S. J.; Lee, S. B.; Joo, S.-W. Gold Nanoparticle Silica Nanopeapods. *J. Am. Chem. Soc.* **2014**, *136* (10), 3833–3841.

23. Yao, Y.; Chaubey, G. S.; Wiley, J. B. Fabrication of Nanopeapods: Scrolling of Niobate Nanosheets for Magnetic Nanoparticle Chain Encapsulation. *J. Am. Chem. Soc.* **2012**, *134* (5), 2450–2452.

24. Adireddy, S.; Rostamzadeh, T.; Carbo, C. E.; Wiley, J. B. Particle Placement and Sheet Topological Control in the Fabrication of Ag–Hexaniobate Nanocomposites. *Langmuir* **2015**, *31* (1), 480–485.

25. Willets, K. A.; Duyne, R. P. V. Localized Surface Plasmon Resonance Spectroscopy and Sensing. *Annu. Rev. Phys. Chem.* **2007**, *58* (1), 267–297.

26. Liu, L.; Lee, W.; Scholz, R.; Pippel, E.; Gösele, U. Tailor-Made Inorganic Nanopeapods: Structural Design of Linear Noble Metal Nanoparticle Chains. *Angew. Chem. Int. Ed.* **2008**, *47* (37), 7004–7008.

27. Haes, A. J.; Zou, S.; Schatz, G. C.; Van Duyne, R. P. A Nanoscale Optical Biosensor: The Long Range Distance Dependence of the Localized Surface Plasmon Resonance of Noble Metal Nanoparticles. *J. Phys. Chem. B* **2004**, *108* (1), 109–116.

28. Smith, B. W.; Monthioux, M.; Luzzi, D. E. Encapsulated C60 in Carbon Nanotubes. *Nature* **1998**, *396*, 323–324.

29. Luzzi, D. E.; Smith, B. W. Nanoscopic Hybrid Materials: The Synthesis, Structure and Properties of Peapods, Cats and Kin. In *Science and Application of Nanotubes*; Thorpe, M. F., Tománek, D., Enbody, R. J., Eds.; Fundamental Materials Research; Springer US, 2002; pp 67–76.

30. Ajayan, P. M.; Stephan, O.; Redlich, P.; Colliex, C. Carbon Nanotubes as Removable Templates for Metal Oxide Nanocomposites and Nanostructures. *Nature* **1995**, *375* (6532), 564–567.

31. Chen, P.-H.; Hsieh, C.-H.; Chen, S.-Y.; Wu, C.-H.; Wu, Y.-J.; Chou, L.-J.; Chen, L.-J. Direct Observation of Au/Ga2O3 Peapodded Nanowires and Their Plasmonic Behaviors. *Nano Lett.* **2010**, *10* (9), 3267–3271.

32. Zhou, W. W.; Sun, L.; Yu, T.; Zhang, J. X.; Gong, H.; Fan, H. J. The Morphology of Au@MgO Nanopeapods. *Nanotechnology* **2009**, *20* (45), 455603.

33. Hunyadi, S. E.; Murphy, C. J. Tunable One-Dimensional Silver−Silica Nanopeapod Architectures. *J. Phys. Chem. B* **2006**, *110* (14), 7226–7231.

34. Yang, Y.; Li, L.; Li, W. Plasmon Absorption of Au-in-CoAl2O4 Linear Nanopeapod Chains. *J. Phys. Chem. C* **2013**, *117* (27), 14142–14148.

35. Adireddy, S.; Carbo, C. E.; Rostamzadeh, T.; Vargas, J. M.; Spinu, L.; Wiley, J. B. Peapod-Type Nanocomposites through the In Situ Growth of Gold Nanoparticles within Preformed Hexaniobate Nanoscrolls. *Angew. Chem. Int. Ed.* **2014**, *53* (18), 4614–4617.

36. Kharisov, B. I.; Kharissova, O. V.; Ortiz-Méndez, U. *Handbook of Less-Common Nanostructures*; CRC Press: Boca Raton, Floride, 2012.

37. Hsieh, C.-H.; Chou, L.-J.; Lin, G.-R.; Bando, Y.; Golberg, D. Nanophotonic Switch: Gold-in-Ga2O3 Peapod Nanowires. *Nano Lett.* **2008**, *8* (10), 3081–3085.

38. Ajayan, P. M.; Lijima, S. Capillarity-Induced Filling of Carbon Nanotubes. *Nature* **1993**, *361* (6410), 333–334.

39. Adireddy, S.; Carbo, C. E.; Yao, Y.; Vargas, J. M.; Spinu, L.; Wiley, J. B. High-Yield Solvothermal Synthesis of Magnetic Peapod Nanocomposites via the Capture of Preformed Nanoparticles in Scrolled Nanosheets. *Chem. Mater.* **2013**, *25* (19), 3902–3909.

40. Yang, S.; Gao, L. Controlled Synthesis and Self-Assembly of CeO$_2$ Nanocubes. *J. Am. Chem. Soc.* **2006**, *128* (29), 9330–9331.

41. Zhang, F.; Chan, S.-W.; Spanier, J. E.; Apak, E.; Jin, Q.; Robinson, R. D.; Herman, I. P. Cerium Oxide Nanoparticles: Size-Selective Formation and Structure Analysis. *Appl. Phys. Lett.* **2002**, *80* (1), 127–129.

42. Zhao, L.; Kelly, K. L.; Schatz, G. C. The Extinction Spectra of Silver Nanoparticle Arrays: Influence of Array Structure on Plasmon Resonance Wavelength and Width. *J. Phys. Chem. B* **2003**, *107* (30), 7343–7350.

43. Lamprecht, B.; Schider, G.; Lechner, R. T.; Ditlbacher, H.; Krenn, J. R.; Leitner, A.; Aussenegg, F. R. Metal Nanoparticle Gratings: Influence of Dipolar Particle Interaction on the Plasmon Resonance. *Phys. Rev. Lett.* **2000**, *84* (20), 4721–4724.

44. Su, K.-H.; Wei, Q.-H.; Zhang, X.; Mock, J. J.; Smith, D. R.; Schultz, S. Interparticle Coupling Effects on Plasmon Resonances of Nanogold Particles. *Nano Lett.* **2003**, *3* (8), 1087–1090.

45. Wei, Q.-H.; Su, K.-H.; Durant, S.; Zhang, X. Plasmon Resonance of Finite One-Dimensional Au Nanoparticle Chains. *Nano Lett.* **2004**, *4* (6), 1067–1071.

46. Chen, T.; Pourmand, M.; Feizpour, A.; Cushman, B.; Reinhard, B. M. Tailoring Plasmon Coupling in Self-Assembled One-Dimensional Au Nanoparticle Chains through Simultaneous Control of Size and Gap Separation. *J. Phys. Chem. Lett.* **2013**, *4* (13), 2147–2152.

Appendix A Synthesis and characterization of Ag@hexaniobate NPPs

A.1 Experimental

Synthesis of Ag@hexaniobate NPPs using an in-situ growth of Ag NPs.

Ag@hexaniobate NPPs were synthesized using preformed NScs as templates. In a typical experiment, preformed multi-walled hexaniobate NScs (30 mg), $AgNO_3$ (20 mg), ethanol (3 mL), OAm (3 mL) were mixed inside a vial and sonicated for one minute. The obtained mixture was heated to 75 °C and magnetically stirred for 10 minutes. 5 mg of L-ascorbic acid was then added to the stirring mixture and the final solution was kept stirring at the same temperature (75 °C) for a day. The obtained dark-brown Ag@hexaniobate NPPs were purified and separated using multiple centrifugation steps.

A.2 Results

The in-situ formations of Ag NPs within preformed hexaniobate NScs used as a template were also accomplished. Similar to our previous report on the formation of Au@hexaniobate NPPs, the obtained products consist of both free NPs and NPPs which could be separated using multiple centrifugation steps. TEM images of obtained Ag@hexaniobate NPPs obtained after separation process are presented in Figure A1.

Although majority of hexaniobate NScs (>80%) are filled with Ag NPs (Figure Aa-d), directly grown Ag NPs are seen to have a broad size distribution; unlike what has perceived in the Au@hexaniobate NPPs in which narrow size distribution of Au NPs were observed. Size of Ag NPs were estimated to vary between 5-30nm. Ag NPs with different sizes can clearly be seen from Figure A1d. Experimental conditions are being modified for the formation of uniform/different size of Ag NPs grown directly inside the hexaniobate NScs.
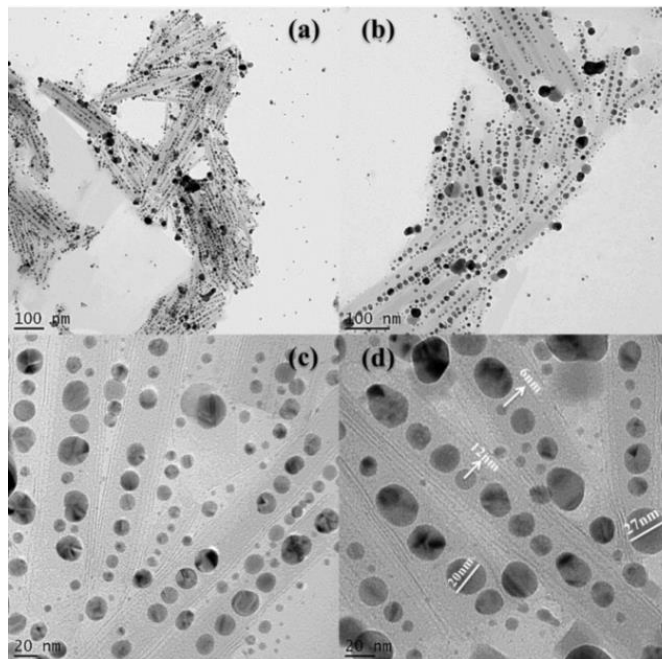
Figure A1. (a, and b) low magnification (c, and d) higher magnification TEM images of Ag@hexaniobate NPPs.

A.3   Discussion

Besides the solvothermal treatment, in-situ growth of NPs directly inside the hollow space of NScs is another synthetic route for the high-yield formation of NPPs. This process was recently developed by our group for the synthesis of Au@hexaniobate. Using a modified approach, Ag NPs could directly be grown inside intercalated multi-wall NScs (INS) in a low temperature as 75°C using a reductive synthesis media (Figure A1). After the reduction of silver ions to silver atoms, when the concentration of silver atoms reaches to a minimum concentration needed for nucleation, nucleation occurs. Nucleation and growth of Ag NPs can happen either directly inside the solution or empty space of NScs which can be considered as heterogeneous nucleation sites. Our TEM images showed that silver NPs do not have a narrow size distribution (Figure A1); unlike gold NPs in Au@hexaniobate NPPs. It should be noted that in the synthesis of Au@hexaniobate NPPs only OAm was used as a reducing agent. However, both L-ascorbic acid and OAm were used as the reducing agent for the reduction of Ag ions and formation of Ag

atoms, followed by nucleation and growth processes. This might cause a secondary nucleation process which can lead to the formation of different sizes of Ag NPs. The methods for the formation of uniform size Ag NPs and Ag@hexaniobate NPPs using a single reducing agent are being sought. Formation of bi-functional CeO_2-Ag@hexaniobate NPPs using the in-situ growth of Ag NPs within partially field CeO_2 @hexaniobate NPPs is also under investigation.

# Appendix B Rapid Synthesis of Au@halloysite NPPs

B.1   Experimental

Synthesis of Au@halloysite NPPs using an in-situ growth of Ag NPs.

Au@halloysite NPPs were synthesized using commercially available halloysite NScs as templates. In a typical experiment, halloysite NScs (15 mg), gold(III) chloride trihydrate (22 mg), ethanol (2 mL), toluene (2 mL) OAm (0.5 mL), and OAc (0.5 mL) were mixed inside a vial and sonicated for two minutes. The obtained mixture was magnetically stirred and heated to 55°C. 10mg of L-ascorbic acid was then added to the stirring mixture. One minutes after the addition of L-ascorbic acid, the stirring mixture was transferred to a dark purple color indicating the formation of gold NPs. the final solution was kept stirring at the same temperature for additional 5 minutes. The obtained product was purified and separated using multiple centrifugation steps. For the in-situ formation of Au nanorods similar experimental conditions as previously explained was adopted except for the amount of L-ascorbic acid (150 mg).

B.2   Results
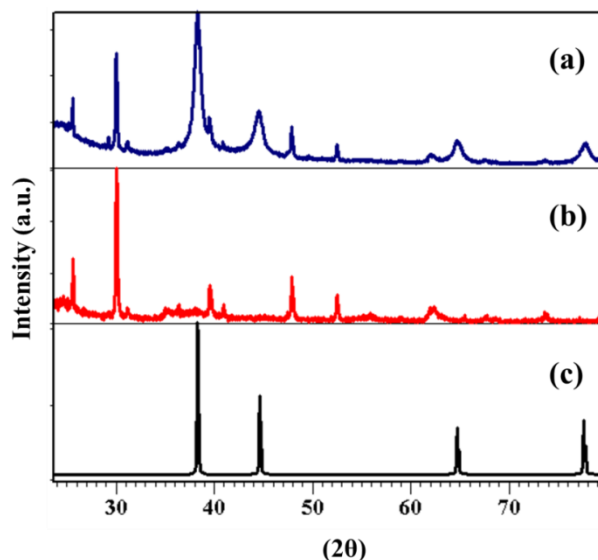
Figure B1. XRD Patterns of a) Au @ halloysite b) Pristine halloysite, and c) Au reference pattern
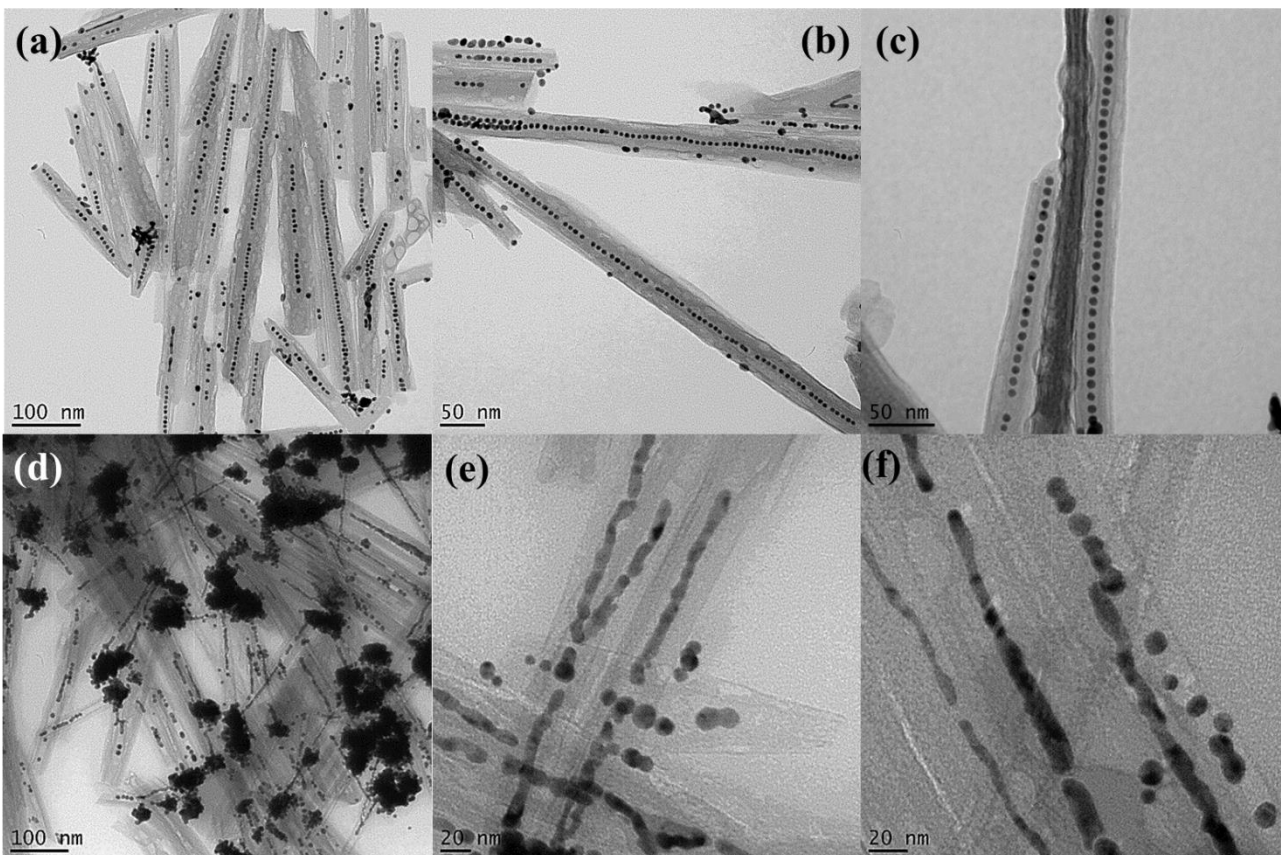
Figure B2. Different magnification TEM images of (a-c) Au NPs @halloysite, and (d-f) Au nanorods @halloysite.

Vita

Taha Rostamzadeh was born in Garmsar, Semnan, Iran. In 2001, he was accepted into the Bachelor of Science program at Semnan University, Iran, with material science and engineering/metallurgy as his major. He graduated in 2005 and continued his studying in the field of nanotechnology/nanomaterials at Tarbiat Modares University (TMU). He obtained his master's degree in 2008. In August 2011, he was admitted into the graduate program in Advanced Materials Research Institute (AMRI), Department of Chemistry at the University of New Orleans, New Orleans, LA, USA. He obtained another master's degree in Materials Chemistry in 2013 and then continued his Ph.D. degree studies in Nanomaterials Chemistry in Professor John B. Wiley's research group.